RIVISTA DEL NUOVO CIMENTO VOL. 9, N. 1 1986

Processing the Signals from Solid-State Detectors in Elementary-Particle Physics.

E. GATTI

Dipartimento di Elettronica del Politecnico - Milano, Italia

P. F. MANFREDI

Dipartimento di Fisica dell'Università - Milano, Italia
Istituto Nazionale di Fisica Nucleare - Sezione di Milano, Italia

(ricevuto il 5 Giugno 1985)

---

1. – Review of the solid-state devices employed in elementary-particle physics.

More than fifteen years ago a silicon active target made of five detectors was employed on a CERN beam to investigate coherent interactions of π-mesons on the Si nucleus [1]. That was probably the first time that a solid-state device was used as an active target in the beam of a large accelerator. Some years afterwards the same technique was adopted in another coherent-production experiment carried out at higher energies at the accelerator of Serpukhov [2].

In both experiments the active target consisted of a telescope of surface barrier, totally depleted silicon detectors, aligned along the beam axis at small mutual distances.

The configuration of an active target used in the coherent-production experiment is shown in fig. 1.1. The target used in the Serpukhov experiment consisted of ten 200 μm thick detectors with an active area of 3.5 cm^2 each.

A device of the type shown in fig. 1.1 has a high space resolution in the beam direction. It allows the measurement of the longitudinal ionization density as a function of the position and, therefore, the pattern of the charged multiplicity

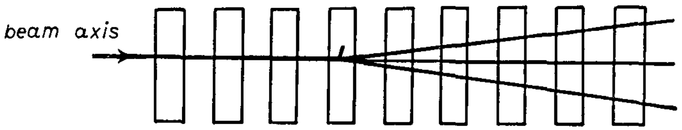

Fig. 1.1. – Silicon active target to investigate coherent processes on the Si nucleus.

can be reconstructed. The detectors where a large energy release occurs as a consequence of a nucleus recoil or of a nucleus break-up can be identified. An example of event reconstructed from the ionization density along the target is shown in fig. 1.2.

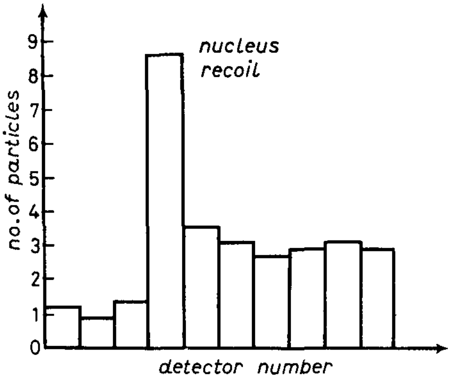

Fig. 1.2. – Coherent event reconstructed from a target of the type shown in fig. 1.1.

Signal processing associated with an active target aims at measuring the energy released along the telescope. This requires an accurate measurement of the charge made available by each detector.

A target similar to that of fig. 1.1 was employed in the first FRAMM experiment to measure the lifetime of short-lived particles [3-5].

The target employed in the FRAMM I experiment was actually designed to measure lifetimes of charmed particles in the $(10^{-13}\div 10^{-12})$ s range.

It consisted of forty silicon detectors 300 μm thick and with 1.5 cm^2 active surface. As any telescope intended for lifetime measurements it had, as compared to the configurations adopted for coherent production, the additional constraint of a very thin air gap between the detectors, 200 μm or less. This requirement comes from the need of keeping the probability of decays occurring in the air gaps as small as possible. A FRAMM event is shown in fig. 1.3. The energies measured in the various detectors are displayed detector after detector.

The unit adopted for the energy scale is the most probable value of the Landau distribution of one minimum-ionizing particle crossing the given detector thickness, $\sim$ 81 keV in the actual case. So, the diagram of fig. 1.3 can be considered presented in units of charged multiplicity. The event corresponding to the multiplicity pattern of fig. 1.3 is shown in the same figure. A high-energy photon beam was employed. The first detectors, that the photon crosses without interacting, do not produce output signals and what appears in the charged-multiplicity axis is the energy equivalent of the electronic noise.

The production detector is identified by a large energy release due to the nucleus recoil. Two minimum-ionizing particles are produced and a multiplicity $\nu = 2$ is measured in some detectors following the one where production

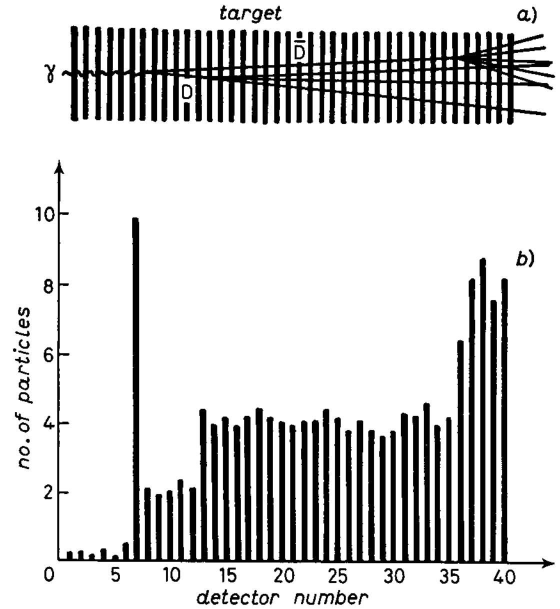

Fig. 1.3. - FRAMM event, production and decay (*a*)), ionization pattern along the telescope (*b*)).

took place. If, as expected, the two produced particles decay within the telescope, the decays give rise to multiplicity variations that are recorded by the silicon detectors.

The described technique of lifetime measurement was substantially improved for the FRAMM II data taking. The first target suffered from accuracy limitations in the energy measurement due to some extent to the electronics and to a larger extent to the fact that the technology employed in detector manufacturing was not adequate for the purpose. In order to meet the requirement of a close spacing between them, a substantial increase in the detector capacitance had to be accepted.

A remarkable improvement in the performances was achieved by using detectors manufactured according to the planar process introduced by KEMMER and shown schematically in fig. 1.4 [6, 7]. The detector shown in fig. 1.4 is based upon ion implantation of the junction and of the rear ohmic contact and SiO_2 passivation.

As a next step, for shorter-lifetime measurements the device of fig. 1.5 was developed [8-10].

The device of fig. 1.5 is obtained from a body of high-purity *n*-type germanium, on the upper face of which *p*-type strips are implanted. A 300 μm layer on the lower face, obtained by diffusing and drifting lithium, and the Al metallization realize the ohmic contact. When reverse bias is applied between the strips and the lower Al plane, the body is depleted of free charge and each strip defines a detector with the section of germanium body underneath.

The device as a whole can be thought of as a sequence of equal detectors with no physical separation in between.

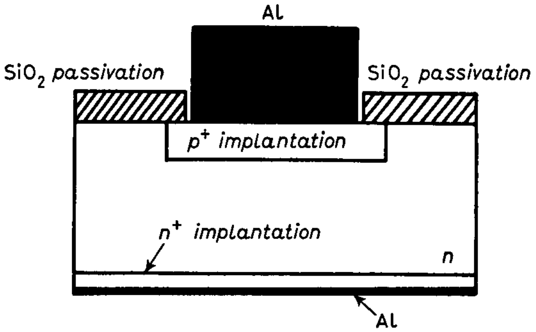

Fig. 1.4. – Silicon detector realized with the planar process.

The beam incidence is parallel to the strip plane. Therefore, the transversal dimensions must be large enough to cover the beam section. In the actual case, the detector thickness is 5 mm and its width 2 cm. The longitudinal dimension is limited to a fraction of radiation length, to avoid excessive beam contamination from e^+, e^- pairs.

The germanium bulk detector, like the silicon telescope, implements the twofold function of active target and of detector of the resulting physical event. In the sketch of fig. 1.5, a photon enters the bulk detector, a photoproduction occurs with nucleus recoil and creation of minimum-ionizing particles. The ionization density produced in the detector is sensed, as a function of the position along the axis, by the strips.

The germanium bulk detector of fig. 1.5 has the advantage over the silicon telescope of fig. 1.1 of a higher spatial resolution along the beam, $(50 \div 100)$ μm *vs.* 200 μm. Such a gain in granularity results from the factor-two-higher specific energy loss in germanium than in silicon, from the absence of air gaps

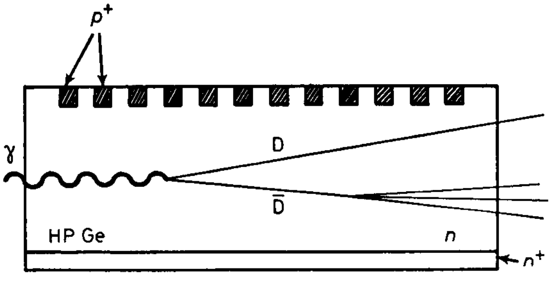

Fig. 1.5. – Ge bulk detector.

between the detection cells and from a more favourable charge transfer to the readout electronics resulting from the lower capacitance of the pick-up electrodes.

The actual FRAMM target combines the properties of the Ge bulk detector and of the Si telescope, as shown in fig. 1.6*a*) [11]. Figure 1.6*b*) shows an event detected in the composite target.

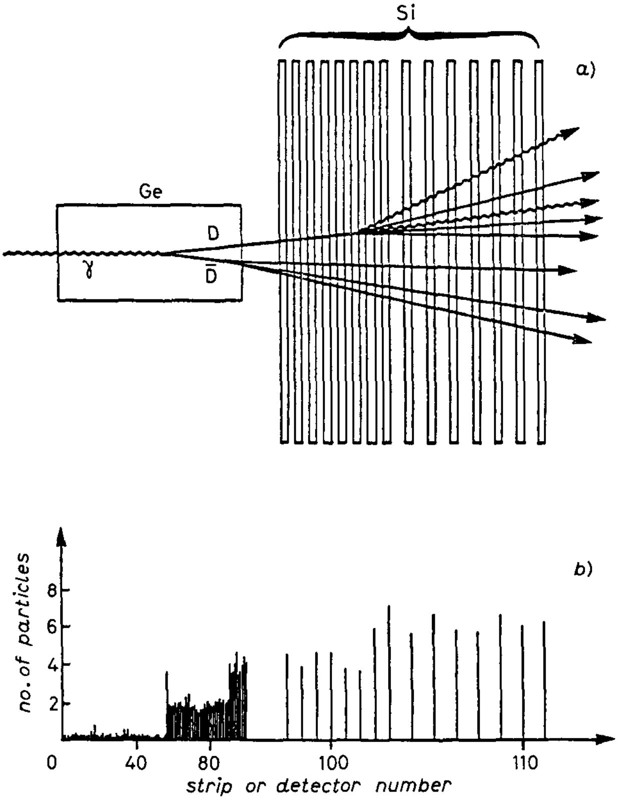

Fig. 1.6. – *a*) FRAMM composite active target using a Ge bulk detector followed by a silicon telescope. *b*) Event detected in the target.

Another application of a telescope of solid-state detectors is the evaluation of charged multiplicity of minimum-ionizing particles. The multiplicity is determined from the total energy released in the telescope. Its segmented structure allows the monitoring of the energy deposited in the individual cells, thereby reducing false multiplicity attributions that may arise from secondary interactions in the detectors. A real-time trigger based upon the difference in multiplicities sensed by two telescopes T_1 and T_2 has been realized as shown in fig. 1.7 [12, 13]. From the multiplicity variation between T_1 and T_2, a possible decay occurring in the gap between them can be detected. Such a principle is employed to trigger on charm decays in the WA 71 experiment.

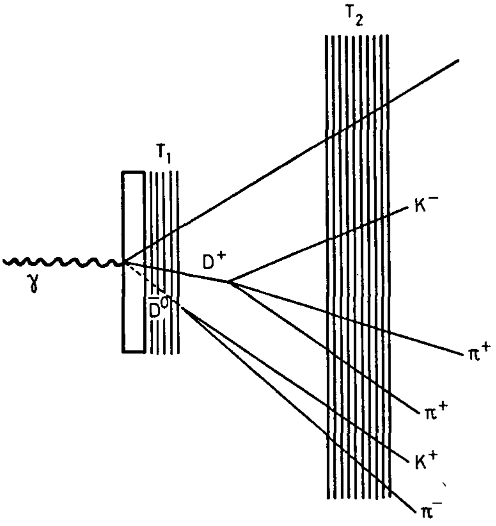

Fig. 1.7. – Real-time trigger based upon two telescopes T_1 and T_2.

A silicon position-sensitive device, the microstrip detector, is already being used in several experiments and extensive use of it is being planned for the future experiments at LEP, at the FNAL Tevatron and collider and elsewhere [8, 14-21].

The structure of a microstrip plane, developed with the same technology of the detector of fig. 1.4, is shown in fig. 1.8.

The structure is similar, to some extent, to the Ge bulk detector; the microstrip plane is much thinner, (200÷300) μm, and is intended for beam incidence almost orthogonal to the strip plane. The position along the x-axis where a track crosses the detector is sensed by that particular strip which collects the charge carriers.

Values of the pitch as small as 20 μm have already been realized; the lower

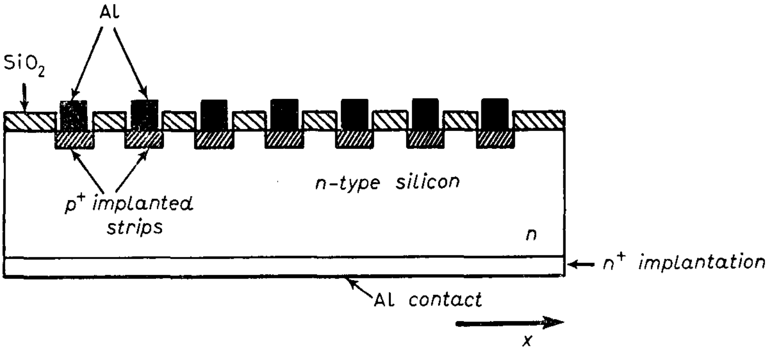

Fig. 1.8. – Microstrip plane.

limitation to the pitch rather than from the detector technology is set by other considerations.

First, considerations of physical nature, according to which, reducing the pitch below a certain limit would be meaningless, for the charge cloud being collected has its own natural width determined by charge diffusion and charge repulsion effects. The importance of these effects can, however, be attenuated by some kind of coarse interpolation.

If the microstrip detector operates in a strong magnetic field, degradation on the space resolution has also to be expected. Experimental investigation about the limits to the achievable spatial resolution with microstrip detectors or arrays of them has been recently carried on [22]. Feasibility of r.m.s. inaccuracies down to 3 to 5 μm, depending on the readout method, has been demonstrated.

A second consideration about the lower limit to the pitch reflects the engineering difficulty in fanning out the signal lines from the detector to the readout electronics. An example of what the fanning-out printed-circuit board looks like is shown in fig. 1.9. The microstrip detector of fig. 1.9 has a 50 μm pitch.

The present interest for microstrip detectors in elementary-particle physics

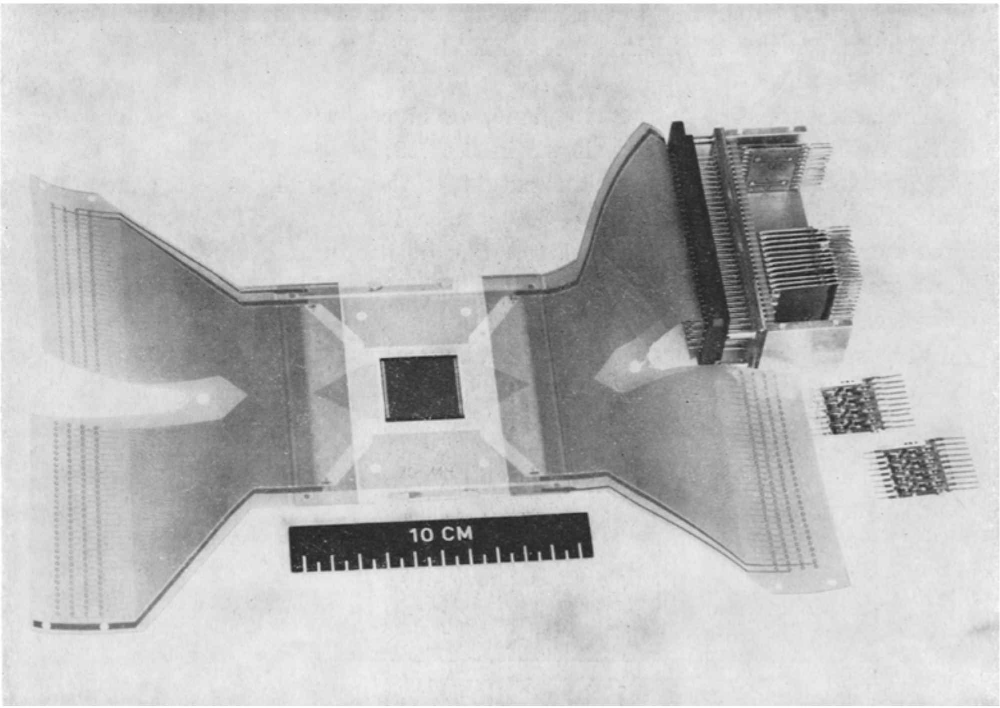

Fig. 1.9. – Printed-circuit board used to fan out the signals from the strips to the readout electronics. (Courtesy of CERN.)

is connected with the possibility of realizing a vertex detector based upon microstrip planes.

An example of this kind of application is shown in fig. 1.10, where an active target made of silicon detectors is associated with a microstrip vertex detector.

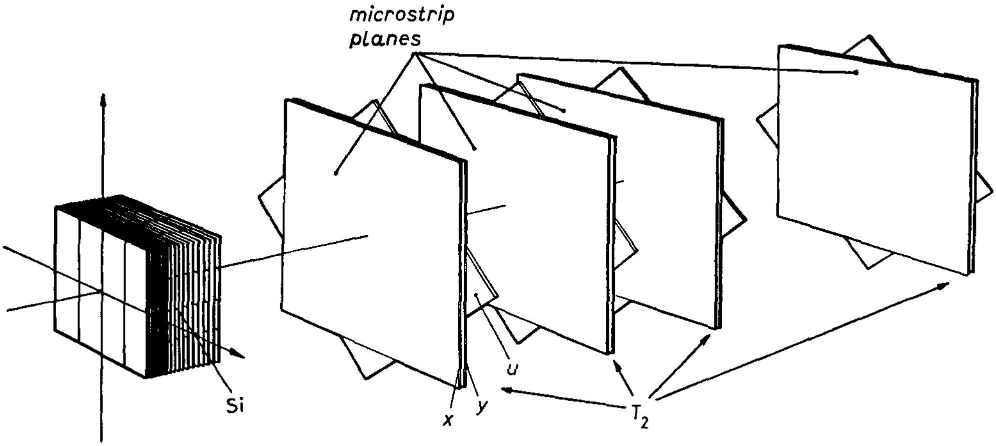

Fig. 1.10. – Silicon active target and microstrip vertex detector of FNAL E687.

The system is intended for investigation about charm and beauty decays, to be performed at the Fermilab Tevatron within the E687 experimental set-up [23, 24]. Several vertex detectors based upon microstrip planes are presently being designed for collider experiments.

An example of barrel-shaped vertex detector intended for one of LEP experiments is illustrated in fig. 1.11 [25, 26].

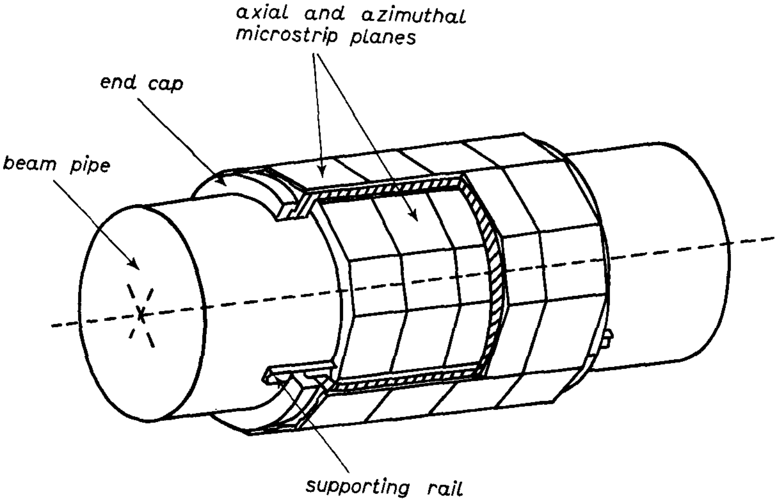

Fig. 1.11. – Barrel-shaped vertex detector employing microstrips.

Other silicon devices for position sensing and tracking applications deserve attention. One of them is the two-dimensional CCD [27, 28]. Such a device allows accurate position sensing in two co-ordinates, has an excellent two-track resolution and presents the advantage of a built-in analog readout. Using a CCD with cells of $22\times22\ \mu\text{m}^2$ pixel size, resolutions of 4.3 and 6.1 μm r.m.s. in two orthogonal directions were achieved.

The second device, the silicon drift chamber, is of very recent realization and is presently undergoing tests on the beam [29, 30]. Based upon a novel charge transport scheme, the silicon drift chamber allows accurate position sensing, yet requiring a limited number of readout channels, 1 or 2 per cm for a resolution of 4 to 8 μm r.m.s.

The principle of the silicon drift chamber is shown in fig. 1.12.

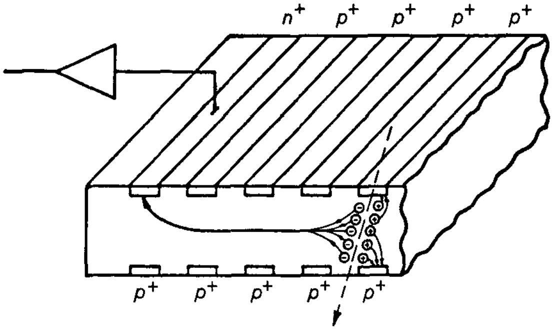

Fig. 1.12. – Silicon drift chamber.

The drift chamber is a fully depleted silicon detector with the space charge of the donors providing a potential well for the electrons. The electrons are so confined in the middle plane of the detector, parallel to its upper and lower surfaces. The confinement of the electrons is shown in fig. 1.12, where the holes created by the ionizing track drift towards the upper and lower p^+ electrodes, while the electrons are confined in the middle plane. The electrons have now to drift towards a collecting electrode. Drifting is obtained with a uniform electric field parallel to the wafer surfaces. Such a field is provided for, by keeping the corresponding p^+ strips of the upper and lower arrays at voltages that are negative with respect to the collecting anode and scaled down of a suitable quantity from one strip to the next one. The drift field determines a uniform motion of the primary electrons towards a low-capacitance n^+ collecting electrode implanted on one side of the wafer as last electrode of one of the arrays of p^+ field electrodes of fig. 1.12.

The surface of electron potential energy in the drift region of the detector for two different values of the voltage difference between two contiguous electrodes is shown in fig. 1.13.

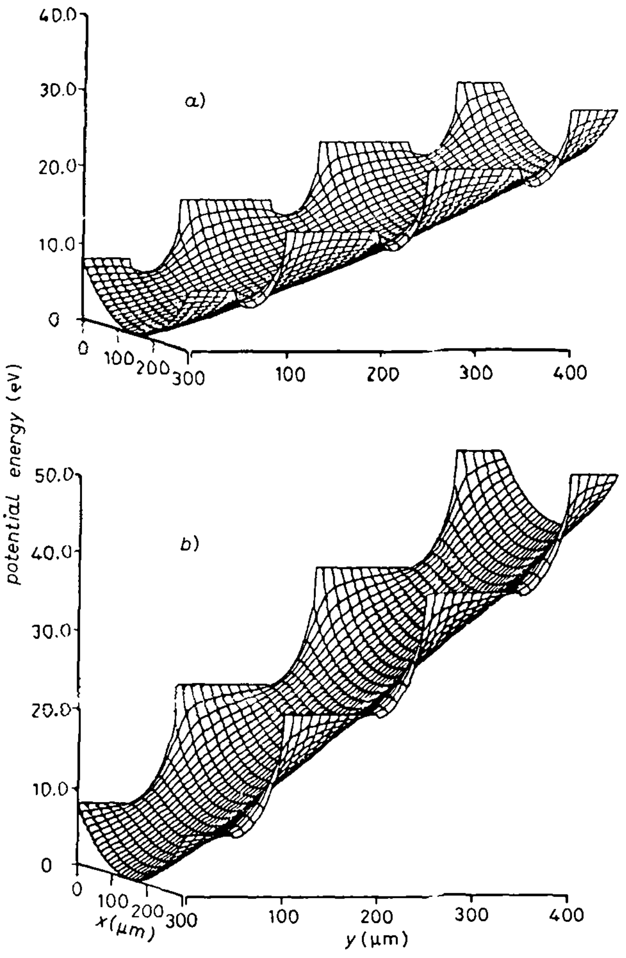

Fig. 1.13. – Potential energy of the electrons in the drift region: *a*) voltage difference between two contiguous p^+ strips 7.5 V, *b*) voltage difference between two contiguous p^+ strips 15 V.

The configuration of the potential surface near the collecting anode is shown in fig. 1.14.

Primary electrons due to a ionizing particle crossing the detector drift and diffuse before reaching the anode. The current pulse at the anode, which is shielded by the arrays of field electrodes, has a Gaussian shape nearly equal to the Gaussian space distributions of the electrons as they reach the anode.

Employed as a position-sensitive or tracking device the silicon drift chamber implies a measurement of the drift time, or interval elapsing between a trigger event in close time relationship with the radiation crossing the detector and a machine time defined on the bunch of electrons at the anode.

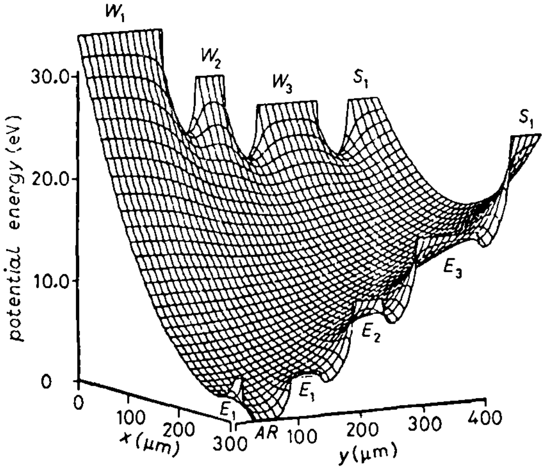

Fig. 1.14. – Potential energy of electrons in the anode region *AR*.

In these applications the silicon drift chambers have as a limitation a poor double-track resolution and ambiguities in the attribution of pulses to multiple triggers that may occur during a drift time interval.

The silicon drift chambers can be also employed for energy measurements and assembled into telescopes to sample the specific energy losses in the beam direction. For these applications they feature a very good energy resolution because the charge created by the ionizing radiation is made available at the output on a low-capacitance electrode.

Silicon is opening his way also in calorimetry [31-33].

Prototypes of calorimeters where the sampling cells are made of silicon detectors are presently being investigated and the results produced so far are well encouraging.

The main task of the present paper is to discuss the problems associated with the solid-state devices reviewed so far.

In some situations, accurate measurements of the energy released in the detectors are required, like in the case of the reconstruction of the ionization density along the beam, or in the charged-multiplicity evaluation, or in silicon calorimetry applications.

In some other cases it has to be distinguished whether an output signal can be safely attributed to a ionizing radiation crossing to the detector or whether it is an artifact determined by the electronic noise. This distinction has to be made in connection with microstrip detectors employed in the strip-by-strip readout mode or with CCDs, where a time slot may or may not contain the information of a particle detected. Other devices may require different kinds of measurements, like, for instance, time measurements in the case of silicon drift chambers.

Regardless of the type of signal processing required, however, the relative importance of detector signal, electronic noise and noise associated with the signal itself determines the accuracy with which the information can be extracted from the signal available at the output of the linear-amplifier system.

In order to introduce the concepts of signal and noise, it will be assumed that a beam of minimum-ionizing particles with a very narrow momentum distribution crosses a thin solid-state detector. The spectrum of the charge of the current pulses at the detector output looks like curve *b*) of fig. 1.15. The following effects contribute to the line broadening.

They are

I) Landau fluctuations in the energy deposited in the detector,

II) statistics in the process of charge creation in the detector for events corresponding to the same energy release,

III) stochastic noise in the preamplifier.

Effect II) is of negligible importance, compared to I) and III) in high-energy physics where the energies deposited in the detectors are small, and where the Landau fluctuations dominate the statistics of the charge appearing at the detector output. The contribution of the electronic noise to the spectral line width can be disentangled from the curve *b*) of fig. 1.15 by injecting at the preamplifier input charge pulses and accumulating the resulting spectrum when the beam is off. The noise line is represented by the shaded peak in fig. 1.15. In this example the contribution of the electronic noise to the total width of the Landau distribution is large, as a result of a poor signal-to-noise ratio determined by the big capacitance of the detector employed.

Generally speaking, the relative importance of Landau fluctuations and electronic noise in determining the final line broadening is related to the following considerations.

At low multiplicities, the effect of noise may be dominant. It has to be pointed out, indeed, that the solid-state detectors have no built-in charge multiplication, that is, the output charge is equal to the one made available by the primary ionization process. Such a charge is determined by the specific energy loss, about 270 eV/μm in silicon and 550 eV/μm in germanium for minimum-ionizing particles, and by the depth of the depleted region in the detecting devices.

With the exception of the germanium bulk detector and of silicon detectors for some calorimetric applications, the practical depletion depths range from about 10 μm in the case of CCDs to about 400 μm in microstrip detectors and telescope layers. Thicker detectors are not used because they would be too slow and, in the case of the microstrip devices, they would present too much material either on the beam or on the tracks emerging from a vertex.

The charge created by one minimum-ionizing particle can be estimated to be in the range 10^3 to $3\cdot10^4$ electrons.

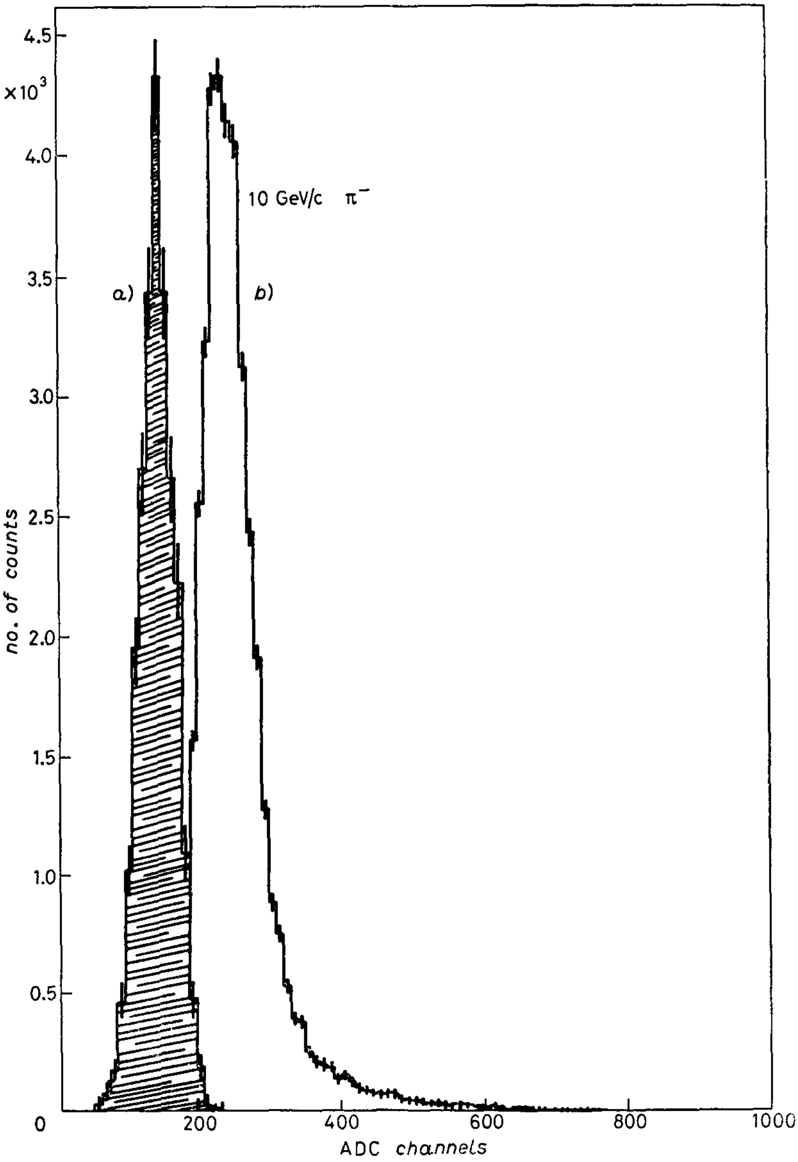

Fig. 1.15. – Landau distribution of the energies released by minimum-ionizing particles in a thin silicon detector (*b*)) and noise line (*a*)). Noise linewidth ENC 4600 e⁻ FWHM, Si 40 keV.

The extent to which the electronic noise affects the accuracy in the charge measurement depends on the detector capacitance and on the time available for the measurement of the single events.

As the radiation multiplicity increases, Landau fluctuations become the dominant source of line broadening and the relative importance of the electronic noise is accordingly reduced. Recently, attention has been conveyed on the investigation about the specific energy losses of minimum-ionizing particles in thin silicon layers [34-37]. Corrections of the classical Landau-Vavilov relation have been suggested.

The limitations in the use of solid-state detecting devices coming from the fluctuations in the energy released will not be discussed in this paper, which is entirely oriented to the instrumental limitations [38]. Among them, as already pointed out, the electronic noise assumes a great importance. Energy measurements with any of the detecting devices presented so far imply the measurement of a charge delivered by a capacitive source with the best possible accuracy compatible with the noise in the amplifying system. The problem is schematically introduced in fig. 1.16, where C_D is the detector capacitance and e_N the total r.m.s. noise referred to the input of the amplifier system.

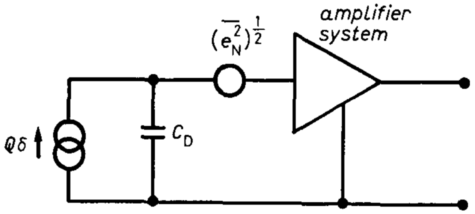

Fig. 1.16. – Basic diagram of a charge-measuring system.

The effect of the preamplifier noise can be described by saying that an infinitely narrow probability density function of detector charge would appear, at the amplifier output, as a Gaussian distribution with variance $\overline{e_N^2}C_D^2$. The quantity $(\overline{e_N^2}C_D^2)^{\frac{1}{2}}$ is called equivalent noise charge referred to the amplifier input; it is represented with the symbol ENC and usually expressed in r.m.s. electrons. The effect of the amplifier noise on the performances of some of the devices considered in this section will be illustrated by a few examples.

In an active target of the type shown in fig. 1.1, the electronic noise may mask a signal variation occurring from one detector to the next one, thereby giving a false attribution of the point at which a multiplicity change occurs.

The electronic noise affects the accuracy in the position identification made with a detector of the type of fig. 1.5 in a similar way.

In the case of a microstrip plane, the need of achieving an adequately small electronic noise is clarified by fig. 1.17. In this example, it is assumed that the microstrip detector is read out by a system which has one channel on every strip, each channel consisting of an amplifier and a discriminator. The two spectra shown in fig. 1.17 are the noise line and the one-particle Landau distribution, whose low-energy edge is determined to a large extent again by the electronic noise. It is evident from fig. 1.17 that, if the ENC is not suitably small in comparison to the Q_1-Q_0 separation, the overlap between the noise line and the Landau spectrum makes the choice of the discriminator threshold Q_T critical. In other words, it becomes impossible to find a value of Q_T which ensures in the meantime a low probability of spurious hits and a high detection efficiency. It can be shown, for instance, that, putting the requirements of less than 0.1% probability of spurious hits and less than 0.1% inefficiency and taking into account a possible charge division between adjacent strips, the ENC must satisfy the relationship

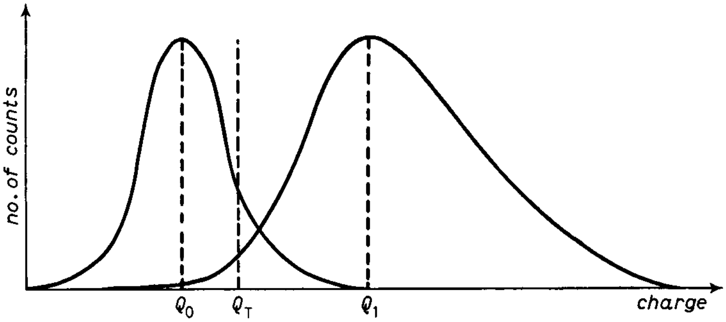

Fig. 1.17. – Effect of electric noise on the microstrip readout.

$$\text{ENC} \leqslant 450\,d \text{ electrons r.m.s.}, \tag{1.1}$$

with d detector thickness in units of 100 μm [39]. So, for instance, a 200 μm strip detector requires an amplifier with less than 900 electrons r.m.s.

If in a microstrip detector the position is read out by some kind of interpolation method, like, for instance, charge division, the considerations about the effects of the noise are different, though the achievement of a high resolution in the position evaluation still requires that the preamplifier noise be kept as small as possible.

Silicon drift chambers employed in energy measurements are subject to the same considerations made with reference to figure 1.16, where now C_D is meant to be the capacitance of the collecting anode, which, as already pointed out, is considerably smaller than the output capacitance of a conventional detector with the same thickness and active area.

When used as a position-sensitive or tracking device, the information processing associated with it has the purpose of measuring with the best accuracy the time taken by the electrons to drift to the collecting anode with reference to a trigger signal.

Typical drift times to achieve the best resolution are 2.5 μs per 5 mm drift, as determined by a 135 V/cm drift field.

Silicon drift chambers have been tested with up to 2500 V/cm drift field and corresponding drift times of 140 ns per 5 mm drift with a factor 4 loss in resolution. If a pulse processor matched to the shorter pulses were employed, the degradation in resolution would be only 1.3.

A typical pulse processor for silicon drift chambers consists of a preamplifier for low detector capacitance, of a quasi-Gaussian amplifier, 175 ns FWHM, followed by a differentiator which delivers a bipolar shape very close to the optimum zero-crossing timing response. Again the preamplifier noise represents a dominant limitation in the achievable position resolution.

Since the solid-state detecting devices made their first appearance in elementary-particle physics, the problem of designing low-noise electronics capable of coping with the peculiar experimental situations had to be faced. If it is true that the fundamentals of signal and noise theory for capacitive sources were known since a long time and that they were extensively employed in low-energy nuclear spectroscopy, it is also true that research and development work was needed to transfer that knowledge into high-energy physics.

For instance, in fixed-target experiments, silicon devices of the telescope type are employed at counting rates up to two orders of magnitude higher than the rates met in nuclear spectroscopy. The effort directed to reduce the noise at short processing times has extended the interest from the junction field-effect transistor to alternative types of amplifying devices. Problems related to very large detector capacitances and under the constraint of the high counting rates had to be solved. The need of achieving outstanding baseline stabilities at high counting rates without sacrificing the intrinsically poor signal-to-noise ratio had to be satisfied. The growing number of detecting channels in each experiment requires compact, low-noise circuitry in the front-end. Hybrid preamplifiers are already of current use, while low-noise monolithic design is being carried on, to solve the problems related to the signal extraction from microstrip detectors of small pitch [40, 41].

Moreover, degradation in signal-to-noise ratio and counting rate performances due to the long connections between beam line and counting room must be avoided.

To conclude, the instrumentation which extracts the information from solid-state devices in elementary-particle physics must be thought about with a number of constraints borne in mind.

The present paper, which aims at discussing the criteria of signal processing for solid-state detectors in elementary-particle physics, will analyse the solutions that have to be adopted to achieve the best performances from the detecting devices reviewed in this section.

REFERENCES

[1] G. Bellini, M. Di Corato, P. F. Manfredi and G. Vegni: *Nucl. Instrum. Methods*, **107**, 85 (1973).

[2] M. Artuso, P. D'Angelo, E. Gatti, P. F. Manfredi and D. Marioli: *High rate pulse processing system for silicon active target*, in *Proceedings of the X International Symposium on Nuclear Electronics, Dresden, G.D.R., 10-16 April 1980*, Vol. **2** (1980), p. 24.

[3] G. Bellini, L. Foà and M. Giorgi: *Phys. Rep.*, **83**, 9 (1982).

[4] G. Bellini, P. D'Angelo, M. Di Corato, D. Marioli, C. Meroni, E. Meroni, L. Moroni, C. Palazzi-Cerrina, F. Palombo, F. Ragusa, S. Sala and G. Vegni: *Live targets as a tool to study short range phenomena in elementary particle physics*, in *Proceedings of the Meeting on Minaturization of High Energy Physics Detectors, Pisa, September 1980*, edited by A. Stefanini (Plenum Press, New York, N. Y., 1983), p. 41.

[5] G. Bellini, P. D'Angelo, P. F. Manfredi, E. Meroni, L. Moroni, C. Palazzi-Cerrina and F. Ragusa: *Nucl. Instrum. Methods*, **196**, 351 (1982).

[6] J. Kemmer: *Nucl. Instrum. Methods*, **169**, 499 (1980).

[7] J. Kemmer, P. Burger, R. Henck and H. Heijne: *Performance and application in high energy physics of passive ion implanted silicon detectors*, in *Proceedings of the Conference on the Search for Charm, Beauty and Truth at High Energies, Erice, November 15-22, 1981*, edited by G. Bellini and S. C. C. Ting (Plenum Press, New York, N. Y., 1984), p. 269.

[8] A. Menzione: *Latest results on silicon detector development ot Pisa*, in *Proceedings of a Workshop on Silicon Detectors for High Energy Physics, Fermilab, October 15-16, 1981*, edited by T. Ferbel (1981), p. 219.

[9] S. R. Amendolia, F. Bedeschi, E. Bertolucci, D. Bettoni, L. Bosisio, C. Bradaschia, M. Budinich, M. Dell'Orso, F. Fidecaro, L. Foà, E. Focardi, P. Giannetti, A. Giazotto, M. A. Giorgi, P. S. Marrocchesi, A. Menzione, L. Ristori, A. Scribano, A. Stefanini, G. Tonelli, G. Triggiani, E. E. Haller, W. L. Hansen and P. N. Luke: *IEEE Trans. Nucl. Sci.*, NS-**30**, 98 (1983).

[10] S. R. Amendolia, F. Bedeschi, E. Bertolucci, D. Bettoni, L. Bosisio, U. Bottigli, C. Bradaschia, M. Dell'Orso, F. Fidecaro, L. Foà, E. Focardi, P. Giannetti, M. A. Giorgi, P. S. Marrocchesi, A. Menzione, G. Raso, L. Ristori, A. Scribano, A. Stefanini, R. Tenchini, G. Tonelli, G. Triggiani, E. Haller, W. L. Hansen and P. N. Luke: *IEEE Trans. Nucl. Sci.*, NS-**31**, 945 (1984).

[11] S. R. Amendolia, G. Batignani, F. Bedeschi, G. Bellini, E. Bertolucci, D. Bettoni, G. Bologna, L. Bosisio, C. Bradaschia, M. Budinich, P. D'Angelo, M. Dell'Orso, B. D'Ettorre Piazzoli, F. L. Fabbri, F. Fidecaro, L. Foà, E. Focardi, P. Giannetti, M. Enorini, M. A. Giorgi, P. Laurelli, F. Liello, P. F. Manfredi, G. Mannocchi, P. S. Marrocchesi, D. Menasce, A. Menzione, E. Meroni, E. Millotti, L. Moroni, D. Pedrini, L. Perasso, P. Picchi, F. Ragusa, L. Ristori, L. Rolandi, S. Sala, A. Scribano, P. Spillantini, A. Stefanini, R. Tenchini, G. Triggiani, G. Tonelli and A. Zallo: *Nucl. Instrum. Methods Phys. Res.*, **226**, 78 (1984).

[12] M. Adamovic, Y. Alexandrov, G. Baroni, S. Benso, N. Crosetti, M. Dameri, G. Darbo, G. Diambrini-Palazzi, P. Ginobbi, E. H. M. Heijne, E. Lamanna, P. F. Manfredi, D. Marioli, F. Meddi, D. Menasce, C. Meroni, S. Micheletti, B. Osculati, S. Petrera, L. Rossi, M. Sannino, S. Tentindo, G. Tomasini, G. Vanderhaeghe, G. Vegni and S. Vitale: *Proposal for an experiment for studying beauty production and lifetime in the upgraded Ω spectrometer*, CERN-SPSC/81-18 SPSC/P159 (20 February 1981).

[13] S. Benso, M. Dameri, G. Diambrini Palazzi, P. F. Manfredi, D. Marioli, C. Meroni, L. Rossi, M. Sannino, S. Tentindo and G. Vegni: *Nucl. Instrum. Methods*, **201**, 329 (1982).

[14] E. H. M. Heijne, L. Hubbeling, B. D. Hyams, P. Jarron, P. Lazyras, F. Piuz, J. C. Vermeulen and A. Wylie: *Nucl. Instrum. Methods*, **178**, 331 (1980).

[15] J. Kemmer, E. Belau, R. Klanner, G. Lutz and B. Hyams: *Development of 10 μm resolution silicon counters for charm signature observation with the* ACCMOR *spectrometer*, in *Proceedings of a Workshop on Silicon Detectors for High Energy Physics, Fermilab, October 15-16, 1981*, edited by T. Ferbel (1981), p. 195.

[16] P. Bonamy, P. Borgeaud, J Movchet and P. G. Rancoita: *Performance of surface barrier and ion implantation silicon microstrip detectors*, in *Proceedings of a Workshop on Silicon Detectors for High Energy Physics, Fermilab, October 15-16, 1981*, edited by T. Ferbel (1981), p. 257.

[17] B. Hyams, U. Koetz, E. Belau, R. Klanner, G. Lutz, E. Neugebauer, A. Wylie and J. Klemmer: *Nucl. Instrum. Methods*, **205**, 99 (1983).

[18] R. Bayley, E. R. Belau, T. Bohringer, M. Bosman, V. Chabaud, C. Damerell, C. Daum, G. De Rijk, H. Dijkstra, A. Dwurazny, S. Gill, A. Gilmmann, R. Gilmore, L. Görlich, Z. Hajduk, C. Hardwich, W. Hoogland, B. D. Hyams, J. Kemmer, R. Klanner, U. Kötz, G. Lütjens, G. Lutz, J. Malos, W. Männer, E. Neugebauer, G. Polok, M. Rozanska, K. Rybicki, H. J. Seebrunner, U. Stierlin, R. J. Tapper, H. G. Tiecke, M. Turala, G. Waltermann, P. Weilhammer, F. Wickens, L. W. Wiggers, A. Wylie and T. Zeludziewicz: *Nucl. Instrum. Methods Phys. Res.*, **226**, 56 (1984).

[19] S. R. Amendolia, F. Bedeschi, E. Bertolucci, D. Bettoni, L. Bosisio, U. Bottigli, C. Bradaschia, M. Dell'Orso, F. Fidecaro, L. Foà, E. Focardi, P. Giannetti, M. A. Giorgi, P. S. Marrocchesi, A. Menzione, G. Raso, L. Ristori, A. Scribano, A. Stefanini, R. Tenchini, G. Tonelli and G. Triggiani: *Nucl. Instrum. Methods Phys. Res.*, **226**, 82 (1984).

[20] E. Engels jr., S. Mani, D. Plants, P. F. Shepard, R. Wilkins and S. Hossain: *Nucl. Instrum. Methods Phys. Res.*, **226**, 59 (1984).

[21] P. E. Karchin, D. L. Hale, R. J. Morrison, M. S. Witherell, M. D. Sokoloff, A. Kiang, B. R. Kumar, J. F. Martin and M. Sarabura: *IEEE Trans. Nucl. Sci.*, NS-**32**, 612 (1985).

[22] E. Belau, R. Klanner, G. Lutz, E. Neugebauer, H. J. Seebrunner, A. Wjlie, T. Böringer, L. Hubbeling, P. Weilhammer, J. Kemmer, U. Kötz and M. Riebesell: *Nucl. Instrum. Methods*, **214**, 253 (1983).

[23] *Fermilab Agreement* E-687, *High energy photoproduction of states containing heavy quarks and other rate phenomena* (21 October 1983).

[24] G. Bellini, M. Di Corato, M. Gianmarchi, P. F. Manfredi, D. Menasce, E. Meroni, L. Moroni, D. Pedrini, L. Perasso and S. Sala: *Nucl. Instrum. Methods Phys. Res.*, **225**, 619 (1984).

[25] *Technical Report* ALEPH *Collaboration* (April 1983), 9.1-9.5.

[26] *Delphi Progress Report*, CERN/LEPC 84-16 (September 1984), p. 23.

[27] P. Bailey, C. J. S. Damerell, R. L. English, A. R. Gillman, A. L. Lintern, J. J. Watts and F. J. Wickens: *Nucl. Instrum. Methods Phys. Res.*, **213**, 210 (1983).

[28] C. Damerell: *Nucl. Instrum. Methods Phys. Res.*, **226**, 26 (1984).

[29] E. Gatti, P. Rehak and J. T. Walton: *Nucl. Instrum. Methods Phys. Res.*, **226**, 129 (1984).

[30] E. Gatti, A. Longoni, P. Rehak, J. Kemmer, P. Holl, R. Klanner, G. Lutz and A. Wylie: *Nucl. Instrum. Methods Phys. Res. A*, **235**, 224 (1985).

[31] G. Barbiellini, G. Cecchet, J. Y. Hemery, F. Lemeilleur, C. Leroy, G. Levman, P. G. Rancoita and A. Seidman: *Nucl. Instrum. Methods Phys. Res.*, **235**, 55 (1985).

[32] G. BARBIELLINI, K. BUKSH, G. CECCHET, J. Y. HEMERY, F. LEMEILLEUR, P. G. RANCOITA, G. VISMARA and A. SEIDMAN: *Nucl. Instrum. Methods Phys. Res. A*, **235**, 216 (1985).
[33] A. NAKAMOTO, H. MURAKAMI, T. DOKE, J. KIKUCHI, K. MASUDA, K. KASAHARA, K. MITSUI, Y. MURAKI and T. YUDA: *A* Si(Li)-Pb *shower calorimeter for* p-$\bar{\text{p}}$ *collider experiments*, report of the Institute for Cosmic Ray Research, University of Tokyo, Japan (28 November 1984).
[34] P. G. RANCOITA and A. SEIDMAN: *Riv. Nuovo Cimento*, **5**, No. 7 (1982).
[35] P. G. RANCOITA: *J. Phys. G*, **10**, 299 (1984).
[36] S. HANCOCK, F. JAMES, J. MOVCHET, P. G. RANCOITA and L. VANROSSUM: *Nucl. Instrum. Methods Phys. Res. B*, **1**, 16 (1984).
[37] G. HALL: *Nucl. Instrum. Methods Phys. Res.*, **220**, 356 (1984).
[38] J. T. WALTON: *Nucl. Instrum. Methods Phys. Res.*, **226**, 1 (1984).
[39] R. KLANNER: *Nucl. Instrum. Methods Phys. Res. A*, **235**, 209 (1985).
[40] E. H. M. HEIJNE and P. JARRON: *Nucl. Instrum. Methods Phys. Res.*, **226**, 12 (1984).
[41] V. RADEKA: *Nucl. Instrum. Methods Phys. Res.*, **226**, 209 (1984).

2. – Shape of the signals delivered by solid-state detectors.

The knowledge of the time dependence of the signals delivered by solid-state radiation detectors is of great importance in the design of the processors that have to operate on them. For this reason, the basic method to evaluate such a time dependence will be presented here. Practical evaluation of current shapes, instead, will be limited to the case of largest application importance, that is, a *P-N* junction detector with planar geometry [1-4].

In the most general case, the evaluation of the output signal at a given electrode of a semiconductor detector requires [5, 6]

a) the knowledge of the initial distributions of electrons and holes;

b) the evaluation of the law of motion for electrons and holes in the electric field determined by the electrode biasing and by the space charge of the doping atoms; the space charge of the carriers created by the ionizing events can be neglected in the case of minimum-ionizing particles;

c) the evaluation of the contribution of every element of charge in motion through a weighting vector $\boldsymbol{E}_{\text{w}}(P)$ which depends on the detector geometry, on the electrical network to which the detector is connected as well as on the velocity $\boldsymbol{u}$ of the charge element under consideration.

These three points will now be discussed in reverse order.

c) *Weighting field* $\boldsymbol{E}_{\text{w}}(P)$. A system of n electrodes connected to a lumped, linear reciprocal electric network will be considered (fig. 2.1).

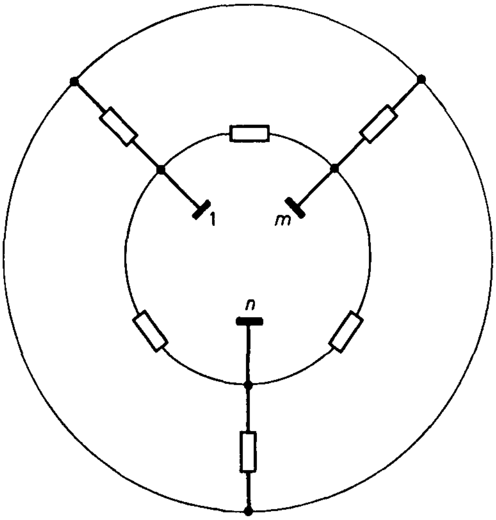

Fig. 2.1. – System of electrodes $1, \ldots, m, \ldots, n$, embedded into a lumped, linear, reciprocal network.

The evaluation of the voltage signal $v_m(t)$ determined by a charge element q on a generic electrode m can be done by applying between m and ground a current generator delivering a δ-impulse and by calculating in the detector volume the weighting electric field $E_{w,v}(P, t)$ due to this generator *alone* (fig. 2.2).

The desired voltage signal $v_m(t)$ is given, by virtue of reciprocity theorems,

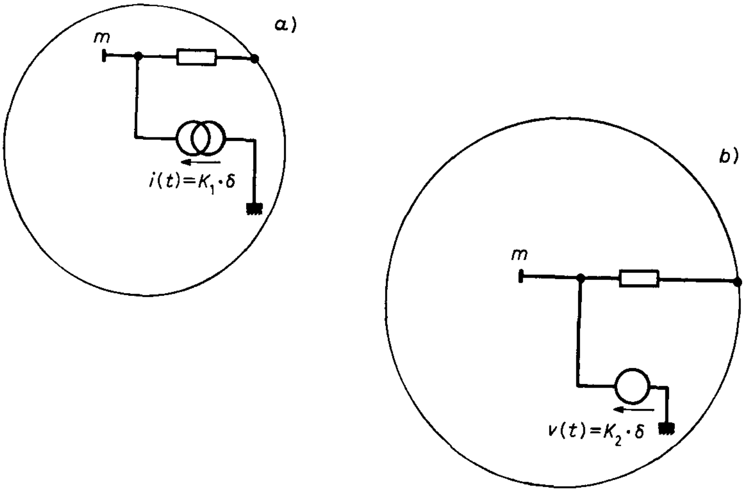

Fig. 2.2. – Evaluation of the voltage signal (*a*)) and of the current signal (*b*)) at the electrode *m*.

by

$$v_m(t) = -\,q\int_{-\infty}^{t}\boldsymbol{E}_{w,v}(P,\, t-\tau)\times\boldsymbol{u}(P(\tau))\,\mathrm{d}\tau\,, \tag{2.1}$$

where the symbol × denotes the scalar product.

In eq. (2.1) $\boldsymbol{u}$ is the velocity of the charge element q at the point P at the instant τ, as determined by the true electric field acting on that element of charge.

To calculate, instead, the current signal $i_m(t)$ induced by the element of charge q, in a conductor shortcircuiting the electrode m to ground, a voltage generator delivering a δ-impulse must be applied between this electrode and ground and the weighting electric field $\boldsymbol{E}_{wi}(P, t)$ in the detector volume and due to this generator *alone* has to be evaluated.

The desired induced current $i_m(t)$, by virtue of reciprocity theorems, is given by

$$i_m(t) = -\,q\int_{-\infty}^{t}\boldsymbol{E}_{wi}(P,\, t-\tau)\times\boldsymbol{u}[P(\tau)]\,\mathrm{d}\tau\,, \tag{2.2}$$

where $\boldsymbol{u}[P(\tau)]$, like in the previous case, is the *true* velocity of the charge element q at the point P and at the instant τ. It has to be pointed out that delayed contributions in the voltage v_m or in the current i_m are generally present. This occurs when the $\boldsymbol{E}_w$ functions have a time dependence which differs from a δ-impulse because of the signals induced on the m electrode by the delayed responses of all the other electrodes embedded in the network.

Only if all the other electrodes are grounded for the signals and neglecting propagation delays, $\boldsymbol{E}_w(P, t)$ can be written as

$$\boldsymbol{E}_w(P, t) = -\,\delta(t)\cdot\operatorname{grad} V_w = \delta(t)\cdot\boldsymbol{E}_{w,\mathrm{static}}\,.$$

Under this hypothesis, the induced current $i_m(t)$, according to (2.2), assumes the well-known expression

$$i_m(t) = -\,q\cdot\boldsymbol{E}_{w,i\mathrm{static}}(P)\times\boldsymbol{u}[P(t)]\,, \tag{2.3}$$

where $\boldsymbol{E}_{w,i\mathrm{static}}(P)$ is the stationary electric field evaluated by connecting the electrode m to potential 1 and all the other electrodes to potential zero.

The general expressions (2.1) and (2.2) are useful in the analysis of detectors with many electrodes not connected to ground, for instance microstrip detectors with capacitive division or delay line readout.

b) *Motion law.* The law of motion for electrons and holes, which in the most adequate form is expressed by $\boldsymbol{u}[P(t)]$, can be calculated in a relatively

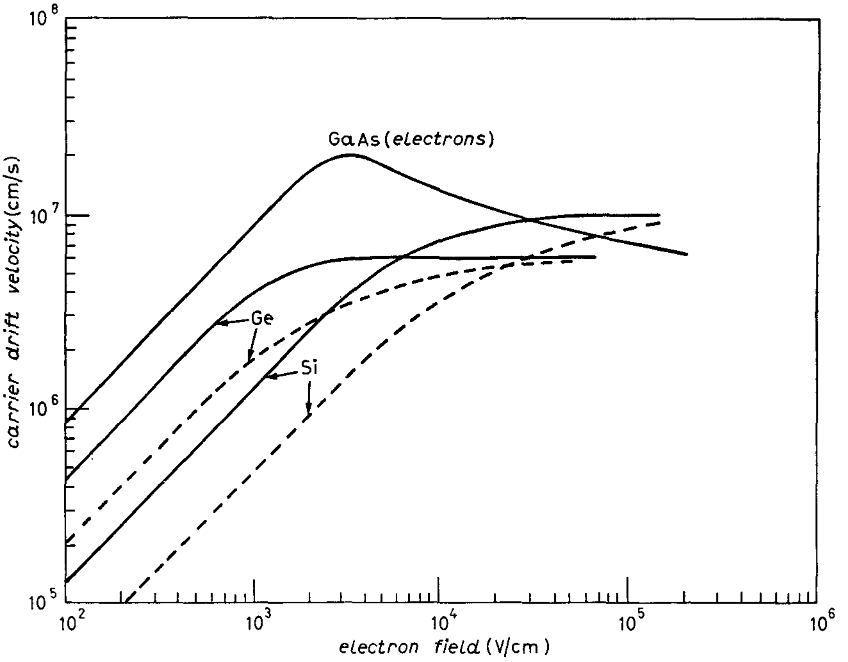

Fig. 2.3. – Carried drift velocity as a function of the electric field for GaAs, Ge and Si at $T = 300$ K: ——— electrons, – – – holes.

easy way once the electron and hole mobilities, μ_e and μ_h, are known, as functions of the electric field. From the curves of fig. 2.3, that represent how the carrier drift velocity depends on the electric field, it can be inferred that at room temperature in silicon the mobilities of both electron and hole have to be considered constant up to an electric field of 4000 V/cm [7]. Their values are, respectively, $\mu_e = 1200$ cm²/V·s and $\mu_h = 450$ cm²/V·s.

a) *Initial charge distribution.* The relationships (2.1) and (2.2) give the partial contributions to the induced voltage and current at time t arising from an elementary bunch of charge q of the initial ionization track. The actual shapes of $v_m(t)$ and $i_m(t)$ are obtained by summing up all the elementary contributions into which the initial track can be split.

As a particular case, a P-N junction with planar geometry will be considered now (fig. 2.4). The detector will be assumed to consist of a heavily doped P^+ region and of a lightly doped N region and the voltage applied larger than the one required to fully deplete the N region.

Let N_D be the concentration of donor atoms supposed to be constant throughout the N region and let w be the detector thickness assumed to be equal to that of the N region. The electric field inside the detector has the linear dependence shown in fig. 2.4 starting from $E_{\min}$ at $x = 0$ and reaching $E_{\max}$

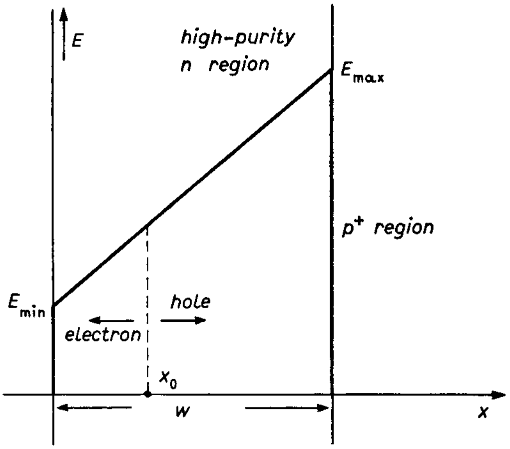

Fig. 2.4. – Electric field inside the *p-n* junction.

at the junction, $x = w$:

$$E(x) = \frac{qN_D}{\varepsilon}\, x + E_{min}\,, \tag{2.4}$$

where ε is the dielectric constant and q the electron charge.

Considering a pair of carriers e, h at the point x_0, the following motion equations can be written:

$$\frac{dx}{dt} = \mu_h \frac{qN_D}{\varepsilon}\, x + \mu_h E_{min} \qquad \text{for the hole}\,, \tag{2.5}$$

$$\frac{dx}{dt} = -\,\mu_e \frac{qN_D}{\varepsilon}\, x - \mu_e E_{min} \qquad \text{for the electron}\,. \tag{2.6}$$

Integrating both equations with the initial conditions $x = x_0$ at $t = 0$, the following time dependences are obtained:

$$x_h = -\frac{\varepsilon}{qN_D} E_{min} + \left(x_0 + \frac{\varepsilon}{qN_D} E_{min}\right) \exp\left[\mu_h q \frac{N_D}{\varepsilon} t\right] \tag{2.7}$$

for the hole, $0 \leqslant t \leqslant t_h$;

$$x_e = -\frac{\varepsilon}{qN_D} E_{min} + \left(x_0 + \frac{\varepsilon}{qN_D} E_{min}\right) \exp\left[-\mu_e q \frac{N_D}{\varepsilon} t\right] \tag{2.8}$$

for the electron, $0 \leqslant t \leqslant t_e$.

In the previous relationships t_h and t_e are the collection times of, respectively, holes and electrons.

The velocities $u_h = dx_h/dt$ and $u_e = dx_e/dt$ for holes and electrons are

$$u_h = \mu_h\left(E_{\min} + \frac{qN_D}{\varepsilon}x_0\right)\exp\left[\mu_h q\frac{N_D}{\varepsilon}t\right], \tag{2.9}$$

$$u_e = -\mu_e\left(E_{\min} + \frac{qN_D}{\varepsilon}x_0\right)\exp\left[-\mu_e q\frac{N_D}{\varepsilon}t\right]. \tag{2.10}$$

The collection times t_h and t_e of hole and electron can be calculated from (2.7) and (2.8). They are

$$t_h = \frac{\varepsilon}{\mu_h qN_D}\ln\frac{w + (\varepsilon/qN_D)E_{\min}}{x_0 + (\varepsilon/qN_D)E_{\min}}, \tag{2.11}$$

$$t_e = \frac{\varepsilon}{\mu_e qN_D}\ln\frac{x_0 + (\varepsilon/qN_D)E_{\min}}{(\varepsilon/qN_D)E_{\min}}. \tag{2.12}$$

According to (2.3) and observing that in the simple geometric configuration of the present detector $|\boldsymbol{E}_{w,i\text{static}}| = 1/w$ and that the velocities $\boldsymbol{u}_h$ and $\boldsymbol{u}_e$ have the same direction as $\boldsymbol{E}_{w,i\text{static}}$, the following expressions can be written for the currents induced by the motion of holes and electrons:

$$i_h(t) = \frac{q}{w}\mu_h\left(E_{\min} + \frac{qN_D}{\varepsilon}x_0\right)\exp\left[\mu_h q\frac{N_D}{\varepsilon}t\right], \qquad 0 \leqslant t \leqslant t_h, \tag{2.13}$$

$$i_e(t) = \frac{q}{w}\mu_e\left(E_{\min} + \frac{qN_D}{\varepsilon}x_0\right)\exp\left[-\mu_e q\frac{N_D}{\varepsilon}t\right], \qquad 0 \leqslant t \leqslant t_e, \tag{2.14}$$

with $i_h(t) = 0$ for $t > t_h$ and $i_e(t) = 0$ for $t > t_e$.

Time integration of (2.13) and (2.14) provides the charge induced on the cathode by both carriers:

$$Q_h = \frac{\varepsilon}{wN_D}\left(E_{\min} + \frac{qN_D}{\varepsilon}x_0\right)\left(\exp\left[\mu_h q\frac{N_D}{\varepsilon}t\right] - 1\right), \tag{2.15}$$

$$Q_e = \frac{\varepsilon}{wN_D}\left(E_{\min} + \frac{qN_D}{\varepsilon}x_0\right)\left(1 - \exp\left[-\mu_e q\frac{N_D}{\varepsilon}t\right]\right). \tag{2.16}$$

Introducing into (2.15) and (2.16) the collection times given by (2.11) and (2.12), the total charges induced by the two carriers on the cathode are obtained:

$$Q_{h,\text{tot}} = q\frac{w - x_0}{w}, \tag{2.17}$$

$$Q_{e,\text{tot}} = q\frac{x_0}{w}. \tag{2.18}$$

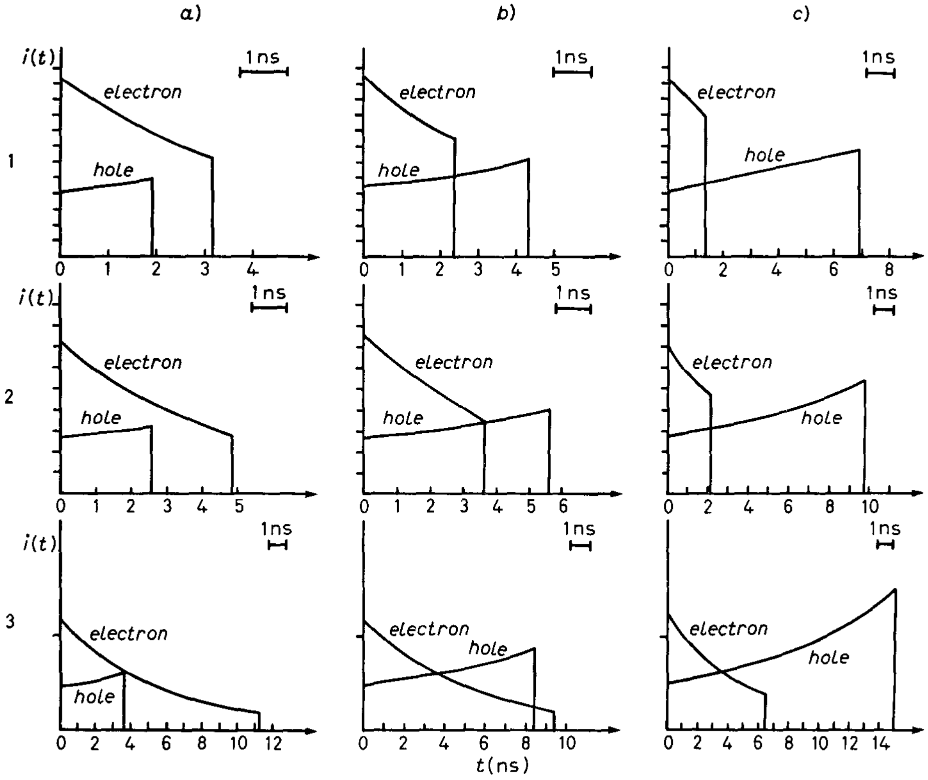

Fig. 2.5. – Shapes of current signals induced on the cathode by an electron-hole pair created at x_0. The columns *a*), *b*), *c*), correspond, respectively, to the values 0.75, 0.5, 0.25 of the x_0/w ratio, while the rows 1, 2, 3 correspond, respectively, to the values 0.9, 0.5, 0.1 of the $E_{\min}/E_{\text{crit}}$ ratio.

The set of curves of fig. 2.5 represents the theoretical shapes of the induced current signals for the combinations of three values of the x_0/w ratio and three values of the ratio $E_{\min}/E_{\text{crit}}$, where $E_{\text{crit}} = (qN_D/\varepsilon)w$ is the smallest electric field at the detector junction which guarantees the total depletion, that is $E_{\min} = 0$ for $E_{\max} = E_{\text{crit}}$. The calculations refer to a detector with $w = 300\ \mu\text{m}$ and $N_D = 10^{12}\ \text{cm}^{-3}$.

The diagrams of fig. 2.5 point out the importance of « over-depleting » the detector, that is, of using a large $E_{\min}/E_{\text{crit}}$ ratio in order to reduce the detector collection times.

In some cases, for instance for the microstrip detectors, the motion of the carriers and the resulting induced currents must be calculated taking into account the diffusion along with the drift. The importance of the diffusion can be evaluated by recalling that the average square deviation $\overline{\Delta r^2}$ with respect to the trajectory without diffusion during a time interval Δt is given by

$$\overline{\Delta r^2} = 2D\Delta t ,$$

where D is the diffusion coefficient of either type of carrier in silicon. The values of $2D$ are 60 cm²/s (6 μm²/ns) for the electrons and 22 cm²/s (2.2 μm²/ns) for the holes. Correspondingly, the squared time spread is $\overline{\Delta t^2} = 2D(\Delta t/u^2)$ and summing these variances, for a time-of-flight t_f,

$$\overline{\Delta t_f^2} = 2D\int_0^{t_f} \frac{dt}{u^2}\,.$$

REFERENCES

[1] S. RAMO: *Proc. IRE*, **27**, 584 (1939).

[2] C. K. JEN: *Proc. IRE*, **29**, 345 (1941).

[3] R. E. COLLIN: *Fundation for Microwave Engineering* (McGraw-Hill Book Co., New York, N. Y., 1966).

[4] G. CAVALLERI, G. FABRI, E. GATTI and V. SVELTO: *Nucl. Instrum. Methods*, **21**, 177 (1963).

[5] A. H. WALENTA: *Nucl. Instrum. Methods*, **151**, 461 (1978).

[6] E. GATTI, G. PADOVINI and V. RADEKA: *Nucl. Instrum. Methods*, **193**, 651 (1982).

[7] S. M. SZE: *Physics of Semiconductor Devices*, 2nd edition (J. Wiley and Sons, New York, N. Y., 1981).

3. – Optimum least-square measurement of the charge released by a solid-state detector.

3·1. *Statement of the problem.* – In this section the theory of the optimum measurement of the charge delivered by a solid-state detector will be reviewed. The loss in signal-to-noise ratio due to signal processing methods different from the optimum one, but of more practical interest will be evaluated in sect. **4**.

The problem of the optimum signal processing in the measurement of the charge Q delivered by a detector of capacitance C_D, briefly outlined in the introduction, can be presented as a search for a network which allows the best least-square measurement of Q in the presence of the preamplifier noise. The theory of the best least-square measurement will be introduced starting from the model of fig. 3.1.

The detector is modelled as a current source, delivering in an indefinitely short time a charge Q, proportional to the energy released, across the parallel combination of the detector capacitance C_D and of the preamplifier input capacitance C_i. Although the actual preamplifier circuits differ from the simple structure of fig. 3.1, the discussion based upon the voltage-sensitive configuration leads to a more straightforward understanding of the processes involved in the charge measurements and of the noise limitations.

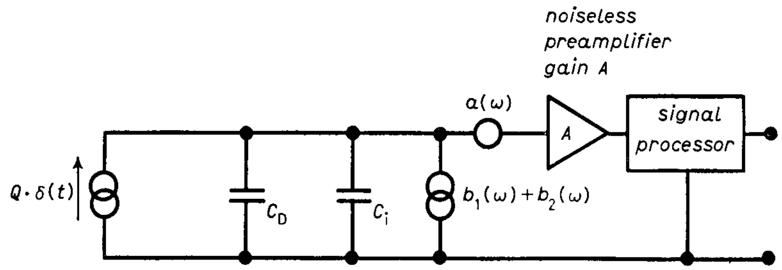

Fig. 3.1. – Analog processor for the measurement of the charge Q.

The final results, moreover, are to a large extent independent of the amplifier configurations.

The noise sources in the whole system are accounted for by a series voltage generator with spectral power density $a(\omega)$ and by a parallel current generator with spectral power density $b_1(\omega) + b_2(\omega)$. While $a(\omega)$ is a characteristic of the preamplifier alone, the parallel noise has been split into two terms, $b_1(\omega)$ including the preamplifier contributions and $b_2(\omega)$ describing the parallel noise associated with the detector and with the bias circuitry of detector and preamplifier. Incidentally, it has to be pointed out that, to describe a linear noisy two-port network, a series and a parallel noise generators with their power spectra $\Sigma_{aa}(\omega) = a(\omega)$, $\Sigma_{bb}(\omega) = b_1(\omega)$ and with the cross-correlation terms $\Sigma_{ab}(\omega)$, $\Sigma_{ba}(\omega)$ are generally required [1-3].

In the cases of interest in nuclear applications, however, the two generators $a_1(\omega)$ and $b_1(\omega)$ can be considered uncorrelated and, therefore, only two spectral power densities will suffice to describe the preamplifier noise. Once the noise is accounted for by the external generators, the preamplifier is represented as a noiseless two-port.

The series voltage source generally consists of a white term a_1 and of a term with a spectral power density of the type $a_2/|\omega|$. The white noise accounts for the shot noise in the collector current in bipolar transistors or for the thermal noise in the channel of field-effect devices. The $a_2/|\omega|$ part of the series power density is of negligible importance in bipolar transistors and silicon junction field-effect transistors as long as their use is limited to elementary-particle physics. The same might not be true for GaAs devices and is surely not true for MOS field-effect transistors, for which the contribution due to the $a_2/|\omega|$ term turns out to be the dominant limitation [4, 5].

The spectral power density $b_1(\omega)$ describes the shot noise associated with the base current in a bipolar transistor or with the gate leakage current in a junction field-effect transistor. In either case b_1 can be considered independent of ω.

The spectral power density $b_2(\omega)$ includes contributions due to the shot noise in the detector leakage current and to the thermal noise in the resistors employed to bias the detector and to provide a d.c. return to the preamplifier input current. These terms are independent of ω.

The noise associated with the dielectric losses, which would add to b_1 and b_2 terms with a linear frequency dependence, is quantitatively of negligible importance in the applications covered by this paper.

The previous discussion leads to the conclusion that the $1/|\omega|$ noise in the input spectrum is important only in one device, the MOS transistor, which cannot be considered, strictly speaking, a true low-noise device. This consideration, along with the remark that such a dependence would considerably increase the mathematical difficulties, suggests that the optimum processing be analysed in the case of white spectra for both series and parallel generators. It will be accordingly assumed $a(\omega) = a$ independent of ω and $b_1(\omega) + b_2(\omega) = b$, also independent of ω. The effect of $1/|\omega|$ noise will be analysed separately, by evaluating its contribution to the total noise in some particular cases. A treatment which extends the discussion to a more general input spectrum is available in the literature [6].

In the foregoing analysis the bilateral representation, ω ranging between $-\infty$ and $+\infty$, will be adopted for the spectral power densities.

Two different methods will be followed to determine the best processing of detector signals. One, which makes use of a time domain approach to synthesize the optimum processor, is due to BALDINGER and FRANZEN [7]. The other one, which extends to the nuclear case the theory of the matched filter with a frequency domain approach, is due to RADEKA and KARLOVAC [8]. Both methods deduce the optimum filter for a single pulse of given shape under the hypothesis that the baseline to which the pulse is referred is known with infinite accuracy. Such a situation is not realistic because the time available for the baseline estimation is limited by the presence of other incoming signals. After the presentation of the methods of Baldinger and Franzen and Radeka and Karlovac, the problem related with the inaccuracies in the baseline estimation will be considered.

3·2. *Time domain approach to optimum processing.* – As a preamble to the time domain approach to optimum processing in the actual case, the following particular situation will be considered. The information about a parameter $\mathscr{A}_1$ is carried by a signal consisting of two rectangular pulses of short width Δt, with amplitudes $\mathscr{A}_1$ and $\alpha\mathscr{A}_1$, occurring at a mutual time distance τ, as in fig. 3.2. The time-dependent part $S(t)$ of the signals is represented by the two rectangles of amplitudes 1 and α.

The signal is added to a noise which is assumed to be of ergodic nature and band-limited white with an upper frequency limitation of the order of $1/\Delta t$.

If the parameter $\mathscr{A}_1$ is determined from the first pulse of fig. 3.2, the signal-to-noise ratio is $\mathscr{A}_1/\langle v_N^2\rangle^{\frac{1}{2}}$, where $\langle v_N^2\rangle^{\frac{1}{2}}$ is the ensemble root-mean-square value of the noise. If $\mathscr{A}_1$ is, instead, determined from the second rectangular pulse, the signal-to-noise ratio is $\alpha\mathscr{A}_1/\langle v_N^2\rangle^{\frac{1}{2}}$, where the ensemble root-mean-square value is the same as before owing to the hypothesis of ergodicity. In both

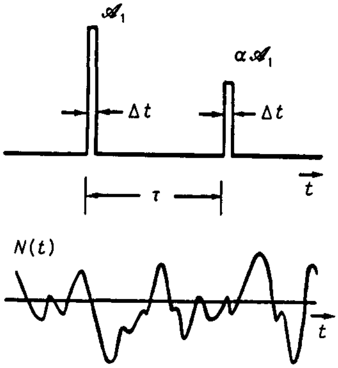

Fig. 3.2. – Best least-square measurement of the parameter $\mathscr{A}_1$ from a signal consisting of two rectangular pulses in the presence of band-limited white noise.

cases a signal-to-noise ratio inferior to the optimum one is achieved, because the full information carried by the signal is not utilized. To fully exploit the information available in the signal, the most general linear processing which consists in the weighted sum of the two pulses will be adopted. The time-variant network which implements it is shown in fig. 3.3.

According to the block diagram of fig. 3.3, a weighting wave form, made of two narrow rectangles of amplitudes 1 and β and synchronous with the two rectangles that constitute the input signal, is triggered.

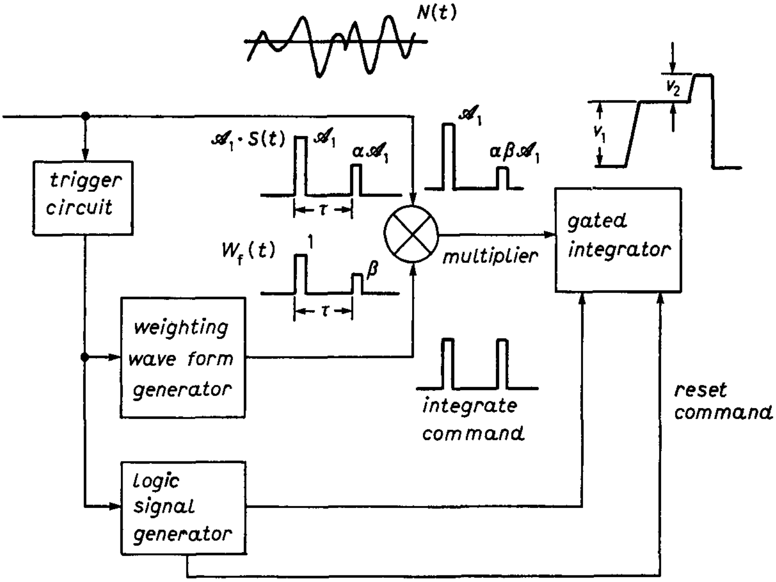

Fig. 3.3. – Time-variant realization of the weighted sum.

An analog multiplier implements the product of the input signal and of the weighting function. The resulting wave form is applied to the input of the gated integrator. At the end of the « integrate command » signal, the voltage stored in the integrator is proportional to $\mathscr{A}_1(1+\alpha\beta)$. At the same instant the noise is proportional to $N(t)+\beta N(t+\tau)$. As the noise is almost white, its autocorrelation function is a very narrow function in the time domain, which means that the two values $N(t)$, $N(t+\tau)$ can be considered uncorrelated.

The ergodic hypothesis ensures that the ensemble root-mean-square values of $N(t)$ and $N(t+\tau)$ are equal. Therefore, the signal-to-noise ratio is

$$\frac{\mathscr{A}_1(1+\alpha\beta)}{(1+\beta^2)^{\frac{1}{2}}\langle v_N^2\rangle^{\frac{1}{2}}}\,. \tag{3.1}$$

Expression (3.1) considered as a function of β has a maximum for $\beta=\alpha$. The maximum signal-to-noise ratio achievable in the measurement of $\mathscr{A}_1$ is, therefore,

$$\frac{\mathscr{A}_1(1+\beta^2)^{\frac{1}{2}}}{\langle v_N^2\rangle^{\frac{1}{2}}}\,,$$

which is a factor $1+\beta^2$ better than the larger of the two signal-to-noise ratios obtained with the information from a single pulse. The circuit of fig. 3.3 represents the time-variant version of the optimum processor, while the time-invariant one is shown in fig. 3.4.

The measurement has to be carried out, in the circuit of fig. 3.4, at $t=\tau$ and the result obtained in this way, with $\beta=\alpha$, corresponds to the best least-square estimate of $\mathscr{A}_1$. The linear processing discussed so far and implemented by either solution 3.3 and 3.4 can be demonstrated to be the best one with respect to any kind of processing [9].

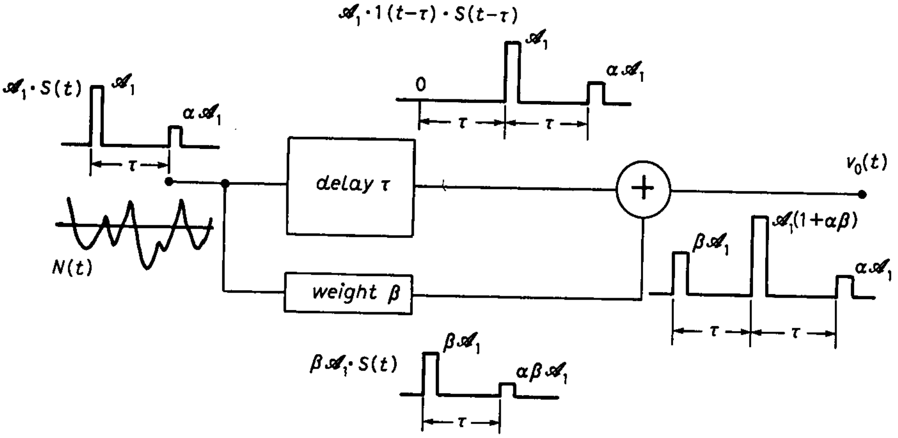

Fig. 3.4. – Time-invariant realization of the network implementing the weighted sum of two pulses.

The circuit of fig. 3.4 responds to a narrow rectangular pulse of unit amplitude with the wave form $v_\delta(t)$ of fig. 3.5. The function $v_\delta(t)$ is the mirror image of the weighting function $w_t(t)$ of fig. 3.5:

$$v_\delta(t) = w_t(\tau - t)\,.$$

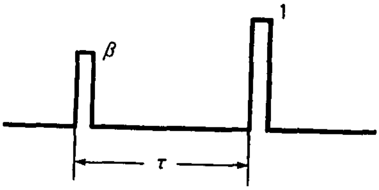

Fig. 3.5. – Response of the time-invariant processor of fig. 3.4 to a narrow rectangle of unit amplitude.

In the optimum situation, $\beta = \alpha$, $v_\delta(t)$ becomes the mirror image of the time-dependent part $S(t)$ of the input signal

$$v_\delta(t) = S(\tau - t)\,.$$

The response $v_0(t)$ of the time-invariant processor of fig. 3.4 to the signal $\mathscr{A}_1 S(t)$ can be interpreted as the convolution of $\mathscr{A}_1 S(t)$ and $v_\delta(t)$.

The previous considerations can be easily extended to the case in which the information about a parameter $\mathscr{A}_1$ is carried by a continuous wave form $\mathscr{A}_1 S(t)$ which can be considered as a sequence of samples of amplitudes $\alpha_1 \mathscr{A}_1$, $\alpha_2 \mathscr{A}_1, \ldots, \alpha_N \mathscr{A}_1$ and $\mathscr{A}_1$ has to be measured with the least-mean-square error in the presence of band-limited white noise.

The optimum processor implements the weighted sum

$$\mathscr{A}_1 \sum_{k=1}^{N} \alpha_k^2\,.$$

Its time-invariant implementation has, as δ-impulse response, the mirror image of $S(t)$

$$v_\delta(t) = S(\tau_N - t)\,.$$

The hypothesis of band-limited white noise is instrumental in making the solution of the optimization problem so simple. If the noise is not white, then the synthesis of the processor which implements the best least-square error measurement has to be split into two steps. One is the synthesis of a filter, called *noise whitening*, which converts the original noise spectrum into a white one. The second step consists in applying the weighted-sum method to the signal at the output of the noise-whitening filter.

The previous considerations will now be applied to the actual case of the nuclear-radiation detector of fig. 3.1. The signal at the preamplifier output is a step of amplitude $(Q/(C_D + C_i))A$ and the noise power spectral density is (see p. 21)

$$A^2\left[a + \frac{b}{\omega^2(C_D + C_i)^2}\right]. \tag{3.2}$$

For instance, a network with transfer function

$$\mathscr{F}_w(s) = \sqrt{\frac{W}{a}}\,\frac{1}{A}\,\frac{s\sqrt{a/b}(C_D + C_i)}{1 + s\sqrt{a/b}(C_D + C_i)}, \tag{3.3}$$

where s is the complex frequency, can transform the noise (3.2) into a white one with spectral power density W.

The *noise-whitening* filter is, therefore, the cascade of a gain element and of an approximate differentiator with time constant

$$\tau_c = \sqrt{\frac{a}{b}}\,(C_D + C_i). \tag{3.4}$$

The time constant τ_c is called « noise corner » time constant and is the reciprocal of that particular angular frequency ω_c at which the contributions from series and parallel noise at the preamplifier input become equal.

As pointed out by (3. 4), the noise corner time constant is determined by the preamplifier series noise, by the total parallel noise and by the total capacitance at the preamplifier input.

At the output of the whitening filter the noise has a spectral density W and the signal has the time dependence

$$\frac{Q}{C_D + C_i}\sqrt{\frac{W}{a}}\exp[-t/\tau_c]\cdot 1(t) = \frac{Q}{C_D + C_i}\sqrt{\frac{W}{a}}\,S_W(t)\cdot 1(t) \tag{3.5}$$

shown in fig. 3.6*a*). It is worth pointing out, in passing, that the transfer function $\mathscr{F}_w(s)$ is not univocally defined by the power spectrum (3.2) and that the filter which has as output signal the mirror image of the response of fig. 3.6*a*) would be a noise-whitening filter as well (fig. 3.6*b*)). At a first glance this second filter looks to be physically unrealizable. However, if the response of fig. 3.6*b*) is truncated to a finite τ_M and a delay equal to or larger than τ_M is introduced, it becomes physically realizable.

Referring, for the sake of simplicity, to the response 3.6*a*) and being the noise at the filter output white, the optimum processor for the measurement of Q can be determined with the already known procedure.

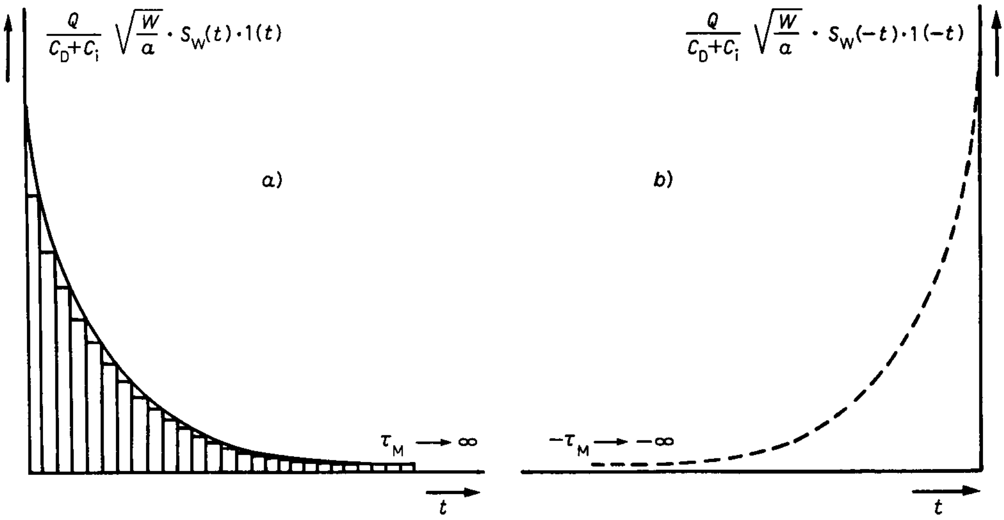

Fig. 3.6. – Signals at the output of noise-whitening filters in response to a δ-impulse detector current of charge Q.

The signal is represented in fig. 3.6*a*) as a time sequence of equally spaced rectangles, each of them having an amplitude proportional to Q.

In the case of an indefinitely long measurement time τ_M the δ-impulse responses of the optimum processors, obtained extending to the continuum case the procedure adopted for the discrete signals of fig. 3.2, are represented in fig. 3.7*a*), *b*), respectively, for the whitening filters of fig. 3.6*a*), *b*).

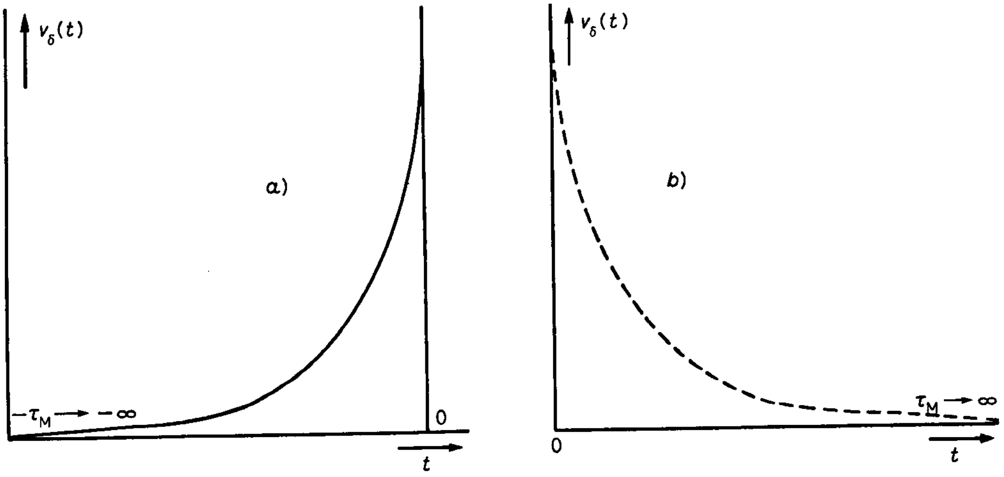

Fig. 3.7. – δ-impulse responses of the optimum processors: *a*) signal at the output of the noise-whitening filter 3.6*a*), the δ is supposed to be applied at $t = -\tau_M$; *b*) signal at the output of the noise-whitening filter 3.6*b*).

The response of the optimum processors to their corresponding input signals, exponentially decaying or exponentially growing, is in either case the indefinite cusp of fig. 3.8.

The measurement of Q requires the evaluation of the peak amplitude of the cusp.

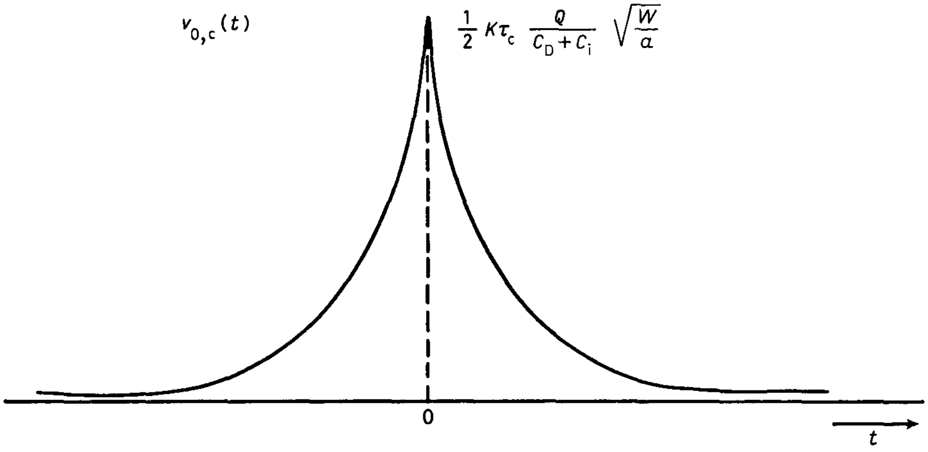

Fig. 3.8. – Response of the optimum processors to the exponentially decaying or exponentially growing pulses at the output of the corresponding noise-whitening filters.

The optimum processors are determined by the time dependence of the signals at the output of the related noise-whitening filters, that is, the processors are matched to those signals. For this reason the theory being developed is also called « matched filter » theory [10]. In order to complete it, the optimum signal-to-noise ratio has now to be evaluated.

To do this, the peak amplitude of the cusp of fig. 3.8 will be calculated at once. According to (3.5) the δ-response of the optimum processor for the exponentially decaying signal is

$$w_i(t) = K\exp[t/\tau_c]\cdot 1(-t)\,, \tag{3.6}$$

where K is an arbitrary constant having the dimension of a frequency. The response of the optimum processor to the exponentially decaying signal is the convolution of (3.5) and (3.6), that is,

$$v_{0,c}(t) = \frac{KQ}{C_D+C_i}\sqrt{\frac{W}{a}}\int_{-\infty}^{\infty}\exp\left[-\frac{\tau_0}{\tau_c}\right]\cdot 1(\tau_0)\exp\left[\frac{t-\tau_0}{\tau_c}\right]\cdot 1(\tau_0-t)\,d\tau_0\,,$$

which is the cusp of fig. 3.8. The function $v_{0,c}(t)$ has a maximum at $t=0$, whose value is

$$(3.7)\qquad v_{0,\mathrm{cmax}} = \frac{KQ}{C_{\mathrm{D}} + C_{\mathrm{i}}} \sqrt{\frac{W}{a}}\, \tau_{\mathrm{c}} \int_{0}^{\infty} \exp\left[-2\,\frac{\tau_0}{\tau_{\mathrm{c}}}\right] \mathrm{d}\left(\frac{\tau_0}{\tau_{\mathrm{c}}}\right) = \frac{1}{2}\, \frac{KQ}{C_{\mathrm{D}} + C_{\mathrm{i}}} \sqrt{\frac{W}{a}}\, \tau_{\mathrm{c}}\,.$$

The root-mean-square noise at the output of the optimum processor can be evaluated from the knowledge of the spectral power density W of the noise at the input and from the transfer function of the optimum processor, which is the Laplace transform of $w_{\mathrm{f}}(t)$ in eq. (3.6):

$$(3.8)\qquad [(\overline{v_{\mathrm{N}}^2})]^{\frac{1}{2}} = \left[\int_{-\infty}^{\infty} W |W_{\mathrm{f}}(j\omega)|^2 \,\mathrm{d}f\right]^{\frac{1}{2}} = \left[-\,W \int_{0}^{-\infty} K^2 \exp\left[\frac{2t}{\tau_{\mathrm{c}}}\right] \mathrm{d}t\right]^{\frac{1}{2}} = \left[\frac{1}{2}\,\tau_{\mathrm{c}} W\right]^{\frac{1}{2}} K\,.$$

In eq. (3.8) $W_{\mathrm{f}}(s)$ is the Laplace transform of $w_{\mathrm{f}}(t)$ and Parseval's theorem has been used to pass from the integral on the frequency domain to the integral in the time domain [11].

The hypothesis of ergodicity ensures that the time average of (3.8) coincides with the ensemble average previously adopted in the evaluation of the signal-to-noise ratio. The optimum signal-to-noise ratio, according to (3.7) and (3.8), is

$$(3.9)\qquad \varrho_{\mathrm{opt}} = \frac{Q}{(C_{\mathrm{D}} + C_{\mathrm{i}})^{\frac{1}{2}}}\, \frac{1}{(4ab)^{\frac{1}{4}}}\,.$$

3'3. *Frequency domain approach to optimum processing.* – An alternative deduction of the matched-filter theory in the frequency domain will now be presented. Let $Q_{\mathrm{i}} S_{\mathrm{i}}(t)$ be the signal carrying the information about the parameter to be measured and let $\mathcal{N}(\omega)$ be the spectral power density of the noise associated with $Q_{\mathrm{i}} S_{\mathrm{i}}(t)$.

The noise is assumed again to be ergodic. The problem of the optimum least-square measurement of the parameter Q_{i} can be stated in the following way. Let $H(s)$ be the *a priori* unknown transfer function of the network which leads to the optimum measurement.

The signal at the output of this network can be written as an inverse Fourier transform

$$(3.10)\qquad v_0(t) = \frac{Q_{\mathrm{i}}}{2\pi} \int_{-\infty}^{\infty} H(j\omega) S_{\mathrm{i}}(\omega) \exp[j\omega t]\, \mathrm{d}\omega\,,$$

where $S_{\mathrm{i}}(\omega)$ is the Fourier transform of $S_{\mathrm{i}}(t)$.

The r.m.s. noise at the output of the same network is

$$(3.11)\qquad \langle v_{\mathrm{N}}^2 \rangle^{\frac{1}{2}} = [\overline{v_{\mathrm{N}}^2}]^{\frac{1}{2}} = \left\{\frac{1}{2\pi} \int_{-\infty}^{\infty} \mathcal{N}(\omega) |H(j\omega)|^2 \,\mathrm{d}\omega\right\}^{\frac{1}{2}},$$

where the ensemble average has been evaluated as a time average thanks to the hypothesis of ergodicity. The unknown function $H(s)$ must be determined so as to maximize the ratio between the value of the signal at the measurement time τ_M and the root-mean-square noise. As the optimization procedure is more easily carried out on the square of this ratio, it can be said that the desired $H(s)$ is the one which makes the ratio

$$\varrho^2 = \frac{Q_i^2}{2\pi} \frac{\left\{ \int\limits_{-\infty}^{\infty} H(j\omega) S_i(\omega) \exp[j\omega\tau_M] \,\mathrm{d}\omega \right\}^2}{\int\limits_{-\infty}^{\infty} \mathcal{N}(\omega) |H(j\omega)|^2 \,\mathrm{d}\omega} \tag{3.12}$$

achieve its maximum value. The existence of an upper limit for (3.12), which turns out to be the required maximum for a particular choice of $H(s)$, can be demonstrated by applying the Schwartz inequality. The Schwartz inequality is recalled here. Let $u_1(\omega)$ and $u_2(\omega)$ be two complex functions of the real variable ω. Then

$$\left| \int\limits_{-\infty}^{\infty} u_1(\omega) u_2(\omega) \,\mathrm{d}\omega \right|^2 \leqslant \int\limits_{-\infty}^{\infty} |u_1(\omega)|^2 \,\mathrm{d}\omega \int\limits_{-\infty}^{\infty} |u_2(\omega)|^2 \,\mathrm{d}\omega \,. \tag{3.13}$$

In expression (3.13) the equality sign holds if

$$u_1(\omega) = K' u_2^*(\omega) \,,$$

where K' is a constant and * denotes the complex conjugate. If the Schwartz inequality is applied to (3.12) by choosing

$$u_1(\omega) = H(j\omega) \mathcal{N}^{\frac{1}{2}}(\omega) \,, \qquad u_2(\omega) = \frac{S_i(\omega)}{\mathcal{N}^{\frac{1}{2}}(\omega)} \exp[j\omega\tau_M] \,,$$

it can be written

$$\begin{aligned} &\frac{Q_i^2}{2\pi} \frac{\left\{ \int\limits_{-\infty}^{\infty} H(j\omega) S_i(\omega) \exp[j\omega\tau_M] \,\mathrm{d}\omega \right\}}{\int\limits_{-\infty}^{\infty} \mathcal{N}(\omega) |H(j\omega)|^2 \,\mathrm{d}\omega} \leqslant \\ &\leqslant \frac{Q_i^2}{2\pi} \frac{\left\{ \int\limits_{-\infty}^{\infty} \mathcal{N}(\omega) |H(j\omega)|^2 \,\mathrm{d}\omega \right\} \left\{ \int\limits_{-\infty}^{\infty} \frac{|S_i(\omega)|^2}{\mathcal{N}(\omega)} \,\mathrm{d}\omega \right\}}{\int\limits_{-\infty}^{\infty} \mathcal{N}(\omega) |H(j\omega)|^2 \,\mathrm{d}\omega} = \frac{Q_i^2}{2\pi} \int\limits_{-\infty}^{\infty} \frac{|S_i(\omega)|^2}{\mathcal{N}(\omega)} \,\mathrm{d}\omega \,. \end{aligned} \tag{3.13}$$

Equation (3.13) is of general validity and it states that, passing a signal with Fourier transform $S_1(\omega)$ and a noise with spectral power density $\mathcal{N}(\omega)$ through whatever linear network, the output signal-to-noise ratio cannot exceed the integral over the whole frequency axis of the ratio between the energy density of the signal and the power density of the noise.

Out of all the possible $H(j\omega)$'s the only one which makes ϱ reach the limit

$$\frac{Q_1^2}{2\pi}\int_{-\infty}^{\infty}\frac{|S_1(\omega)|^2}{\mathcal{N}(\omega)}\,d\omega \tag{3.14}$$

is the one which satisfies the condition

$$H(j\omega)\mathcal{N}^{\frac{1}{2}}(\omega) = K'\frac{S_1^*(\omega)}{\mathcal{N}^{\frac{1}{2}}(\omega)}\exp[-j\omega\tau_M].$$

The limit itself is, therefore, the sought ϱ_{opt}. The transfer function $H(s)$ of the optimum network must, then, satisfy the relationship

$$H(j\omega) = K'\frac{S_1^*(\omega)}{\mathcal{N}(\omega)}\exp[-j\omega\tau_M]. \tag{3.15}$$

Equation (3.15) can be written by assuming for $S_1(t)$ the signal shape $S_w(t) = 1(t)\cdot\exp[-t/\tau_c]$, eq. (3.5), at the output of the noise-whitening filter. A point at which the noise is white may not even exist in the actual charge-measuring system, but reference to it can be made, though in a virtual way. By putting $S_1(t) = S_w(t)$, $\mathcal{N}(\omega) = W$, eq. (3.15) yields

$$H(j\omega) = \frac{K'}{W}S_w(\omega)\exp[-j\omega\tau_M]. \tag{3.17}$$

Recalling the properties of the conjugate of the Fourier transform of a real function, it can be concluded from (3.17) that, apart from a coefficient, the δ-impulse response of the optimum network following the noise-whitening filter is

$$S_w(\tau_M - t). \tag{3.18}$$

The same result as in the case of the time domain analysis is reached, that is, the optimum processor responds to the δ-impulse at the output of the noise-whitening filter with the mirror image of the signal present at that point.

The optimum signal-to-noise ratio can be evaluated from (3.14) by assuming as $Q_1S_1(t)$ the signal (3.5) at the output of the noise-whitening filter, where $\mathcal{N}(\omega) = W$.

By putting $Q_i = (Q/(C_D + C_i))\sqrt{W/a}$, $S_i(t) = S_w(t)$, (3.14) gives

$$\varrho_{\text{opt}} = \frac{Q}{C_D + C_i}\sqrt{\frac{W}{a}}\left\{\frac{1}{W}\int_{-\infty}^{\infty}|S_w(\omega)|^2\frac{d\omega}{2\pi}\right\}^{\frac{1}{2}} = \tag{3.19}$$

$$= \frac{Q}{C_D + C_i}\sqrt{\frac{W}{a}}\left\{\frac{1}{W}\int_0^{\infty}\exp\left[-2t/\tau_c\right]dt\right\}^{\frac{1}{2}}.$$

The transformation of the integral from the frequency domain to the time domain was made possible by Parseval's theorem.

Evaluation of the integral in (3.19) gives

$$\varrho_{\text{opt}} = \frac{Q}{(C_D + C_i)^{\frac{1}{2}}}\,\frac{1}{(4ab)^{\frac{1}{4}}}, \tag{3.20}$$

which is the same result expressed by (3.9).

The optimum signal-to-noise ratio, according to (3.9) and (3.20), is proportional to the charge available Q and inversely proportional to the square root of the sum of the capacitances C_D and C_i and to the fourth root of the product of series and parallel spectral power densities.

3'4. *Partial use of the information available at the output of the noise-whitening filter.* – The result expressed by eqs. (3.9) and (3.20) refers to the case in which the information available at the output of the noise-whitening filter is fully exploited.

The need of working with a finite peaking time τ_M suggests that only the part of the signal $S_w(t)$ corresponding to $0 \leqslant t \leqslant \tau_M$ is utilized, as in fig. 3.9. The shaded area in fig. 3.9*a*) is the part of the signal utilized for the measurement. The δ-response of the optimum processor following the noise-whitening filter is shown in fig. 3.9*b*), while the response of the whole system to the detector current pulse is shown in fig. 3.9*c*).

The truncated cusp allows the charge measurement to be done at a finite time τ_M; however, no reduction in the width of the output pulse is achieved.

The reduction in signal-to-noise ratio which results from truncation can be obtained from (3.19) by limiting the integral between 0 and τ_M:

$$\varrho_{\tau_M} = \frac{Q}{C_D + C_i}\,\frac{1}{\sqrt{a}}\left[\int_0^{\tau_M}\exp\left[-2t/\tau_c\right]dt\right]^{\frac{1}{2}} = \varrho_{\text{opt}}\left[1 - \exp\left[-2\,\frac{\tau_M}{\tau_c}\right]\right]^{\frac{1}{2}}. \tag{3.21}$$

As pointed out by (3.21), the increase in ϱ_{τ_M} which results from extending the measurement time beyond τ_c is very small. Increasing, for instance, τ_M from τ_c to infinite, only 8% is gained in signal-to-noise ratio.

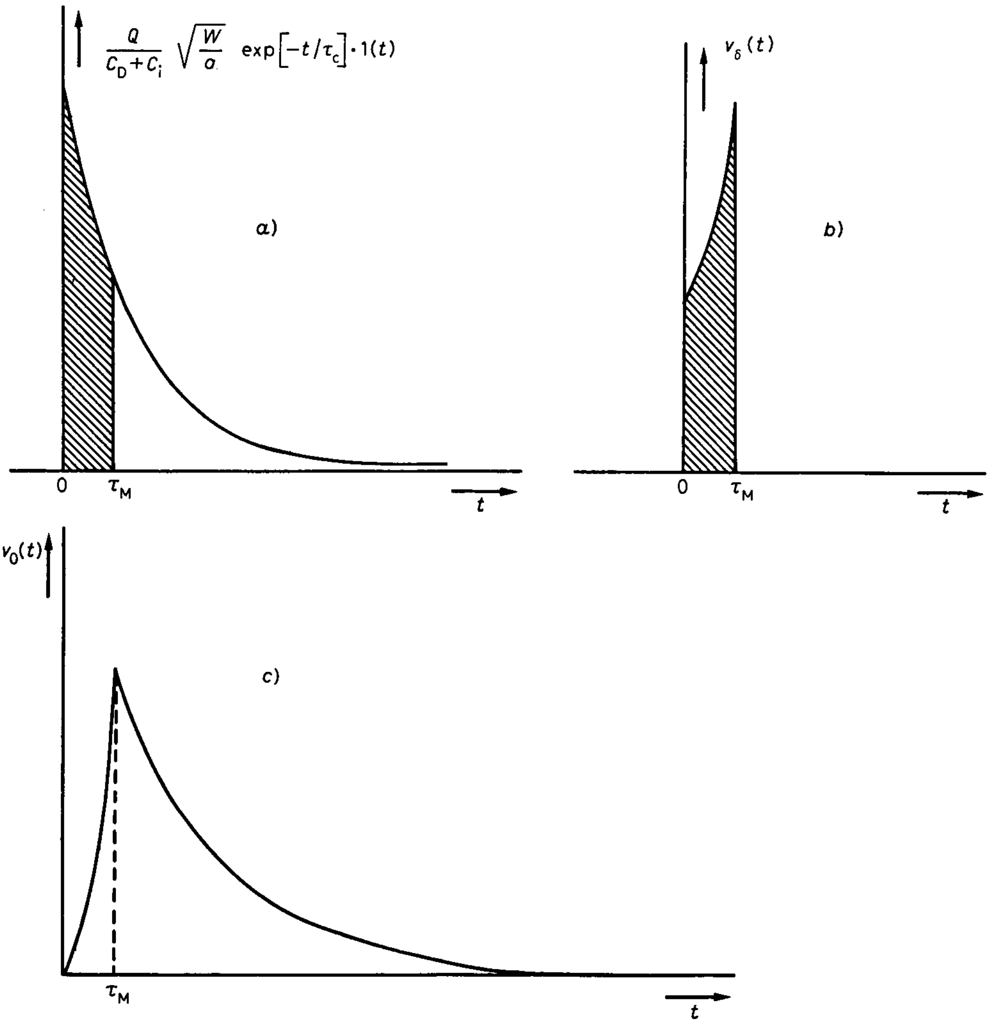

Fig. 3.9. – Use of a fraction of information contained in the signal: *a*) the shaded area is the part utilized in the measurement, *b*) δ-impulse response of the optimum network, *c*) truncated cusp.

3'5. *Matched-filter theory in the case of finite rate of arrival of events on the detector.* – The matched-filter theory developed so far has not been subjected to any constraint in the pulse width. The signal at the output of the matched filter has either an indefinitely long peaking time if ϱ_{opt} must be achieved or a finite peaking time in the case of a truncated cusp. Both signals have infinite duration. The theory, in other words, was restricted to the consideration of a single event to be measured and according to this hypothesis the measurement of the peak amplitude of the cusp, which carries the information about Q, was referred to an indefinitely accurate baseline.

In the actual case a sequence of pulse amplitudes has to be measured and, therefore, a constraint on the maximum allowed duration of the pulse at the processor output must be added. The problem of the optimum least-square error measurement will, therefore, be restated by assuming that elementary events delivering in the detector the charge Q occur in a random sequence of finite rate.

The situation is depicted in fig. 3.10.

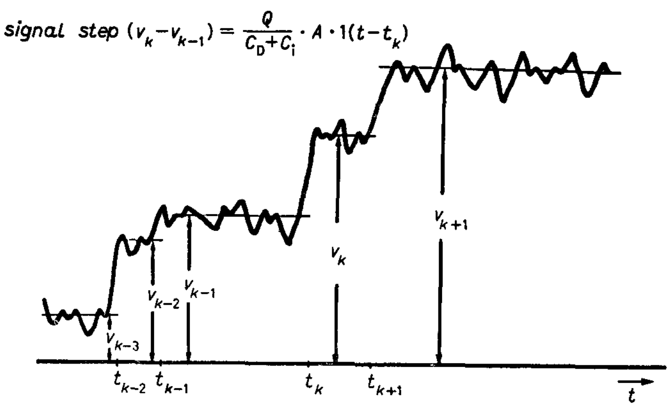

Fig. 3.10. – Stochastic straircase determined at the preamplifier output by the random occurrence of detector pulses.

The stochastic staircase of fig. 3.10 represents the effect of the random superposition of steps determined by the occurrence of the detector current pulses. The evaluation of the charge associated with the event happening at $t = t_k$, for instance, requires the best estimate of the difference $v_k - v_{k-1}$. The level v_{k-1} existing prior to the arrival of the event at $t = t_k$ represents, therefore, the baseline to which the event to be measured is referred. To deal with the present problem a simplifying hypothesis, which is frequently respected in the experimental situations of elementary-particle physics, will be introduced. The hypothesis is related with the property that, when the measurement time is short compared with the noise corner time constant τ_c given by (3.4), the parallel noise becomes of minor importance. A treatment of the present problem without this limiting hypothesis is available in the literature [12]. If only the series noise is considered, the spectral noise density at the preamplifier output is white and, therefore, no additional whitening filter is needed.

This means that the problem of the best estimate of the $v_k - v_{k-1}$ difference has to be solved in the presence of white noise, whose spectral density, according to fig. 3.1, is, at the preamplifier output, $W = aA^2$. As shown in fig. 3.10, a time interval (t_{k-1}, t_k) is available to estimate v_{k-1} and a time interval (t_k, t_{k+1}) is available to estimate v_k. Application of the previously developed matched-filter theory to the measurement of the v_{k-1} level in the presence of white noise shows that the best processing is a pure integration in the (t_{k-1}, t_k) interval. The optimum signal-to-noise ratio is, according to (3.14),

$$\varrho_{\text{opt}} = \frac{v_{k-1}}{a^{\frac{1}{2}} A} \left[\int\limits_{t_{k-1}}^{t_k} \mathrm{d}t \right]^{\frac{1}{2}} = \frac{v_{k-1}}{a^{\frac{1}{2}} A} [t_k - t_{k-1}]^{\frac{1}{2}} . \tag{3.22}$$

According to (3.22) the root-mean-square noise at the output of the optimum processor is

$$\langle v^2_{\text{N},k} \rangle^{\frac{1}{2}} = A \left[\frac{a}{t_k - t_{k-1}} \right]^{\frac{1}{2}} . \tag{3.23}$$

Similarly, the optimum processor to estimate v_k in the presence of white noise is a pure integrator acting in the (t_k, t_{k+1}) interval. It follows again from (3.14)

$$\varrho_{\text{opt}} = \frac{v_k}{a^{\frac{1}{2}} A} \left[\int\limits_{t_k}^{t_{k+1}} \mathrm{d}t \right]^{\frac{1}{2}} = \frac{v_k}{a^{\frac{1}{2}} A} [t_{k+1} - t_k]^{\frac{1}{2}} \tag{3.24}$$

and for the noise at the output of the optimum processor

$$\langle v^2_{\text{N},k+1} \rangle^{\frac{1}{2}} = A \left[\frac{a}{t_{k+1} - t_k} \right]^{\frac{1}{2}} . \tag{3.25}$$

The signal-to-noise ratio in the measurement of the step amplitude can now be evaluated as

$$\varrho_{\text{opt}}(v_k - v_{k-1}) = \frac{v_k - v_{k-1}}{[\langle v^2_{\text{N},k} \rangle + \langle v^2_{\text{N},k+1} \rangle]^{\frac{1}{2}}} = \frac{Q}{(C_{\text{D}} + C_{\text{i}})[1/(t_{k+1} - t_k) + 1/(t_k - t_{k-1})]^{\frac{1}{2}} a^{\frac{1}{2}}} . \tag{3.26}$$

It is important to point out that the optimum signal-to-noise ratio in the measurement of the difference depends on the length of the empty intervals available for the measurement *before* and *after* the event to be processed. The network which implements the best processing for the $v_k - v_{k-1}$ measurement is characterized by a constant distribution of weights of negative polarity between t_{k-1} and t_k and by a constant distribution of weights of positive polarity between t_k and t_{k+1}. Both distributions are shown in fig. 3.11 normalized to unit area.

Figures 3.11*b*) and *d*) show, respectively, the δ-response of the optimum processor and the actual output signal, convolution of the wave form *b*) and of the step under measurement.

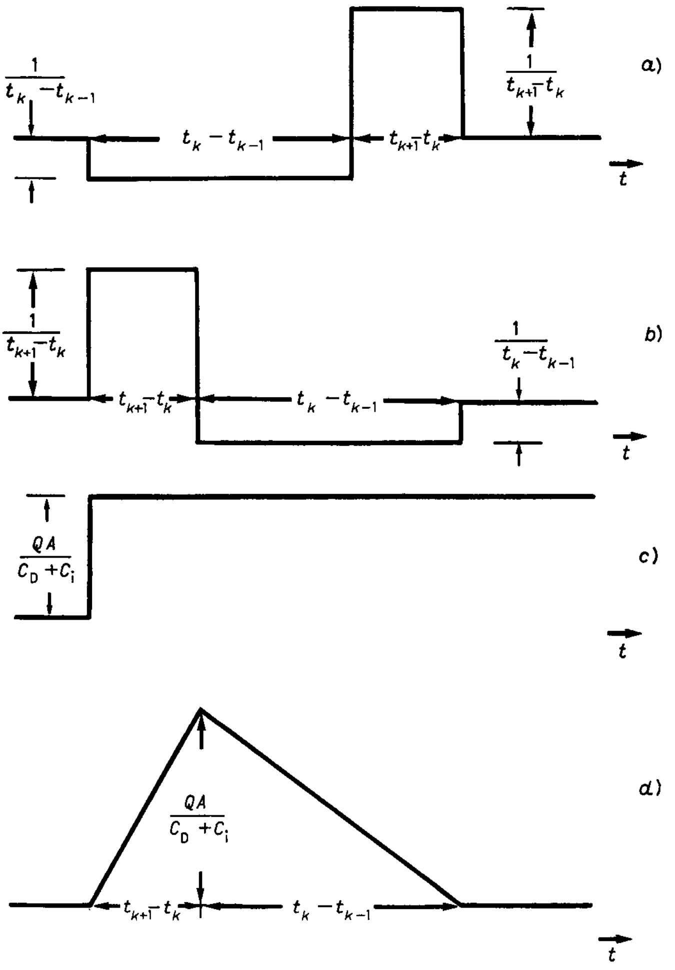

Fig. 3.11. – Optimum processing for the estimation of a voltage step in the presence of white noise: *a*) weight distribution, *b*) δ-response of the optimum processor, *c*) step under measurement, *d*) actual response of the optimum processor to the input step.

As the detector pulses are randomly distributed in time and their instants of arrival unpredictable, the best processing based upon the exploitation of the full empty intervals before and after each event is not of practical feasibility. A good approximation consists of using equal time intervals τ preceding and following the event [12]. The total processing time 2τ must be chosen for a given event rate short enough to keep the pile-up probability small.

In the case in which processing intervals of equal duration are employed, (3.26) simplifies into

$$\varrho(v_k - v_{k-1}) = \frac{Q}{(C_D + C_i)[2a/\tau]^{\frac{1}{2}}} \cdot \tag{3.27}$$

It is interesting now to compare the optimum processing described in fig. 3.11 with the one which would suggest Baldinger and Franzen's theory in the case of white noise and with the exploitation of a finite step duration τ_M.

The corresponding wave forms are shown in fig. 3.12.

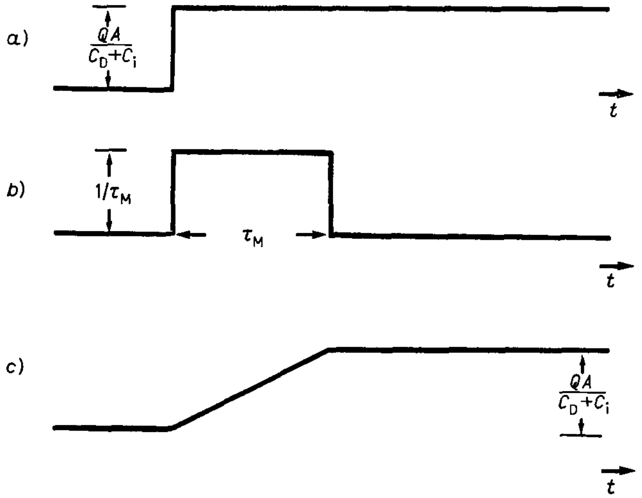

Fig. 3.12. – Optimum processing of a step in white noise and finite measurement time τ_M according to the theory of Baldinger and Franzen: *a*) step under measurement, *b*) δ-response of the optimum processor, *c*) actual response of the optimum processor to the input step.

The processor of fig. 3.12 can be considered as a particular case of the one of fig. 3.11, in which the time interval $t_k - t_{k-1}$ has become indefinitely long, that is, when the free time available for baseline estimation before t_k is infinite. A time-invariant implementation of a processor measuring the amplitude of the input step with a finite resolving time 2τ is the circuit which responds to the δ-impulse excitation with the bipolar signal of fig. 3.13.

The bipolar weighting distribution implemented by the processor of fig. 3.13 has been recognized to be the optimum one when a free time τ is available before and after the edge of the incoming pulse [12].

The time-variant realization of the processing described in fig. 3.13 is shown in fig. 3.14 I).

The timing relationships are shown in fig. 3.14 II).

As shown in fig. 3.14 II), the δ-impulse carrying the charge information arrives at one of the multiplier inputs when the triangular wave form at the other multiplier input has its maximum amplitude. The gated integrator performs the operation

$$\frac{Q}{C_D + C_i} A \int_0^{2\tau} \delta(t - \tau) r(t)\, dt = \frac{Q}{C_D + C_i} A r(\tau) = \frac{Q}{C_D + C_i} A , \tag{3.28}$$

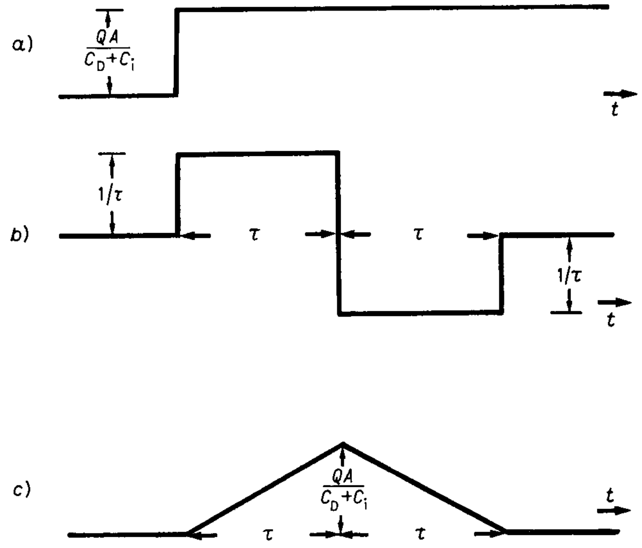

Fig. 3.13. – Processing the input step under the condition of finite resolving time 2τ: *a*) input step, *b*) δ-impulse response of the processor, *c*) actual response of the processor to the input step.

having assumed as time origin the arrival instant of the radiation on the detector.

The white noise at the input of the preamplifier, which, as will be discussed exhaustively in the next section, can be represented in the time domain as a random sequence of positive and negative δ-impulses, becomes after differentiation a random sequence of doublets. A doublet arriving at the multiplier input at a random instant t_0, with $0 < t_0 < 2\tau$, produces at the integrator output

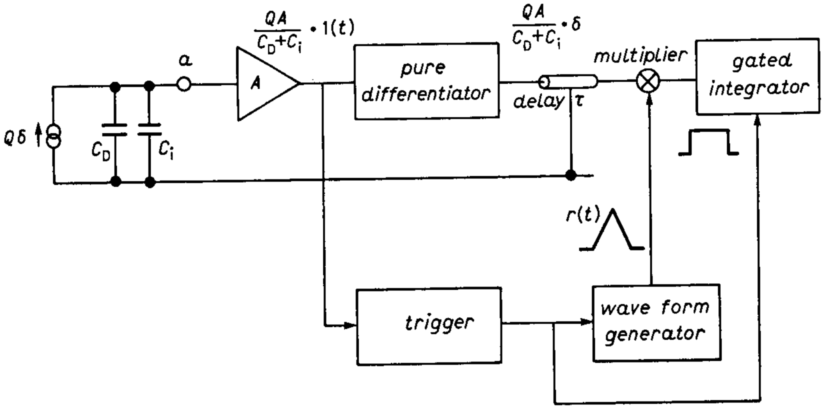

Fig. 3.14I) – Time-variant realization of the processor with bipolar weight distribution. Block diagram of the processor.

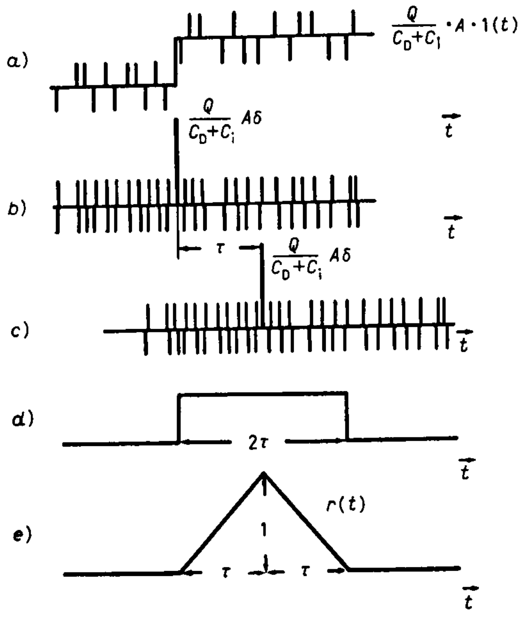

Fig. 3.14II). – Time-variant realization of the processor with bipolar weight distribution. Wave forms in the various points: *a*) step at the preamplifier output with δ-noise, *b*) δ-impulse at the differentiator output with doublet noise, *c*) same as *b*) after a delay τ, *d*) integrator gating command, *e*) triangular multiplying wave form.

a step with an amplitude

$$\int_0^{2\tau} \delta'(t-t_0)r(t)\,\mathrm{d}t = r'(t_0)\,. \tag{3.29}$$

If now t_0 is varied between 0 and 2τ, $r'(t_0)$ describes the bipolar function of fig. 3.13*b*).

It is, therefore, possible to conclude that the time-variant processor of fig. 3.14 I) has the same signal-to-noise ratio as the time-invariant one with bipolar δ-response of fig. 3.13. Such a conclusion relies upon the fact that both produce the same output amplitude when the charge Q is delivered by the detector and they are characterized by the same weighting function, coinciding with the δ-response in the time-invariant case or $r'(t)$ in the time-variant one. Note that the output responses for the signal are different for the equivalent time-variant and time-invariant processors, while the resolving times are equal.

3'6. *Optimum filter for an arbitrary pulse shape in white noise for a fixed estimation time of the baseline.* – The problem of synthesizing the optimum filter for an arbitrary input pulse shape in white noise and fixed baseline estimation time can be introduced. The case considered here refers, as in Baldinger and Franzen's approach, to a signal consisting of two narrow rectangles of amplitudes $\mathscr{A}_1$ and $\alpha\mathscr{A}_1$ in band-limited white noise (fig. 3.15*a*)).

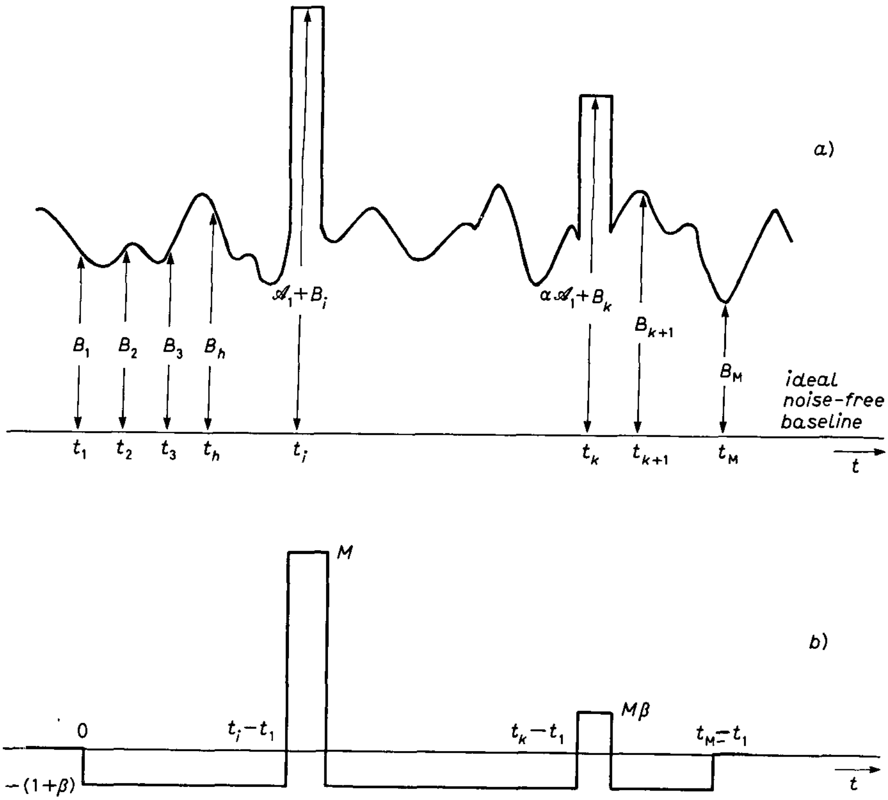

Fig. 3.15. – *a*) Signal consisting of two pulses in white noise, with fixed baseline estimation time. *b*) Weighting function of the optimum processor.

The baseline is sampled at M equally spaced instants $t_1, t_2, t_3, \ldots, t_M$. As the noise is supposed to be band-limited white, the noise samples taken at these instants are uncorrelated. Let $B_1, B_2, B_3, \ldots, B_M$ be the baseline samples referred to an ideal, noise-free baseline. Let t_i, t_k be the instants at which the two pulses occur and suppose these instants different from those at which the baseline is sampled. It will be assumed that M is much larger than the number of wave form samplings, two in this case.

The following weighted sum can be constructed, by referring the $\mathscr{A}_1+B_i$, $\alpha\mathscr{A}_1+B_k$ amplitudes to all the possible baseline evaluations:

$$\sum_{j=1}^{M}[(\mathscr{A}_1+B_i)-B_j]+\beta\sum_{j=1}^{M}[(\alpha\mathscr{A}_1+B_k)-B_j]\,. \tag{3.30}$$

Equation (3.30) gives for the square amplitude of the signal

$$\mathcal{S}^2 = M^2(1+\alpha\beta)^2\mathcal{A}_1^2 . \tag{3.31}$$

By labelling $v_{\mathrm{N},i}$ the noise amplitude at the instant t_i, from (3.30) the following expression can be written for the total noise $v_{\mathrm{N,T}}$:

$$v_{\mathrm{N,T}} = Mv_i - \sum_{j=1}^{M} v_j + \beta M v_k - \beta\sum_{j=1}^{M} v_j . \tag{3.32}$$

The root-mean-square noise can be evaluated from (3.32) as

$$\langle v_{\mathrm{N,T}}^2\rangle \simeq (\beta^2+1)(M^2+M)\langle v_{\mathrm{N}}^2\rangle , \tag{3.33}$$

where $\langle v_{\mathrm{N}}^2\rangle$ is the ensemble average of the noise at the sampling instants.

The square of the signal-to-noise ratio, from (3.31) and (3.33), can be written as

$$\varrho^2 = \frac{\mathcal{A}_1^2(1+\alpha\beta)^2}{\langle v_{\mathrm{N}}^2\rangle[(1+\beta^2)(1+1/M)]} \tag{3.34}$$

and it achieves a maximum for

$$\beta = \alpha . \tag{3 35}$$

The weighting function of the optimum processor is shown in fig. 3.15*b*).

The above outlined procedure can be extended to any input wave form.

REFERENCES

[1] H. Rothe and W. Dahlke: *Proc. IRE*, **44**, 811 (1956).
[2] 50 I.R.E., 20 S1 Committee, H. A. Haus, Chairman: *Proc. IRE*, **48**, 60 (1960).
[3] I.R.E. Subcommittee 7.9 on Noise, H. A. Haus, Chairman: *Proc. IRE*, **48**, 69 (1960).
[4] A. Van Der Ziel: *Noise-Sources, Characterization, Measurements* (Prentice-Hall, Inc., Englewood Cliffs, N. J., 1970).
[5] V. Radeka: *Nucl. Instrum. Methods Phys. Res.*, **226**, 209 (1984).
[6] E. Gatti and V. Svelto: *Energ. Nucl.* (*Milan*), **8**, 505 (1961).
[7] E. Baldinger and W. Franzen: *Adv. Electron. Electron Phys.*, **8**, 225 (1956).
[8] V. Radeka and N. Karlovac: *Nucl. Instrum. Methods*, **52**, 86 (1967).
[9] F. T. Arecchi, G. Cavalleri, E. Gatti and V. Svelto: *Energ. Nucl.* (*Milan*), **7**, 691 (1960).
[10] G. L. Turin: *IRE Trans. Inf. Theory*, IT-**6**, 311 (1960).
[11] A. Papoulis: *Probability, Random Variables and Stochastic Processes* (McGraw-Hill, New York, N. Y., 1965).
[12] M. Bertolaccini, C. Bussolati, S. Cova, J. De Lotto and E. Gatti: *Nucl. Instrum. Methods*, **61**, 84 (1968).

4. – Calculation of the signal-to-noise ratio for some practical analog processors.

4'1. *Introductive remarks.* – The analysis of the previous section is of fundamental nature, its purpose being that of clarifying the intrinsic limitations that occur in the measurement of the charge delivered by a capacitive source. The optimum processing realized by the indefinite-cusp response, the loss in signal-to-noise ratio introduced by the truncated cusp and the constraint set by finite empty intervals before and after the event to be processed have been reviewed.

In practical applications of nuclear radiation detectors, however, networks that respond to a δ-impulse shaped detector current with signals different from the cusp or the triangle are sometimes employed.

Additional constraints may in fact be present, requiring, for instance, a rounded top in the δ-response of the whole system to make the measurement of the peak amplitude more precise or a flat-topped trapezoidal response to reduce the ballistic errors [1, 2]. Cancellation of long tails following the signal may require bipolar shaping [3].

For these reasons it is useful to introduce analytical methods to evaluate the signal-to-noise ratio. The problem to be solved will be presented in the following way. In a given charge-measuring system, consisting of detector, preamplifier and of the network which determines the signal-to-noise ratio, the noise sources are specified through their power spectra, like in fig. 4.1. The signal-to-noise ratio has to be evaluated. The network determining the signal-to-noise ratio can be of either time-invariant or time-variant nature. In the former case the signal-to-noise ratio can be evaluated using a frequency domain approach or a time domain approach.

In the case of a network of time-variant nature, the time domain method has necessarily to be adopted.

In the nuclear-electronics literature the network which determines the signal-to-noise ratio is either referred to as a filter to emphasize its action in the frequency domain or as a shaper to emphasize its behaviour in the time domain.

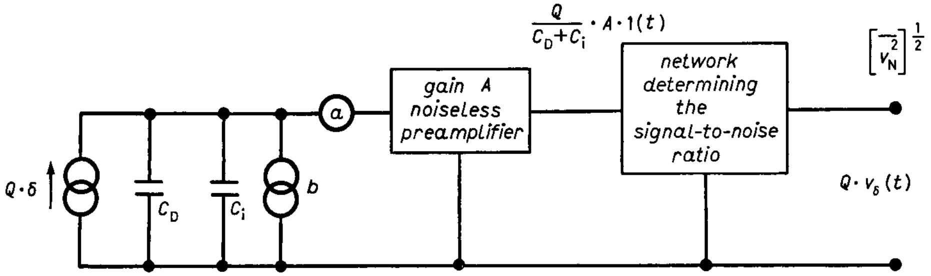

Fig. 4.1. – Evaluation of the signal-to-noise ratio in a charge-measuring system.

In the foregoing treatment the term shaper will be generally preferred, both because more importance will be attributed to the time domain analysis and because the term shaper seems to be more appropriate when referred to time-variant systems.

4'2. *Time-invariant shapers.* – When the network determining the signal-to-noise ratio in fig. 4.1 is of time-invariant nature, its behaviour is described by the transfer function $T(s)$. The transfer function $T(s)$ is the Laplace transform of the response of the shaper to an input signal v_1 assumed equal to a δ-impulse. By definition of time-invariant shaper, such a response at a given instant t is a function of the difference $t - t_1$ alone, t_1 being the instant at which the input δ-impulse is applied and is independent of the absolute time position of t_1.

4'2.1. Frequency domain noise calculation. Returning to the processor of fig. 4.1 and calling $v_\delta(t)$ the response to a detector current signal represented by a δ-impulse of unit coefficient, $v_\delta(t)$ can be written as

$$v_\delta(t) = \mathcal{L}^{-1}\left[\frac{1}{s(C_D + C_i)}\,AT(s)\right], \tag{4.1}$$

where $\mathcal{L}^{-1}$ denotes the inverse Laplace-transform operator. As $v_\delta(t)$ is zero for $t < 0$ and must return to zero at either a finite time or as $t \to \infty$, it must have at least one maximum or minimum depending on its polarity. Let MAX $[v_\delta(t)]$ be the largest absolute value of these maxima and minima. It will be assumed that the signal measurement is performed on this value. The signal amplitude corresponding to the release of a charge Q in the detector will be, therefore,

$$Q\cdot\mathrm{MAX}\,[v_\delta(t)]\,.$$

The output root-mean-square noise $[\overline{v_N^2}]^{\frac12}$ can be evaluated according to the frequency domain approach as [4-8]

$$[\overline{v_N^2}]^{\frac12} = \left[\int_{-\infty}^{\infty}\mathcal{N}(\omega)|T(j\omega)|^2\,\mathrm{d}f\right]^{\frac12} = \left[\frac{1}{2\pi}A^2\int_{-\infty}^{\infty}\left(a + \frac{b}{\omega^2(C_D + C_i)^2}\right)|T(j\omega)|^2\,\mathrm{d}\omega\right]^{\frac12}. \tag{4.2}$$

The signal-to-noise ratio ϱ can, therefore, be expressed as

$$\varrho = \frac{\dfrac{QA}{C_D + C_i}\,\mathrm{MAX}\,\mathcal{L}^{-1}\left[\dfrac{T(s)}{s}\right]}{\left\{\dfrac{1}{2\pi}A^2\displaystyle\int_{-\infty}^{\infty}\left(a + \frac{b}{\omega^2(C_D + C_i)^2}\right)|T(j\omega)|^2\,\mathrm{d}\omega\right\}^{\frac12}}\,. \tag{4.3}$$

The signal-to-noise ratio, as expressed by (4.3), does not provide a description of the intrinsic noise behaviour of the processor, for it depends on a parameter, Q, related to the incoming radiation.

The noise performances of a processor intended for capacitive sources are usually expressed in terms of equivalent noise charge referred to the input, ENC [7]. The equivalent noise charge is defined, according to (4.3), as that value of Q which makes $\varrho = 1$. This means that the equivalent noise charge is the value of charge which injected across the detector capacitance by a δ-like signal produces at the output of the analog processor a signal whose amplitude equals the output root-mean-square noise. By applying the definition, eq. (4.3) yields

$$(4.4) \qquad \mathrm{ENC} = \frac{\left\{\dfrac{1}{2\pi}\displaystyle\int_{-\infty}^{\infty}\left(a(C_\mathrm{D}+C_\mathrm{i})^2+\dfrac{b}{\omega^2}\right)|T(j\omega)|^2\,\mathrm{d}\omega\right\}^{\frac{1}{2}}}{\mathrm{MAX}\,\mathscr{L}^{-1}\left[\dfrac{T(s)}{s}\right]}\ \text{r.m.s. coulomb}\,.$$

As stated by (4.3), the evaluation of ϱ requires the evaluation of the peak amplitude of the δ-response of the whole system and that of the noise integral at the denominator.

A few examples will illustrate the method.

4·2.1.1. Triangular shaping. In the case shown in fig. 4.2, $T(s)$ has the following expression:

$$T(s) = \frac{1}{s\tau_\mathrm{M}}\left(1-\exp\left[-s\tau_\mathrm{M}\right]\right)^2 .$$

The numerator of (4.3) is equal to $Q(A/(C_\mathrm{D}+C_\mathrm{i}))$.

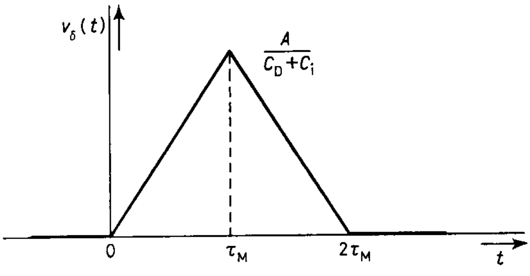

Fig. 4.2. – Triangular shaping with peaking time τ_M.

The integral at the denominator is given by

$$(4.5)\qquad 16\int_{-\infty}^{\infty}\left[a+\frac{b}{\omega^2(C_D+C_i)^2}\right]\frac{\sin^4(\omega\tau_M/2)}{\omega^2\tau_M^2}\,d\omega=$$

$$=16\frac{a}{\tau_M}\int_0^{\infty}\frac{\sin^4 x}{x^2}\,dx+\frac{4b}{(C_D+C_i)^2}\tau_M\int_0^{\infty}\frac{\sin^4 x}{x^4}\,dx\qquad\left(x=\frac{\omega\tau_M}{2}\right).$$

If the values of the two integrals (see appendix) are introduced into (4.5), the following expression is found for the denominator of (4.3):

$$(4.6)\qquad A\left[2\frac{a}{\tau_M}+\frac{2}{3}\frac{b}{(C_D+C_i)^2}\tau_M\right]^{\frac{1}{2}}.$$

The signal-to-noise ratio can now be evaluated from (4.3), thus obtaining

$$(4.7)\qquad \varrho=\frac{Q}{[2(a/\tau_M)(C_D+C_i)^2+(2/3)b\tau_M]^{\frac{1}{2}}}$$

and the equivalent noise charge is

$$(4.8)\qquad \mathrm{ENC}=\left[2\frac{a}{\tau_M}(C_D+C_i)^2+\frac{2}{3}b\tau_M\right]^{\frac{1}{2}}\ \text{r.m.s. coulomb}.$$

4.2.1.2. *RC-CR* shaping. A transfer function of the network determining the signal-to-noise ratio of the type

$$T(s)=\frac{s\tau_M}{(1+s\tau_M)^2}$$

leads to the following $v_\delta(t)$:

$$v_\delta(t)=\frac{A}{C_D+C_i}\frac{t}{\tau_M}\exp[-t/\tau_M].$$

The time dependence of $v_\delta(t)$ is shown in fig. 4.3. The peak of $v_\delta(t)$ occurs at $t=\tau_M$ and the peak value is $(A/(C_D+C_i))\cdot 1/e$.

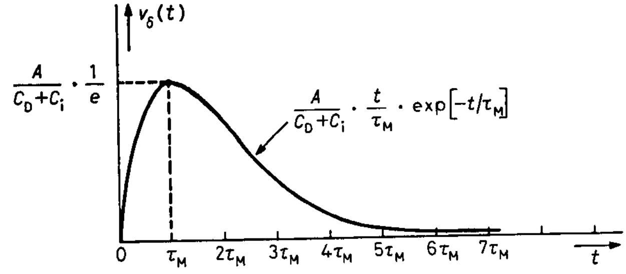

Fig. 4.3. – Response of the *RC-CR* filter to a δ-impulse detector current.

The integral at the denominator of (4.3) can be written as

$$2a\int_0^\infty \frac{\omega^2\tau_M^2}{(1+\omega^2\tau_M^2)^2}\,\mathrm{d}\omega+\frac{2b\tau_M^2}{(C_D+C_i)^2}\int_0^\infty\frac{\mathrm{d}\omega}{(1+\omega^2\tau_M^2)^2}=$$

$$=\frac{2a}{\tau_M}\int_0^\infty\frac{x^2\,\mathrm{d}x}{(1+x^2)^2}+\frac{2b}{(C_D+C_i)^2}\tau_M\int_0^\infty\frac{\mathrm{d}x}{(1+x^2)^2}\qquad(x=\omega\tau_M)\,.$$

The value of both integrals is $\pi/4$ (see appendix).

The signal-to-noise ratio for the *RC-CR* shaping is, therefore,

$$\varrho=\frac{(2/e)Q}{[(C_D+C_i)^2(a/\tau_M)+b\tau_M]^{\frac{1}{2}}}\tag{4.9}$$

and the equivalent noise charge is

$$\mathrm{ENC}=\frac{e}{2}\left[(C_D+C_i)^2\frac{a}{\tau_M}+b\tau_M\right]^{\frac{1}{2}}\text{r.m.s. coulomb}\,.\tag{4.10}$$

4.2.2. Time domain noise calculation. The time domain noise calculation will now be introduced.

The time domain approach is particularly straightforward in the case of a time-invariant processor of the type shown in fig. 4.1, and for the noise generators there considered. The time domain approach is based upon two theorems. One, known as Carson's theorem, states that an ergodic noise source with bilateral power spectrum $\mathcal{N}(\omega)$ can be considered as due to the superposition in the time domain of randomly distributed events with Fourier transform $\Phi(\omega)$ occurring at an average rate λ [9, 10]. The relationship between $\mathcal{N}(\omega)$, $\Phi(\omega)$ and λ is

$$\mathcal{N}(\omega)=\lambda|\Phi(\omega)|^2\,.\tag{4.11}$$

So, for instance, white noise with bilateral spectrum d can be thought of as the result of random occurrence of δ-impulses of unit area with an average rate $\lambda=d$. If the noise has a zero mean value, the δ-impulses will be randomly positive and negative.

In the circuit of fig. 4.1 both series and parallel noise wave forms can be considered, therefore, resulting from the random occurrence of δ-impulses with average rates a and b, respectively.

Once the noise generators are represented in this way, the output noise can be evaluated by making use of Campbell's theorem [9, 11]. This theorem states that a noise process resulting from the superposition of pulses of a fixed shape $\varphi(t)$, randomly occurring in time with an average rate λ, has a root-mean-square value $(\overline{v_N^2})^{\frac{1}{2}}$ given by

$$[\overline{v_N^2}]^{\frac{1}{2}} = \left[\lambda\int\limits_{-\infty}^{\infty}\varphi^2(t)\,\mathrm{d}t\right]^{\frac{1}{2}}. \tag{4.12}$$

The evaluation of the signal-to-noise ratio on the basis of the time domain approach proceeds in the following way [12-14].

The signal amplitude is calculated, like in the previous case, as

$$Q\cdot\mathrm{MAX}[v_\delta(t)] = \frac{Q}{C_D + C_I}\,A\cdot\mathrm{MAX}\,\mathscr{L}^{-1}\left[\frac{T(s)}{s}\right].$$

For the noise evaluation, it can be observed that a δ in the parallel generator induces at the output the response $v_\delta(t)$. According to Campbell's theorem, the root-mean-square output contribution due to the parallel noise source is

$$\left[b\int\limits_{-\infty}^{\infty}v_\delta^2(t)\,\mathrm{d}t\right]^{\frac{1}{2}}. \tag{4.13}$$

The contribution due to the series noise has to be calculated as follows. A δ-impulse in the series generator induces at the output a signal whose Laplace transform is

$$A\,T(s) = s(C_D + C_I)\mathscr{L}[v_\delta(t)]. \tag{4.14}$$

Equation (4.14) states that a δ-impulse in the series generator excites at the output the response

$$(C_D + C_I)v'_\delta(t),$$

proportional to the time derivative of $v_\delta(t)$.

Utilizing Campbell's theorem, it can be concluded that the series generator contributes to the output root-mean-square noise with the term

$$\left[a(C_D + C_I)^2\int\limits_{-\infty}^{\infty}[v'_\delta(t)]^2\,\mathrm{d}t\right]^{\frac{1}{2}}. \tag{4.15}$$

Both expressions (4.13) and (4.15) can be written in a more useful fashion remembering that

$$v_\delta(t) = \frac{A}{C_D + C_I}\,\mathscr{L}^{-1}\left[\frac{T(s)}{s}\right].$$

By putting $f(t) = \mathscr{L}^{-1}[T(s)/s]$ the previous relationship can be written as

$$v_\delta(t) = \frac{A}{C_D + C_i} f(t)\,.$$

Let now $u = t/\tau_R$ be a dimensionless variable, which represents the time normalized to a reference interval τ_R. For instance, τ_R might be the peaking time of $v_\delta(t)$. Observing that $dt = \tau_R du$, $dv_\delta/dt = (dv_\delta/du)\cdot 1/\tau_R$ and that $v_\delta(u) = (A/(C_D + C_i))f(u)$, the total root-mean-square noise resulting from (4.13) and (4.15) can be written as

$$\text{(4.16)}\qquad [\overline{v_N^2}]^{\frac{1}{2}} = A\left[\frac{a}{\tau_R}\int_{-\infty}^{\infty}[f'(u)]^2 du + \frac{b\tau_R}{(C_D + C_i)^2}\int_{-\infty}^{\infty}[f(u)]^2 du\right]^{\frac{1}{2}}.$$

The two integrals in (4.16) are two numerical shape coefficients that can be easily calculated from the knowledge of $v_\delta(t)$. To clarify the time domain method, some examples will be discussed.

4.2.2.1. Triangular shaping. From fig. 4.2 the following expression of $v_\delta(t)$ can be obtained, with $\tau_R = \tau_M$: $v_\delta(u) = (A/(C_D + C_i))[1(u)\cdot u - 2(u-1)\cdot 1(u-1) + (u-2)\cdot 1(u-2)]$.

The integrals in eq. (4.16) have the following values:

$$\int_{-\infty}^{\infty} f^2(u)\,du = \frac{2}{3}\,, \qquad \int_{-\infty}^{\infty}[f'(u)]^2 du = 2\,.$$

The output root-mean-square noise is, therefore,

$$\text{(4.17)}\qquad [\overline{v_N^2}]^{\frac{1}{2}} = A\left[2\frac{a}{\tau_M} + \frac{2}{3}\tau_M\frac{1}{(C_D + C_i)^2}\right]^{\frac{1}{2}}.$$

The signal-to-noise ratio is

$$\text{(4.18)}\qquad \varrho = \frac{Q}{[2(a/\tau_M)(C_D + C_i)^2 + (2/3)\tau_M]^{\frac{1}{2}}}$$

and the equivalent noise charge is

$$\text{(4.19)}\qquad \text{ENC} = \left[2\frac{a}{\tau_M}(C_D + C_i)^2 + \frac{2}{3}\tau_M\right]^{\frac{1}{2}} \text{r.m.s. coulomb}\,.$$

as already found, (4.8).

4·2.2.2. *RC-CR* shaping. According to fig. 4.3, putting $\tau_R = \tau_M$, $v_\delta(u)$ becomes $(A/(C_D + C_i))u \exp[-u]\cdot 1(u)$. The two integrals in eq. (4.16) become

$$\int_{-\infty}^{\infty} f^2(u)\,\mathrm{d}u = \int_0^{\infty} u^2 \exp[-2u]\,\mathrm{d}u = \frac{1}{4},$$

$$\int_{-\infty}^{\infty} [f'(u)]^2\,\mathrm{d}u = \int_0^{\infty} (1-u)^2 \exp[-2u]\,\mathrm{d}u = \frac{1}{4}.$$

The root-mean-square noise becomes, therefore,

$$[\overline{v_N^2}]^{\frac{1}{2}} = \frac{A}{2}\left[\frac{a}{\tau_M} + \frac{b}{(C_D + C_i)^2}\tau_M\right]^{\frac{1}{2}}. \tag{4.20}$$

The signal-to-noise ratio and the equivalent noise charge are given, respectively, by

$$\varrho = \frac{(2/e)Q}{[(C_D + C_i)^2(a/\tau_M) + b\tau_M]^{\frac{1}{2}}}, \tag{4.21}$$

$$\mathrm{ENC} = \frac{e}{2}\left[(C_D + C_i)^2\frac{a}{\tau_M} + b\tau_M\right]^{\frac{1}{2}} \text{r.m.s. coulomb}. \tag{4.22}$$

as already found, (4.10).

4·2.2.3. Piecewise parabolic shaping. A piecewise parabolic δ-response can be obtained by multiplying the normalized function shown in fig. 4.4 by $A/(C_D + C_i)$. The way in which the piecewise parabolic shape is constructed from its second derivative is shown in the same figure. The signal amplitude is $(Q/(C_D + C_i))A$. The root-mean-square output noise is, according to eq. (4.16),

$$[\overline{v_N^2}]^{\frac{1}{2}} = A\left[a\frac{1}{\tau_M}\int_{-\infty}^{\infty}[f'(u)]^2\,\mathrm{d}u + \frac{b\tau_M}{(C_D + C_i)^2}\int_{-\infty}^{\infty} f^2(u)\,\mathrm{d}u\right]^{\frac{1}{2}}.$$

The values of the two integrals are 8/3 and 14/15, respectively. The signal-to-noise ratio is

$$\varrho = \frac{Q}{[a(C_D + C_i)^2(8/3)(1/\tau_M) + b(14/15)\tau_M]^{\frac{1}{2}}} \tag{4.23}$$

and the equivalent noise charge is

$$\mathrm{ENC} = \left[a(C_D + C_i)^2\frac{8}{3}\frac{1}{\tau_M} + b\frac{14}{15}\tau_M\right]^{\frac{1}{2}} \quad \text{r.m.s. coulomb}. \tag{4.24}$$

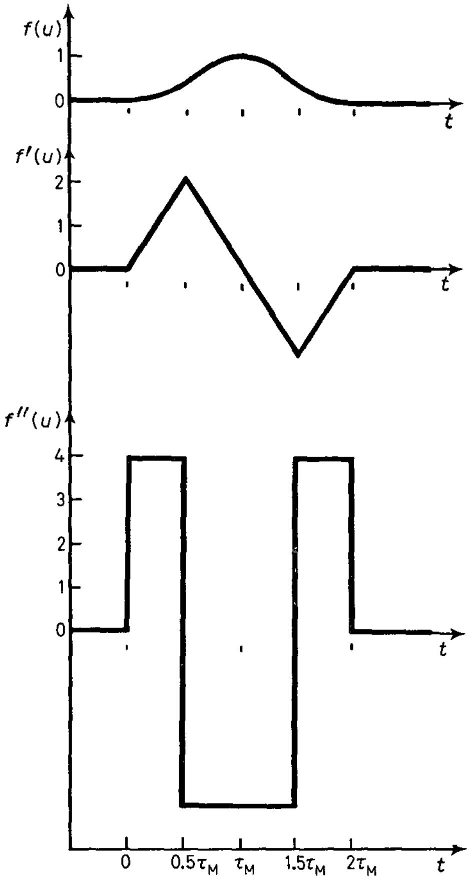

Fig. 4.4. – Normalized piecewise parabolic pulse and its first and second derivative, $u = t/\tau_M$.

4'2.2.4. Trapezoidal shaping. The trapezoidal response to a δ-impulse detector current is shown in fig. 4.5. The contribution to the output noise due to the series noise source is equal to that of the triangular shaping with peaking

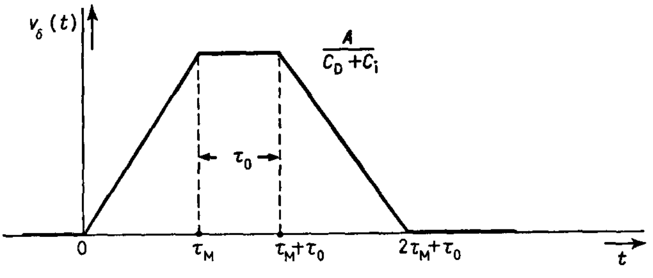

Fig. 4.5. – Trapezoidal shaping.

time τ_M. The contribution due to the parallel noise becomes instead

$$[\overline{v_N^2}]^{\frac{1}{2}} = \frac{A}{C_D + C_i}\left[\left(\frac{2}{3}\,\tau_M + \tau_0\right)b\right]^{\frac{1}{2}}. \tag{4.25}$$

The signal-to-noise ratio ϱ is given by

$$\varrho = \frac{Q}{[a(C_D + C_i)^2\,(2/\tau_M) + b\big((2/3)\,\tau_M + \tau_0\big)]^{\frac{1}{2}}} \tag{4.26}$$

and the equivalent noise charge is

$$\mathrm{ENC} = \left[a(C_D + C_i)^2\,\frac{2}{\tau_M} + b\left(\frac{2}{3}\,\tau_M + \tau_0\right)\right]^{\frac{1}{2}} \quad \text{r.m.s. coulomb}\,. \tag{4.27}$$

It can be taken advantage of the example of the trapezoidal shaping to make a statement of general validity. A processing system will be considered, which

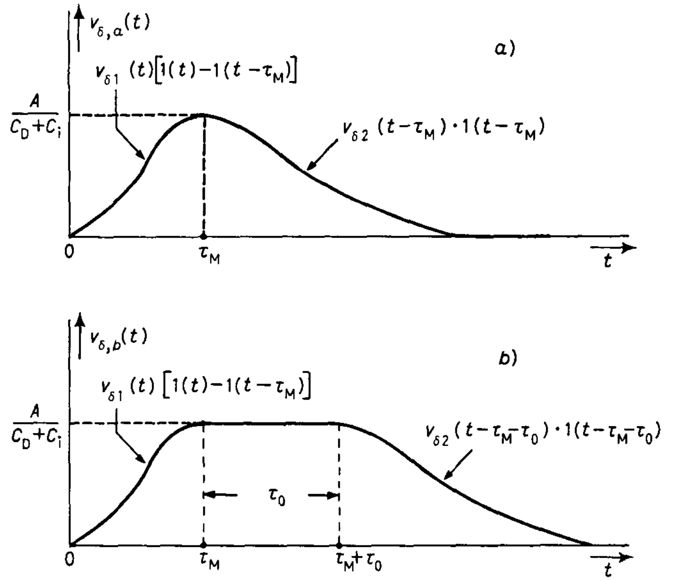

Fig. 4.6. – Responses $v_{\delta,a}(t)$ and $v_{\delta,b}(t)$ to the δ-impulse detector current. The two responses have equal leading and trailing edges. The response of *b*) differs from that of *a*) for a flat-topped region of duration τ_0.

is described by the $v_{\delta,a}(t)$ of fig. 4.6*a*) along with the system described by the $v_{\delta,b}(t)$ of fig. 4.6*b*).

As shown in fig. 4.6, $v_{\delta,a}(t)$ and $v_{\delta,b}(t)$ have the same leading and trailing edges; the peak region of $v_{\delta,a}$ is replaced by a flat-topped region of duration

τ_0 in $v_{\delta,b}(t)$. As the derivatives of $v_{\delta,a}$ and $v_{\delta,b}$ are equal, the contribution from the white series noise is the same in both cases. The presence of the flat-topped region in $v_{\delta,b}$ enhances the effect of the parallel noise to the extent shown by eq. (4.25) which compares the equivalent noise charge in the two cases:

$$\mathrm{ENC}^2_{v_{\delta b}} = \mathrm{ENC}^2_{v_{\delta a}} + b\tau_0 . \tag{4.28}$$

4.2.2.5. Bipolar shaping. Let $v_\delta(t)$ be the response of the analog processor to a δ-impulse detector current; it will be assumed that $v_\delta(t)$ has a finite width T and that it is strictly unipolar, as shown in fig. 4.7*a*). Let $v_{\delta 1}(t)$ be the δ-response obtained by applying to $v_\delta(t)$ the operator $1 - \exp[-sT]$ which adds to $v_\delta(t)$ a signal equal in shape to $v_\delta(t)$ but delayed of a time T and reversed in polarity. The bipolar signal $v_{\delta 1}(t)$ is shown in fig. 4.7*b*). Bipolar shaping is sometimes employed in processors intended for high counting rates owing to the following property. If the signal of fig. 4.7*b*) is passed through a transfer function which has a zero at $s = 0$, typical of an a.c. coupled processor, the tails of opposite sign determined by the positive and negative lobes cancel each other for $t > 2T$ fairly well. As a consequence, the baseline shifts at high counting rates, that are a serious limitation in a.c. coupled processors working on unipolar signals, are almost eliminated with bipolar shaping.

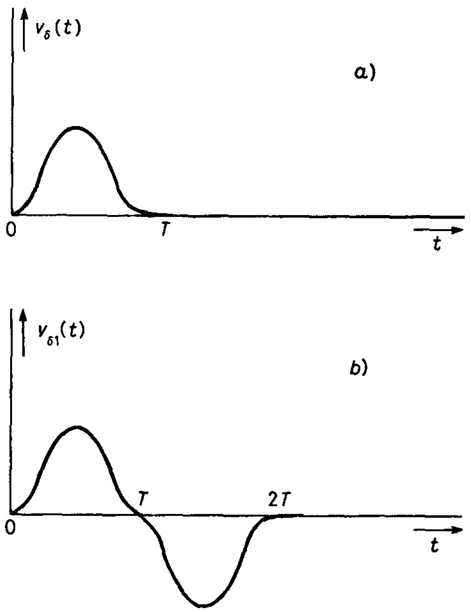

Fig. 4.7. – Unipolar response to the δ-impulse detector current (*a*)) and bipolar response obtained by delaying and reversing in polarity the previous one (*b*)).

As far as the signal-to-noise ratio goes, however, bipolar shaping is worse than the unipolar one. Time domain noise evaluation of cases *a*) and *b*) of fig. 4.7 leads to the conclusion that both series and parallel contributions to the output root-mean-square noise are increased of a factor $\sqrt{2}$ passing from unipolar to bipolar shaping.

4'3. *Contribution of the series* $1/|\omega|$ *noise to the output* r.m.s. *noise in some particular cases.* – Let $c/|\omega|$ be the bilateral power spectral density of the series noise whose contribution to the total root-mean-square output noise has to be evaluated. As already pointed out, the calculation has to be made in the frequency domain and only some cases of particular interest will be considered [15-18].

4'3.1. Triangular shaping. With reference to the shape shown in fig. 4.2 and to the procedure followed to determine the effect of series and parallel noise generators, the contribution due to the $c/|\omega|$ term is given by

$$\overline{v_N^2} = \frac{16A^2}{2\pi}\int_{-\infty}^{\infty}\frac{c}{|\omega|}\,\frac{\sin^4(\omega\tau_M/2)}{\omega^2\tau_M^2}\,d\omega = \frac{16A^2}{\pi}c\int_0^{\infty}\frac{\sin^4(\omega\tau_M/2)}{\omega^3\tau_M^3}\,d(\omega\tau_M) =$$

$$= \frac{4A^2}{\pi}c\int_0^{\infty}\frac{\sin^4 x}{x^3}\,dx \qquad \left(x = \frac{\omega\tau_M}{2}\right).$$

Introducing for the integral the value given in appendix, the following expression is obtained for the contribution of the $c/|\omega|$ term to the output r.m.s. noise:

$$\overline{v_N^2} = A^2 c\, 4\,\frac{\ln 2}{\pi}. \tag{4.29}$$

The contribution of the $1/|\omega|$ series term to the ENC is accordingly

$$\text{ENC} = 2\left(\frac{\ln 2}{\pi}c\right)^{\frac{1}{2}}(C_D + C_i) \approx 0.96\, c^{\frac{1}{2}}(C_D + C_i). \tag{4.30}$$

4'3.2. *RC-CR* shaping. With reference to fig. 4.3 and to the procedure followed to determine the signal-to-noise ratio for the *RC-CR* shaping, the following expression of the contribution given by the $c/|\omega|$ term to the output r.m.s. noise is obtained:

$$\overline{v_N^2} = \frac{A^2}{2\pi}\int_{-\infty}^{\infty}\frac{c}{|\omega|}\,\frac{\omega^2\tau_M^2}{1+\omega^2\tau_M^2}\,d\omega = \frac{cA^2}{\pi}\int_0^{\infty}\frac{x}{(1+x^2)^2}\,dx \qquad (x = \omega\tau_M).$$

Introducing for the integral the value given in appendix, the following expression is obtained for $\overline{v_N^2}$:

$$\overline{v_N^2} = \frac{cA^2}{2\pi}\,. \tag{4.31}$$

The contribution brought by the $1/|\omega|$ series noise to the total ENC is

$$\text{ENC} = e\left(\frac{c}{2\pi}\right)^{\frac{1}{2}}(C_D + C_i) \approx 1.08c^{\frac{1}{2}}(C_D + C_i)\,. \tag{4.32}$$

4·3.3. *RC*-$(CR)^2$ shaping. Although the *RC*-$(CR)^2$ shaper, consisting of the cascade connection of one approximate integration and two approximate differentiations, is of little interest in modern pulse processing, it is useful to evaluate its effect on the $1/|\omega|$ noise. If in the processor of fig. 4.1 the transfer function $T(s) = (s\tau)^2/(1 + s\tau)^3$ is introduced, the following $v_\delta(t)$ is obtained:

$$v_\delta(t) = \frac{A}{C_D + C_i}\,\frac{t}{\tau}\exp\left[-t/\tau\right]\left[1 - \frac{t}{2\tau}\right],$$

which is shown in fig. 4.8.

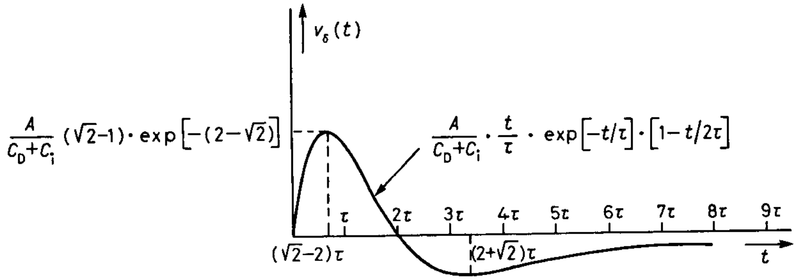

Fig. 4.8. – Bipolar shape obtained by passing the step at the preamplifier output through the cascade connection of one approximate integrator and two approximate differentiators.

The noise is evaluated from the integral

$$\overline{v_N^2} = \frac{c}{\pi}A^2\int_0^\infty \frac{\omega^3\tau^4}{(1+\omega^2\tau^2)^3}\,\mathrm{d}\omega = \frac{c}{\pi}A^2\int_0^\infty \frac{x^3}{(1+x^2)^3}\,\mathrm{d}x \qquad (x = \omega\tau)\,.$$

The value of the integral is $\frac{1}{4}$. The root-mean-square output noise due to the $1/|\omega|$ source is, therefore,

$$(\overline{v_N^2})^{\frac{1}{2}} = \frac{1}{2}\left(\frac{c}{\pi}\right)^{\frac{1}{2}}A\,. \tag{4.33}$$

The contribution to the total ENC is accordingly

$$\text{ENC} = \frac{1}{2}\left(\frac{c}{\pi}\right)^{\frac{1}{2}} \frac{\exp\left[2-\sqrt{2}\right]}{\sqrt{2}-1}\,(C_{\text{D}}+C_{\text{i}}) \approx 1.23\,c^{\frac{1}{2}}(C_{\text{D}}+C_{\text{i}})\,. \tag{4.34}$$

The evaluations made on the ENC contribution coming from the series $1/|\omega|$ noise show that it is independent of the shaper characteristic time τ_{R} and that it is very little dependent on the wave form determined by the shaper.

4'4. *Time-variant shapers.* – Time-variant shapers were proven to be of very practical usefulness in high-energy experiments and, therefore, the more significant examples of this class of circuits will be discussed [19-27]. From a strictly conceptual standpoint, time-variant shapers do not allow better signal-to-noise ratio or counting rate performances or lower pile-up probability than the best time-invariant shapers. If the comparison between time-variant and time-invariant shapers is, however, transferred to the ground of actual behaviour, of requirements set to the instrumentation which follows and of the additional facilities they offer, the former ones have to be considered with favour in the context of elementary-particle physics. In this domain of applications, especially when fixed-target experiments are considered, the analog processors are subject to extremely high rates of events, while for very few of them the requirements of the selection logic are met. In a time-invariant shaper, all the incoming pulses are processed in the same way, while a time-variant shaper for high-energy experiment is usually a gated network which completes the processing only on those events for which the selection requirements are met. Time-variant shapers offer as advantages a fast, tail-free recovery to the baseline at the end of the shaped pulses, a built-in gating function so that at their output the counting rate is small and, in some configurations, a built-in analog store facility is easily implemented.

As pointed out by the authors [27], time-variant shapers belong to two different categories according to whether shaping occurs entirely after gating or whether a preshaping is performed before and shaping is completed after the gating. The block diagram of a time-variant shaper of the former type is shown in fig. 4.9.

The most common time-variant filter of the latter type is shown in fig. 4.10, where the second part of the shaping is done by a gated integrator.

The attractive aspect of this time-variant shaper lies in the fact that most ADCs for high-energy experiments are of the charge-sensitive type, that is, they employ a gated integrator as input analog memory. It becomes, therefore, natural to commit to this integrator the twofold function of time-variant shaper and analog store of the amplitude to be measured.

The noise analysis of time-variant shapers has to be carried out in the time domain. The approach, however, is more involved than the one adopted for

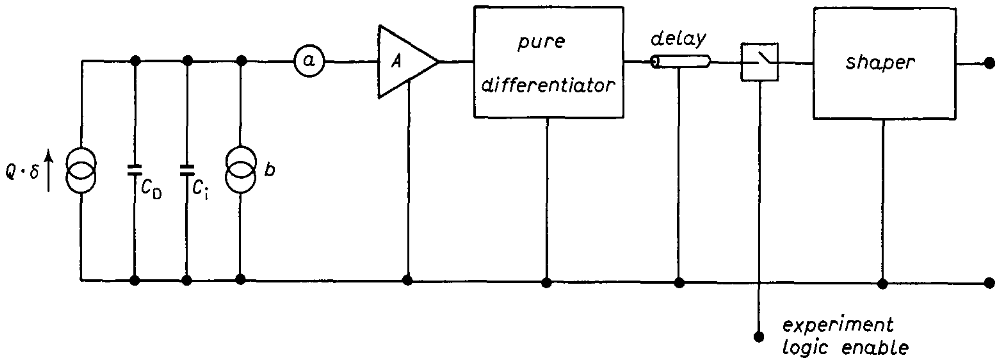

Fig. 4.9. – Time-variant shaper with the shaping entirely performed after the gate.

the time-invariant shapers. In the case of a time-invariant shaper the δ-impulses that describe the series and parallel noise generator induce at the output signals whose form is independent of the instant at which the exciting δ occurs. The knowledge of the response of the processor to a δ-impulse detector signal allows, as was shown, a straightforward evaluation of the root-mean-square output noise through Campbell's theorem. In a time-variant shaper the switch opening is synchronized with the arrival of the signal to be analysed and the contribution of the δ-impulse describing the series and parallel noise generator to the root-mean-square noise at the measuring instant depends on their time relationship with the signal.

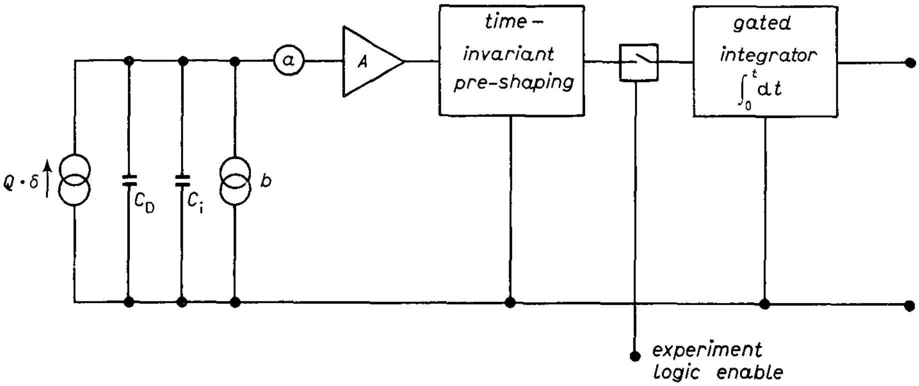

Fig. 4.10. – Time-variant shaper employing a gated integrator.

The knowledge of the processor response to the δ-impulse-like detector current is not sufficient to evaluate the noise. This is especially true for the shapers of the type shown in fig. 4.10. The following description of the behaviour of the two types of time-invariant filters does not claim to be a comprehensive treatment of the problem, but rather an intuitive approach to their use. As shown in fig. 4.9, the preamplifier is followed by a differentiator which reproduces the original shape of the detector current pulses. The δ's describing the parallel white-noise source appear again as δ-impulses at the differentiator output, while the δ-impulses describing the series white noise are transformed by the differentiator into doublets. An over-simplified explanation of the deterioration in signal-to-noise ratio, which may occur in this kind of shaper if a proper time relationship between switch opening and signal arrival is not respected, lies on the split-doublet effect [20].

The opening of the switch may cause a doublet splitting.

The uncompensated part of the doublet will impair the signal-to-noise ratio unless the shaper which follows the switch responds to the split doublet (a δ-like pulse of ∞ area) with a signal which goes to zero at the measurement instant.

To avoid this effect, the time relationships shown in fig. 4.11 are employed.

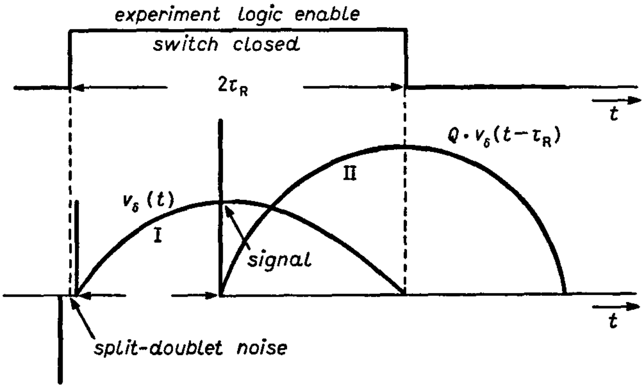

Fig. 4.11. – Timing sequence in a time-invariant shaper of the first type.

It is assumed that the shaper which follows the switch has a δ-impulse response with a peak at $t = \tau_R$ and a base width $2\tau_R$ and that this response is symmetric.

Whenever the experiment logic requirements are met, a switch opening command is generated with a time duration $2\tau_R$. A doublet which may be split by the gate opening excites in the shaper a response which reaches zero at $t = 2\tau_R$. The signal to be analysed is delayed of τ_R, so as to appear in the middle of the opening interval. The response it excites in the shaper reaches its maximum at the end of the opening interval, that is, when the response to the split doublet is zero. The amplitude measurement is performed at $t = 2\tau_R$.

If the effect of split doublet is avoided in the way shown, the root-mean-square noise at the measurement instant can be calculated with the same procedure adopted for the time domain analysis of time-invariant shapers. This is a consequence of the fact that all the shaping is concentrated after the switch and, therefore, all the δ-impulses and doublets that occur when the switch is open excite the same outputs, respectively $v_\delta(t)$ or $v'_\delta(t)$. A time-variant filter of the type just described was employed in the coherent-production experiment of π-mesons on the nucleus of Si [25]. The δ-impulses transmitted by the gate excite a sinusoid in an active filter. The time relationships between switch opening and incoming detector signal are identical to those depicted in fig. 4.11. The amplitude measurement is performed on the peak of the first lobe of the sinusoid. Shortly after the peak of the first lobe, the sinusoid is nonlinearly damped. The system has a very good behaviour at high counting rates by virtue of a very neat, tail-free differentiation of the signals at the preamplifier output and of the symmetric δ-response of the sinusoidal filter in the linear mode. The case of the sinusoidal shaper after the switch will be analysed here, just to show in a practical case an example of evaluation of the signal-to-noise ratio. As already pointed out, throughout the opening interval of the gate and as long as the split-doublet effect is neglected, the shaper is described, like a time-invariant one, by the response $v_\delta(t)$ to a unit δ detector current.

For the sinusoidal shaper

$$v_\delta(t) = \frac{A}{C_D + C_i}\sin\frac{\pi t}{2\tau_R}\cdot 1(t)\,. \tag{4.35}$$

The response of the sinusoidal shaper to a unit δ delivered by the parallel noise generator is $v_\delta(t)$, while the response of the sinusoidal shaper to a unit δ delivered by the series voltage generator is, according to (4.14),

$$(C_D + C_i)v'_\delta(t) = \frac{A\pi}{2\tau_R}\cos\frac{\pi t}{2\tau_R}\cdot 1(t)\,. \tag{4.36}$$

The root-mean-square output noise is, therefore,

$$[\overline{v_N^2}]^{\frac{1}{2}} = \left\{a\frac{A^2\pi^2}{4\tau_R^2}\int\limits_0^{2\tau_R}\cos^2\frac{\pi t}{2\tau_R}\,\mathrm{d}t + b\,\frac{A^2}{(C_D + C_i)^2}\int\limits_0^{2\tau_R}\sin^2\frac{\pi t}{2\tau_R}\,\mathrm{d}t\right\}^{\frac{1}{2}} = $$

$$= A\left\{a\frac{\pi^2}{4}\,\frac{1}{\tau_R} + \frac{b}{(C_D + C_i)^2}\,\tau_R\right\}^{\frac{1}{2}}.$$

The signal amplitude is $QA/(C_D + C_i)$. The signal-to-noise ratio ϱ and the equivalent noise charge ENC are, respectively,

$$\varrho = \frac{Q}{[(\pi^2/4)(C_D + C_i)^2(a/\tau_R) + b\tau_R]^{\frac{1}{2}}}\,, \tag{4.37}$$

$$\mathrm{ENC} = \left[\frac{\pi^2}{4}(C_D + C_i)^2\frac{a}{\tau_R} + b\tau_R\right]^{\frac{1}{2}} \text{ r.m.s. coulomb}\,. \tag{4.38}$$

A method will now be presented which allows a straightforward calculation of the signal-to-noise ratio for the time-variant shaper of fig. 4.10.

Let $(A/(C_D + C_i))p(t)\cdot 1(t)$ be the signal at the output of the time-invariant preshaper induced by a unit δ detector current. It will be assumed that $p(t)$ has a finite width τ_p (fig. 4.12*a*)).

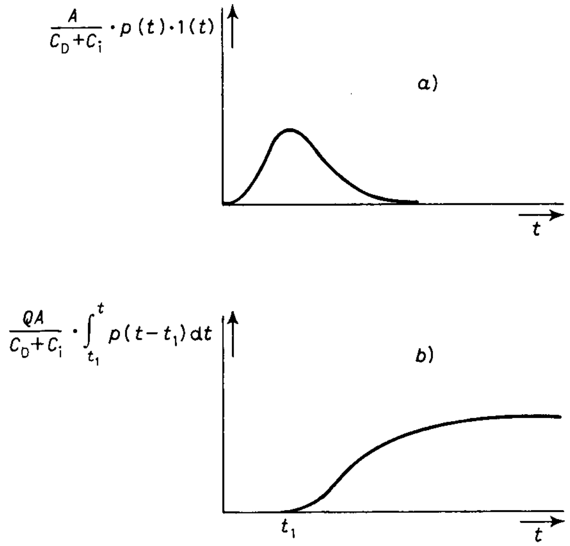

Fig. 4.12. – *a*) Signal at the preshaper output induced by a current δ in the detector. *b*) Gated integration of the signal occurring at the preshaper output beginning at $t = t_1$.

A detector signal of charge Q occurring at $t = t_1$ will produce at the preshaper output the signal

$$\frac{QA}{C_D + C_i}\,p(t - t_1)\cdot 1(t - t_1)\,.$$

The switch opening is synchronized with the arrival of the detector signal and the switch remains open for a duration $\tau_R \geqslant \tau_p$.

The signal $(QA/(C_D + C_i))p(t - t_1)\cdot 1(t - t_1)$ is integrated over the time interval $(t_1, t_1 + \tau_R)$ and the amplitude measurement is performed at $t = t_1 + \tau_R$, after which the integrator is reset.

The noise evaluation of this time-variant filter is based upon a time domain approach which requires the knowledge of the so-called « noise weighting function » [13, 19, 20].

Contrary to what happens in a time-variant filter of the type of fig. 4.9, where no preshaping exists, in the time-variant filter of the type of fig. 4.10, the signals arriving to the gate have a finite width. This means that all the δ-impulses delivered by the parallel and series noise generator in the time interval $(t_1 - \tau_p, t_1)$ as well as those occurring between t_1 and $t_1 + \tau_R$ contribute to the noise at the measuring instant.

The « noise weighting function » is defined as the contribution to the noise at the measuring time $t = \tau_R$ given by a δ-impulse delivered by the parallel noise generator at a time t_0 and expressed as a function of t_0 between $t_1 - \tau_p$ and $t_1 + \tau_R$.

The way of evaluating the noise weighting function at different instants t_0 is shown in fig. 4.13. The noise weighting function at a given t_0 is represented by the area of the shaded region of the signal induced at the preshaper output by a δ-impulse from the parallel noise source.

This accounts for the fact that a δ-impulse from the parallel source, which is in the same circuit position as the signal source, induces at the prefilter outpnt a signal whose shape is $p(t)$. The portion of this signal which enters the gate is integrated and stored in the integrator, therefore contributing to the noise at $t = t_1 + \tau_R$.

As clarified by fig. 4.13, the weighting function can be expressed in the following way:

$$W(t_0) = 0 \qquad \text{for } t_0 < t_1 - \tau_p \text{ and } t_0 > t_1 + \tau_R\,,$$

$$W(t_0) = \frac{A}{C_D + C_i}\int\limits_0^{t_0+\tau_p-t_1} p(\tau_p - x)\,\mathrm{d}x\,, \qquad t_1 - \tau_p < t_0 < t_1\,,$$

$$W(t_0) = \frac{A}{C_D + C_i}\int\limits_0^{\tau_p} p(\tau_p - x)\,\mathrm{d}x\,, \qquad t_1 < t_0 < t_1 + \tau_R - \tau_p\,,$$

$$W(t_0) = \frac{A}{C_D + C_i}\int\limits_0^{t+\tau_R-\tau_0} p(x)\,\mathrm{d}x\,, \qquad t_1 + \tau_R - \tau_p < t_0 < t_1 + \tau_R\,.$$

Once $W(t_0)$ is determined, the noise contributions from the parallel source can be evaluated by adding quadratically all the elementary contributions appearing at the integrator output and caused by δ-impulses occurring in the time intervals t_0, $t_0 + \mathrm{d}t_0$ as t_0 varies. That is,

$$(\overline{v_N^2})_p^{\frac{1}{2}} = \frac{A}{C_D + C_i}\left[b\int\limits_{t_1-\tau_p}^{t_1+\tau_R} W^2(x)\,\mathrm{d}x\right]^{\frac{1}{2}}. \tag{4.39}$$

By sliding in a similar manner the derivative of $(A/(C_D + C_i))p(t)$ through the integrator window, the noise weighting function for doublets of current injected across the C_D, C_i parallel combination can be determined. The resulting function, which is the derivative of $W(t)$ of fig. 4.13, allows the calculation of the output noise arising from the white term in the series generator of fig. 4.1.

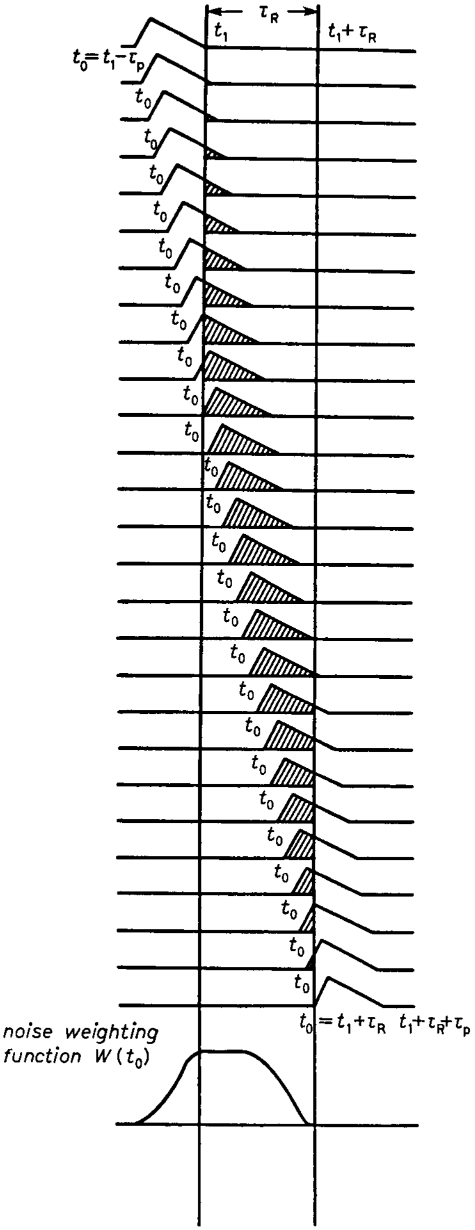

Fig. 4.13. – Graphical evaluation of the noise weighting function $W(t)$.

The root-mean-square output noise due to the series generator is

$$[\overline{v_{\mathrm{N}}^2}]_{\mathrm{s}}^{\frac{1}{2}} = A\left[a\int_{t_1-\tau_p}^{t_1+\tau_{\mathrm{R}}}[W'(x)]^2\,\mathrm{d}x\right]^{\frac{1}{2}}. \tag{4.40}$$

The signal-to-noise ratio ϱ and the equivalent noise charge ENC are, respectively, given by the following equations:

$$\varrho = \frac{Q\int_0^{\tau_{\mathrm{R}}} p(x)\,\mathrm{d}x}{\left\{a(C_{\mathrm{D}}+C_{\mathrm{i}})^2\int_{t_1-\tau_p}^{t_1+\tau_{\mathrm{R}}}[W'(x)]^2\,\mathrm{d}x + b\int_{t_1-\tau_p}^{t_1+\tau_{\mathrm{R}}}W^2(x)\,\mathrm{d}x\right\}^{\frac{1}{2}}}, \tag{4.41}$$

$$\mathrm{ENC} = \frac{\left\{a(C_{\mathrm{D}}+C_{\mathrm{i}})^2\int_{t_1-\tau_p}^{t_1+\tau_{\mathrm{R}}}[W'(x)]^2\,\mathrm{d}x + b\int_{t_1-\tau_p}^{t_1+\tau_{\mathrm{R}}}W^2(x)\,\mathrm{d}x\right\}^{\frac{1}{2}}}{\int_0^{\tau_{\mathrm{R}}} p(x)\,\mathrm{d}x}\ \text{r.m.s. coulomb}. \tag{4.42}$$

Both equations point out the fact that the knowledge of two different functions, namely $p(x)$ for the signal and $W(x)$ for the noise, is required in the analysis of a time-variant shaper of the type of fig. 4.10.

Two examples will clarify the behaviour of time-variant filters employing the gated integrator. A processor in which $p(t)$ is a unit-amplitude rectangle of duration τ_p responds to a δ-shaped signal with the function of fig. 4.14*b*). The noise weighting function, instead, has the symmetric shape of fig. 4.14*c*). The signal-to-noise ratio and the equivalent noise charge are identical to those

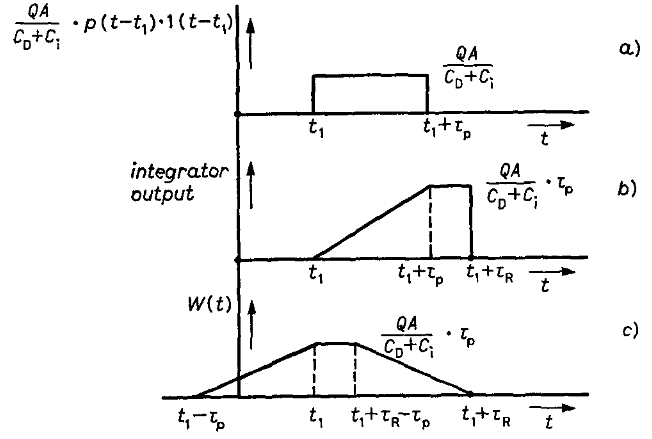

Fig. 4.14. – Wave forms at the input and at the output of the gated integrator (*a*), *b*)) and noise-weighting function (*c*)).

calculated in the case of the time-invariant trapezoidal shaper, with $\tau_M = \tau_p$ and $\tau_0 = \tau_R - \tau_p$.

If the duration of the signal at the preshaper output is made equal to τ_R, then the flat top in the wave forms 4.14*a*) and *b*) disappears and the noise weighting function becomes a triangle of base width $2\tau_R$.

A processor for which $p(t)$ is a triangle of base width $\tau_p = \tau_R$ presents the wave forms and the noise weighting function of fig. 4.15.

The signal-to-noise ratio and the equivalent noise charge are identical to those evaluated for the piecewise parabolic shaper and their values are given by eqs. (4.23), (4.24), where $\tau_M = \tau_R$.

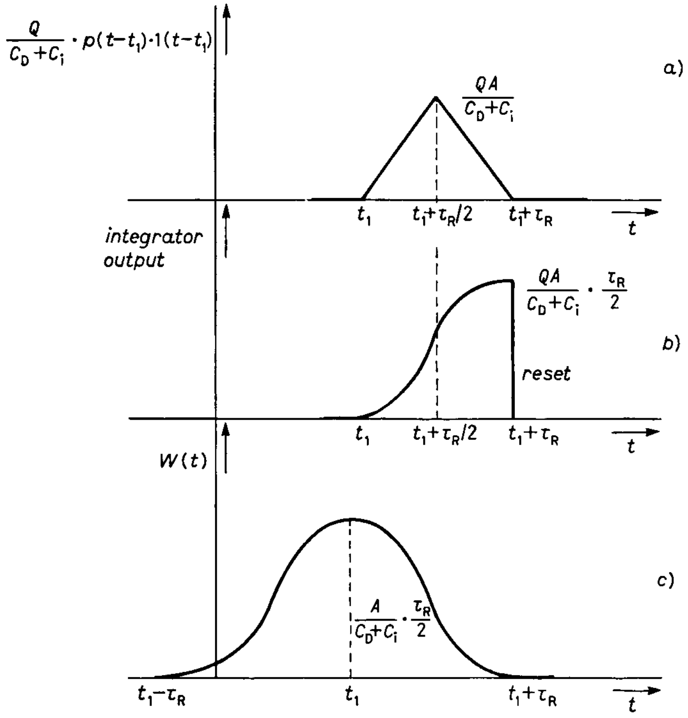

Fig. 4.15. – Wave forms at the input and output of the gated integrator (*a*), *b*)) and noise weighting function (*c*)).

As a general comment to sect. **3** and **4** it has to be pointed out that they were basically oriented to the analysis of shapers suitable for energy measurements. Shaping problems related to time measurements, for instance, were purposely neglected. It is, however, important to quote, among the shapers that have been omitted, the antisymmetric-ramp one, which is employed in the evaluation of the centroid of an arbitrary input signal [28]. The antisymmetric-ramp shaper is of particular importance in some kinds of position-sensing applications.

REFERENCES

[1] E. Baldinger and W. Franzen: *Adv. Electron. Electron Phys.*, **8**, 225 (1956).

[2] V. Radeka: *IEEE Trans. Nucl. Sci.*, NS-**19**, 412 (1972).

[3] E. Fairstein and J. Hahn: *Nuclear pulse amplifiers. Fundamental and design practice*, Part I: *Nucleonics*, **23**(7), 56 (1965); Part II: *Nucleonics*, **23**(9), 81 (1965); Part III: *Nucleonics*, **23**(11), 50 (1965); Part IV: *Nucleonics*, **24**(1), 54 (1966); Part V: *Nucleonics*, **24**(3), 68 (1966).

[4] W. R. Bennett: *Proc. IRE*, **44**, 609 (1956).

[5] J. S. Bendat: *Principles and Applications of Random Noise Theory* (J. Wiley and Sons, New York, N. Y., 1958).

[6] A. B. Gillespie: *Signal, Noies and Resolution in Nuclear Counter Amplifiers* (Pergamon Press, London, 1953).

[7] P. W. Nicholson: *Nuclear Electronics* (J. Wiley and Sons, London, 1974).

[8] S. Cova and A. Longoni: *An introduction to signals, noise and measurements*, in *Analytical Laser Spectroscopy*, edited by N. Omenetto (J. Wiley and Sons, London, 1979).

[9] S. O. Rice: *Bell Syst. Tech. J.*, **23**, 282 (1944).

[10] J. R. Carson: *Bell Syst. Tech. J.*, **10**, 374 (1931).

[11] A. Van Der Ziel: *Noise-Sources, Characterization, Measurements* (Prentice-Hall, Inc., Englewood Cliffs, N. J., 1970).

[12] M. O. Deighton: *Nucl. Instrum. Methods*, **58**, 201 (1968).

[13] F. S. Goulding: *Nucl. Instrum. Methods*, **100**, 493 (1972).

[14] A. Hrisoho: *Nucl. Instrum. Methods*, **185**, 207 (1981).

[15] V. Radeka: *1/f noise in physical measurements*, in *Proceedings of the 1969 Ispra Nuclear Electronics Symposium*, Publ. EUR 4289-e (1969), p. 1.

[16] A. Van Der Ziel: *Adv. Electron. Electron Phys.*, **49**, 225 (1979).

[17] V. Radeka: *Nucl. Instrum. Methods Phys. Res.*, **226**, 209 (1984).

[18] P. F. Manfredi and F. Ragusa: *Nucl. Instrum. Methods Phys. Res. A*, **235**, 345 (1985).

[19] M. Conrad: *IEEE Trans. Nucl. Sci.*, NS-**15**, 268 (1968).

[20] V. Radeka: *IEEE Trans. Nucl. Sci.*, NS-**15**, 455 (1968).

[21] K. Kandiah: *High resolution spectrometry with nuclear radiation detectors*, AERE Report-R 6699-Harwell (1971).

[22] V. Radeka and N. Karlovac: *Time-variant filters for high-rate pulse amplitude spectrometry*, in *Proceedings of the Gatlinburg Conference on Semiconductor Radiation Detectors and Circuits*, National Academy of Sciences, Publication 1593 (1969), p. 553.

[23] K. Kandiah, A. J. Smith and G. White: *A pulse processor for* X-*ray spectrometry with* Si(Li) *detectors*, in *Proceedings of the II* ISPRA *Nuclear Electronics Symposium*, Publ. EUR 5370 e (1975), p. 153.

[24] A. J. Kalinin: private communication, Serpukhov, USSR (1977).

[25] M. Artuso, P. D'Angelo, E. Gatti, P. F. Manfredi and D. Marioli: *High rate pulse processing system for silicon active targets*, in *Proceedings of the X International Symposium on Nuclear Electronics, Dresden, GDR, 1980*, Vol. **2** (1980), p. 24.

[26] F. S. Goulding and D. A. Landis: *IEEE Trans. Nucl. Sci.*, NS-**29**, 1125 (1982).

[27] E. Gatti and P. F. Manfredi: *Nucl. Instrum. Methods Phys. Res.*, **226**, 142 (1984).

[28] E. Gatti, G. Padovini, L. Quartapelle, N. E. Greenlaw and V. Radeka: *IEEE Trans. Nucl. Sci.*, NS-**26**, 2910 (1979).

5. – Identification of the noise sources in preamplifier, detector and related bias networks.

5·1. *Noise sources, in the input amplifying device.* – In order to apply the theory developed about signal processing and signal-to-noise ratio, it is now necessary to discuss the explicit forms of the *a* and *b* noise generators for different kinds of preamplifying active devices, to account for the noise associated with the detector and to analyse the noise sources associated with the related bias networks. It will still be assumed that the preamplifier consists of a voltage-sensitive configuration of the type shown in fig. 5.1*a*), *b*), where the input active device is either a grounded-emitter bipolar transistor or a grounded-source field-effect transistor.

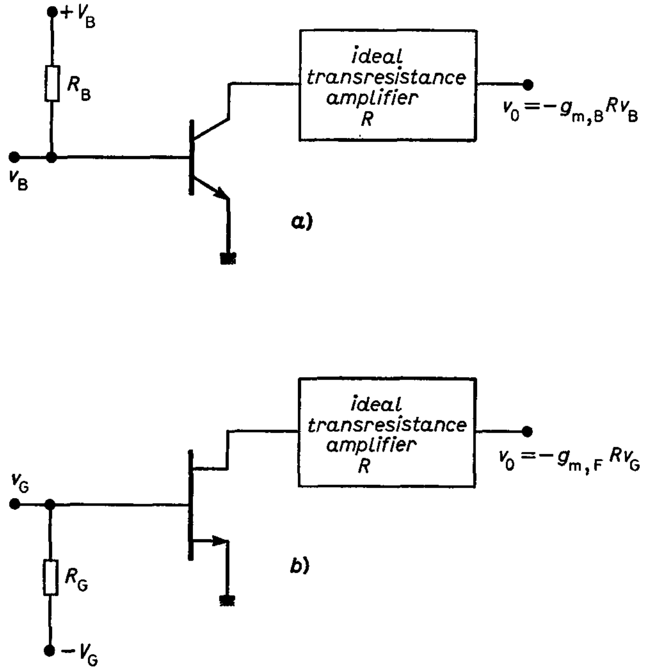

Fig. 5.1. – Voltage-sensitive preamplifiers employing as input device a grounded-emitter bipolar transistor (*a*)) and a grounded-source field-effect transistor (*b*)).

In both circuits of fig. 5.1, the output current from the first amplifying device is injected into an ideal transresistance amplifier, so that the voltage gains of the two amplifiers are, respectively, $-g_{m,B}R$ and $-g_{m,F}R$, where $g_{m,B}$ is the transconductance of the bipolar transistor and $g_{m,F}$ that of the field-effect transistor. The bipolar transistor is biased by fixing through the resistor

R_B connected to the $+V_B$ voltage supply its standing base current. The junction field-effect transistor is biased by connecting its gate to a negative voltage source $-V_G$ through the resistor R_G. The bias network of fig. 5.1*b*) can be used, with a proper choice of value and polarity of V_G, also for depletion-type or enhancement-type MOS field-effect transistors.

The contributions determining the $a(\omega)$ series noise spectrum and the $b_1(\omega)$ parallel spectrum will now be discussed for the different types of active device. For this analysis the transresistance amplifier R will be considered noiseless.

5'1.1. Silicon junction field-effect transistor. The silicon junction field-effect transistor is still the leading device for low-noise applications at values of the processing times, either τ_M or τ_R, ranging from a few hundreds of nanoseconds to several tens of microseconds.

The small-signal equivalent circuit of the silicon junction field-effect transistor with the noise sources is shown in fig. 5.2.

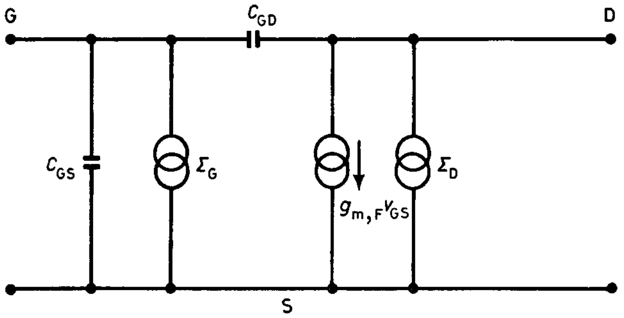

Fig. 5.2. – Small-signal equivalent circuit of the junction field-effect transistor including the dominant noise sources.

For a thorough analysis of the physical phenomena responsible for the noise behaviour of silicon field-effect transistors the reader can refer to the available literature [1-5].

From the point of view of the noise sources, the model of fig. 5.2 is a simplified one. Among the simplifications introduced, the effect of thermal noise in the channel coupled to the gate has been neglected.

In fig. 5.2 the two current sources with bilateral densities Σ_G and Σ_D account, respectively, for the shot noise in the gate leakage current and for the thermal noise in the channel. Their expressions are

$$\Sigma_G = qI_G\,, \tag{5.1}$$

$$\Sigma_D = 2kT\cdot 0.7\, g_{m,F}\,. \tag{5.2}$$

In the previous relationships q is the electron charge, $q = 1.6\cdot 10^{-19}$ C, k is

Boltzmann's constant, $k = 1.38 \cdot 10^{-23}$ J/K, T is the absolute temperature and I_G is the gate leakage current. The equivalent circuit of fig. 5.2 can be redrawn in a form closer to the representation of fig. 3.1 by referring the thermal noise in the channel to the input and by remembering that in the circuit diagram 5.2*b*) the drain of the JFET is connected to an ideal current input. The new equivalent circuit is shown in fig. 5.3.

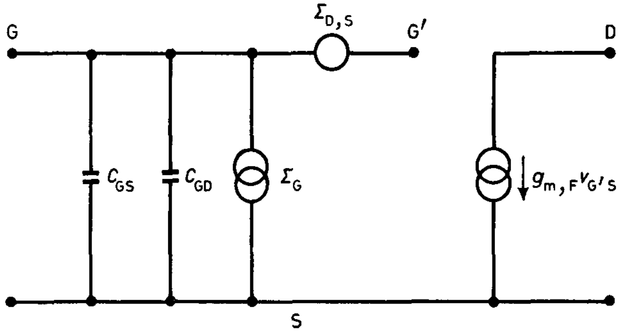

Fig. 5.3. – Equivalent circuit of the junction field-effect transistor with a series voltage source accounting for the thermal noise in the channel.

In the circuit of fig. 5.3 the thermal noise in the channel is accounted for by the series voltage source with bilateral power spectral density

$$\Sigma_{D,S} = 2kT\,\frac{0.7}{g_{m,F}}\,. \tag{5.3}$$

The transconductance $g_{m,F}$ is related to the pinch-off voltage V_P and to the drain current I_{DS} in the saturation region by the relationship [6]

$$g_{m,F} \simeq 3\,\frac{I_{DS}}{V_P}\,, \tag{5.4}$$

where the maximum of I_{DS} is I_{DSS}, the drain saturation current. According to (5.4) a device with a 1V V_P would exhibit a $g_{m,F}$ of 30 mA/V at a drain current of 10 mA.

Such a value of g_m/I_{DS} is an upper limitation among silicon JFETs, whereas an average good device has typically 10 mA/V at $I_{DS} = 10$ mA.

The intrinsic contribution to the parallel noise in a silicon junction field-effect transistor is the shot noise in the gate leakage current I_G. The values of I_G range between 10^{-12} A and 10^{-10} A at $T = 300$ K.

The junction field-effect transistor is a majority carrier device whose gain-bandwidth product is limited by the transit time in the channel. The gain-bandwidth product, which in terms of concentrated parameters can be shown to be equal to the $g_{m,F}/(C_{GD} + C_{GS})$ ratio, has the following upper limitation:

$$\omega_{T,F} < \frac{\mu V_P}{\pi L^2}, \tag{5.5}$$

where L is the length of the channel and μ is the mobility of the carriers.

Comparing the equivalent circuit of fig. 5.3 with the general block diagram of fig. 3.1, it can be concluded that the preamplifier input capacitance C_i is the sum of C_{GS} and C_{GD}, that the spectral power density a is represented by $\Sigma_{D,S}$ and that the spectral power density b_1 is represented by Σ_G.

5·1.2. Bipolar transistors. The equivalent circuit which summarizes the signal action and the noise characteristics of the bipolar transistor is shown in fig. 5.4 [7, 8].

In the diagram of fig. 5.4 $R_{BB'}$ is the base spreading resistance, R_B is the incremental base resistance, which depends on the base standing current I_B according to the relationship $R_B = kT/qI_B$, C_B is the sum of the base-to-emitter diffusion and junction capacitances. $C_{OB'}$ is the capacitance of the base-collector junction. In ordinary operating conditions the base-to-emitter junction capacitance is small compared to the diffusion one and, therefore, it will be assumed that C_B represents the diffusion capacitance.

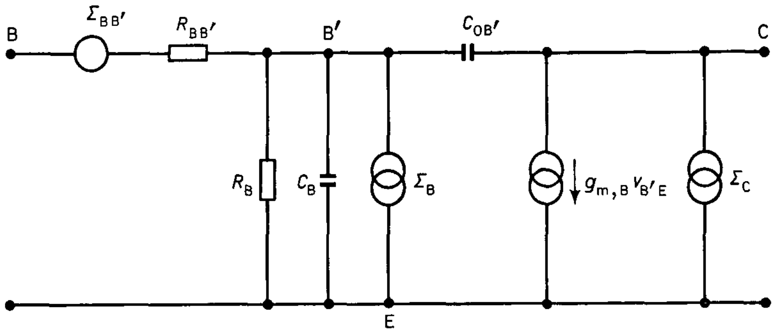

Fig. 5.4. – Small-signal equivalent circuit of the bipolar transistor including the dominant noise sources.

As to the noise sources, $\Sigma_{BB'}$ is the bilateral spectral power density of the generator which accounts for the thermal noise in the base spreading resistance, Σ_B is the bilateral spectral power density of the generator describing the shot noise in the base current and Σ_C the one of the generator describing the shot noise in the collector current I_C. Their expressions are

$$\Sigma_{BB'} = 2kTR_{BB'}\,, \tag{5.6}$$

$$\Sigma_B = qI_B\,, \tag{5.7}$$

$$\Sigma_C = qI_C\,. \tag{5.8}$$

The circuit of fig. 5.4 can be transformed into that of fig. 5.5, where the shot

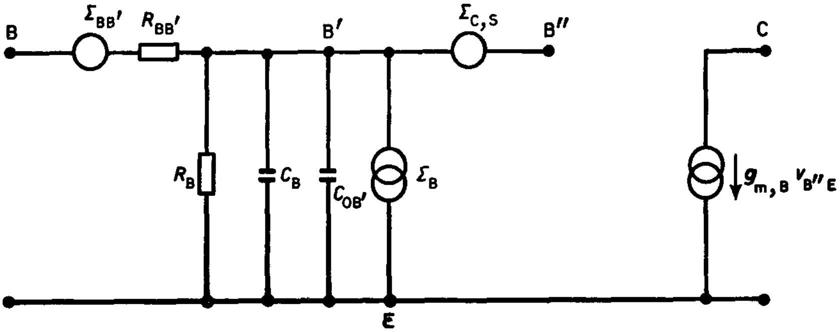

Fig. 5.5. – Equivalent circuit of the bipolar transistor with a series voltage source, $\Sigma_{C,S}$, accounting for the collector shot noise.

noise in the collector current is accounted for by the series voltage generator $\Sigma_{C,S}$. The $C_{OB'}$ capacitance has been represented in parallel to C_B as in the practical application of fig. 5.1*a*) the collector of the transistor terminates to a zero-impedance input. In the ordinary operating conditions $C_{OB'}$ is negligible compared to the base diffusion capacitance.

The spectral power density $\Sigma_{C,S}$ is expressed by

$$\Sigma_{C,S} = \frac{qI_C}{g^2_{m,B}}\,. \tag{5.9}$$

Remembering that $g_{m,B} = qI_C/kT$, $\Sigma_{C,S}$ can be rewritten in a form close to the one seen for the thermal noise referred to the input in a field-effect transistor, that is,

$$\Sigma_{C,S} = 2kT\,\frac{0.5}{g_{m,B}}\,. \tag{5.10}$$

If the thermal voltage $V_T = kT/q = 25$ mV at $T = 300$ K is introduced into the expression of $g_{m,B}$ and the ratios

$$\frac{g_{m,B}}{I_C} = \frac{1}{V_T} \quad \text{and} \quad \frac{g_{m,F}}{I_{DS}} = \frac{3}{V_P}$$

are compared, it can be concluded that the ratio between transconductance and standing current for the bipolar transistor is more than an order of magnitude larger than for the junction field-effect transistor.

The spectral power density $\Sigma_{\mathrm{C,S}}$ gives a first contribution to the series generator a in the general diagram of fig. 3.1. A second contribution, which from the circuit diagram of fig. 5.5 can be evaluated to be equal to

$$2kTR_{\mathrm{BB'}}\,\frac{C_{\mathrm{D}}^2}{(C_{\mathrm{D}}+C_{\mathrm{i}})^2}\,, \tag{5.11}$$

is due to the thermal noise in the base spreading resistance. Therefore, with reference to fig. 3.1, it can be written for the white-noise part a_{w} of the series spectral power density

$$a_{\mathrm{w}} = 2kT\,\frac{0.5}{g_{\mathrm{m,B}}} + 2kTR_{\mathrm{BB'}}\,\frac{C_{\mathrm{D}}^2}{(C_{\mathrm{D}}+C_{\mathrm{B}})^2}\,, \tag{5.12}$$

having neglected $C_{\mathrm{OB'}}$. As shown by (5.12), the contribution to the series white noise introduced by $R_{\mathrm{BB'}}$ depends on the $C_{\mathrm{D}}/C_{\mathrm{B}}$ ratio, being zero at $C_{\mathrm{D}} = 0$ and approaching $2kTR_{\mathrm{BB'}}$ when $C_{\mathrm{D}} \gg C_{\mathrm{B}}$. The base spreading resistance in a microwave bipolar transistor featuring typically more than 5 GHz gain-bandwidth product at a collector current of 5 mA can be in the $(10\div15)\,\Omega$ range.

The bipolar transistor has a large parallel noise source related to the shot noise in the base leakage current. The spectral power density of the generator b_1 in fig. 3.1 is

$$b_1 = \Sigma_{\mathrm{B}} = qI_{\mathrm{B}}\,. \tag{5.13}$$

The usual values of I_{B} in nuclear detector applications are in the $(10\div100)\,\mu\mathrm{A}$ range.

The gain-bandwidth product ω_{T} in a bipolar transistor can be expressed as [6]

$$\omega_{\mathrm{T}} = \frac{g_{\mathrm{m,B}}}{C_{\mathrm{B}}} = \frac{2\mu V_{\mathrm{T}}}{L^2}\,, \tag{5.14}$$

where μ is the mobility of minority carriers in the base region and L is the base width.

Although the presence of the large parallel noise requires that the bipolar transistor be employed at a value of the collector current substantially lower than the one at which the maximum of ω_{T} occurs, that is, I_{C} below 1 mA, still values of ω_{T} of 2π Grad/s can be achieved.

5·1.3. GaAs junction field-effect transistors. Compared to the silicon field-effect transistor, the Schottky-barrier GaAs junction field-effect transistor has a better $g_{\mathrm{m}}/I_{\mathrm{DS}}$ ratio and a much larger ω_{T}, this feature being related to the higher mobility of electrons in GaAs. As a disadvantage, the GaAs Schottky-barrier device has a parallel noise substantially greater, I_G approaching 1 μA and even more and a nonnegligible $1/|\omega|$-type series noise [9].

5'1.4. MOS transistors. The favour for MOS transistors as input devices of preamplifiers for solid-state detectors is presently growing because of two considerations. First, the MOS-VLSI technology might provide in the long run a solution to the readout problems associated with microstrip detectors. Secondly, discrete dual-gate MOS transistors with a large g_m/I_D ratio, a large gain-bandwidth product and a relatively small $1/|\omega|$ series noise are providing in some applications useful alternative solutions in the areas that were usually covered by silicon junction field-effect transistors [10-12]. For instance, the BF992 Philips dual-gate MOSFET has values of c in eq. (5.15) as small as $10^{-12}\,V^2$, that correspond to ENC contributions due to $1/|\omega|$ series noise of about 100 electrons r.m.s. at $C_D = 0$. In the range of τ_M values, where the ENC is governed by the $1/|\omega|$ series noise, slopes $d(\mathrm{ENC})/dC_D$ as small as 5 electrons/pF can be achieved with BF992.

VLSI processes with a very short channel, from a very few μm to less than 1 μm, are providing devices with a very large gain-bandwidth product, in the several GHz range [13].

As already pointed out, the series generator in MOS devices has a spectral power density expressed approximately as [9]

$$a(\omega) = a_w + \frac{c}{|\omega|}, \tag{5.15}$$

where $a_w = 2kT\cdot h/g_m$, h being about 0.7, like in the junction field-effect transistors for MOS transistors with channel length of the order of some μm, and exceeding 1 for channel length in the submicrometre region [10].

The parallel noise in a MOS transistor, as long as it is employed in preamplifiers for high-energy experiments, can be neglected.

5'2. *Noise sources in detector and bias network.* – The detector, its own bias resistor when present and the preamplifier bias resistors R_G of fig. 5.1 contribute to the parallel noise source b_2 of fig. 3.1.

The detector can be connected to the preamplifier with either a.c. or d.c. coupling. The two biasing networks are shown in fig. 5.6, where the preamplifier, for the sake of reference, is assumed to employ a field-effect transistor.

The d.c. connection of fig. 5.6*b*) is used, in the case of the voltage-sensitive preamplifier, only provided that the detector leakage current is so small that the voltage drop it produces across R_G is negligible. Its analysis is, however, interesting to understand the difference in the noise behaviour between the connections *a*) and *b*).

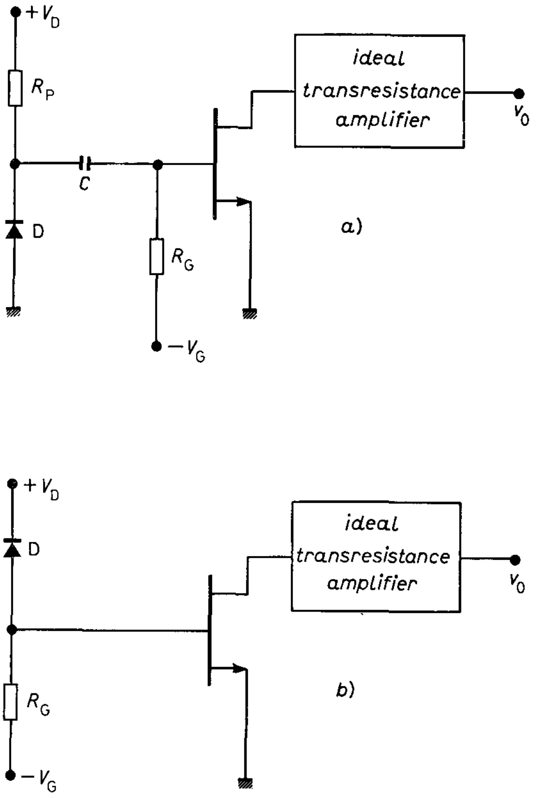

Fig. 5.6. – Connection between detector and preamplifier: *a*) a.c. coupling, *b*) d.c. coupling.

In both cases the detector contributes to the term b_2 in the spectral power density of the parallel source in fig. 3.1 with $\Sigma_{\text{det}} = qI_{\text{L}}$, describing the shot noise associated with the detector leakage current.

In the connection of fig. 5.6*a*) there are two sources of thermal noise, one associated with the detector bias resistor R_{P} and the other one associated with R_{G}. The resulting spectral power density of the equivalent parallel generator is

$$\Sigma_{\text{T}} = 2kT\left[\frac{1}{R_{\text{G}}} + \frac{1}{R_{\text{P}}}\right].$$

It can, therefore, be concluded that the parallel noise generator b_2 in the case of the a.c. coupled detector (fig. 5.6*a*)) has the following expression:

$$b_2 = qI_{\text{L}} + 2kT\left[\frac{1}{R_{\text{G}}} + \frac{1}{R_{\text{P}}}\right]. \tag{5.16}$$

It may be useful to point out, in passing, that the thermal noise modelled as a current source with bilateral power density $2kT/R$ can be attributed to an equivalent shot noise current source with spectral power density qI_{eq}, where $I_{\text{eq}} = (kT/q)(2/R)$. Conversely, shot noise can be attributed to an equivalent thermal source. In the case of fig. 5.6*b*), with the detector d.c. coupled to the preamplifier, only one source of thermal noise is present, that is, the one associated with R_{G}. Consequently

$$b_2 = qI_{\text{L}} + 2kT\frac{1}{R_{\text{G}}}\,. \tag{5.17}$$

Adding the b_2 terms of either (5.16) or (5.17) to the b_1 terms related, respectively, to the bipolar transistor, eq. (5.13), or to the field-effect transistor, eq. (5.1), the total spectral power density in the parallel noise generator of fig. 3.1 is found. Continuous monitoring of I_{L} during the experiment is advisable. In the spectral power density b of the parallel generator of fig. 3.1 the relative importance of b_1, contribution due to the parallel noise in the amplifying device, and b_2, contribution due to the detector and bias resistors, is subject to the following considerations. If the active device is a bipolar transistor, b_1 largely dominates. If, instead, the input device is a field-effect transistor and this is connected to a silicon detector operated at room temperature, then the parallel noise is determined by the detector leakage current and by the thermal noise in the bias resistors, $b = b_2$.

In the case of germanium bulk detector, which operates at cryogenic temperatures, the dominant contribution to parallel noise comes from the bias resistor R_{G} in the preamplifier. For such an application, indeed, preamplifiers with JFET input are utilized and d.c. coupling between detector and preamplifier is adopted.

Table 5.I summarizes the expressions of the spectral power densities a, b_1, b_2 for different combinations of detector type, bias network and active device.

TABLE 5.I.

	Type of input active device			
	Si JFET	Bipolar transitor	GaAs MESFET	MOS FET
$a(\omega)$	$2kT\dfrac{0.7}{g_{\text{m,F}}}$	$2kT\dfrac{0.5}{g_{\text{m,B}}} + R_{\text{BB}'}\dfrac{C_{\text{D}}^2}{(C_{\text{D}}+C_{\text{B}})^2}$	$2kT\dfrac{h}{g_{\text{m,F}}} + \dfrac{c_{\text{G}}}{\lvert\omega\rvert}$	$2kT\dfrac{h}{g_{\text{m}}} + \dfrac{c_{\text{M}}}{\lvert\omega\rvert}$
$b_1(\omega)$	qI_{G}	qI_{B}	qI_{G}	~ 0
	Type of detector and connection to the preamplifier			
	Si d.c. coupled	Si a.c. coupled	Ge d.c. coupled	Ge a.c. coupled
$b_2(\omega)$	$qI_{\text{L}} + \dfrac{2kT}{R_{\text{G}}}$	$qI_{\text{L}} + 2kT\left(\dfrac{1}{R_{\text{P}}} + \dfrac{1}{R_{\text{G}}}\right)$	$\sim 2kT\dfrac{1}{R_{\text{G}}}$	$\sim 2kT\left[\dfrac{1}{R_{\text{P}}} + \dfrac{1}{R_{\text{G}}}\right]$

Table 5.I enables the reader to determine the values of noise corner time constant achievable with the various possible detector-preamplifier combinations.

Recalling eq. (3.4) which can be written as

$$\tau_c = \sqrt{\frac{a_w}{b_1 + b_2}}\,(C_D + C_i)\,,$$

and the expressions of a_w, b_1, b_2 in table 5.I, it can be concluded that, for a fixed value of $C_D + C_i$, τ_c is limited by the base current noise in a bipolar transistor to a much smaller value than in the other devices. For instance, neglecting the terms b_2, τ_c would be of the order of $10^3(C_D + C_i)$ in a bipolar transistor and of the order of $10^6(C_D + C_i)$ in a junction field-effect transistor. The presence of the detector leakage current and of the thermal noise in the bias resistors may actually reduce the value of τ_c in the case of a junction field-effect transistor to much smaller values.

To understand qualitatively the effects of the noise sources in the active devices and their importance in the equivalent noise charge ENC at different processing times, the expression of ENC for the triangular shaper will be assumed as a reference [14]. Combining (4.8) and (4.27) the following result is obtained:

$$\text{ENC} = \left\{2\,\frac{a_w}{\tau_M}\,(C_D + C_i)^2 + 4\,\frac{\ln 2}{\pi}\,c(C_D + C_i)^2 + \frac{2}{3}\,(b_1 + b_a)\,\tau_M\right\}^{\frac{1}{2}}. \tag{5.18}$$

The equivalent noise charge is expressed as the square root of the quadratic sum of three partial contributions. The first one, determined by the white component in the power spectral density of the series generator, is inversely proportional to $\tau_M^{\frac{1}{2}}$.

The second one, due to the $1/|\omega|$ term in the power spectral density of the series generator, is independent of τ_M.

The third one, due to the parallel noise, is proportional to $\tau_M^{\frac{1}{2}}$. According to (5.18), the ENC has a minimum at $\tau_M = \sqrt{3}\tau_c$. The value of τ_M at which the minimum of ENC occurs is unaffected by the $1/|\omega|$-type noise.

The following interesting comments about the behaviour of the ENC as a function of τ_M can be made with reference to fig. 5.7 [14].

As shown in fig. 5.7, the bipolar transistor has an optimum ENC at a value of τ_M of a few tens of ns. The ENC for a junction field-effect transistor would be a continuously decreasing function of τ_M, represented by the linear behaviour in the double-logarithmic plot of fig. 5.7 if the noise from the detector and bias resistors were not present. A 10 nA detector leakage current shifts the value of τ_M at which the minimum of the ENC occurs to the 1 μs range.

The MOS transistor has an initial drop of the ENC as a function of τ_M, which reflects the behaviour of the white component a_w in the spectral power density

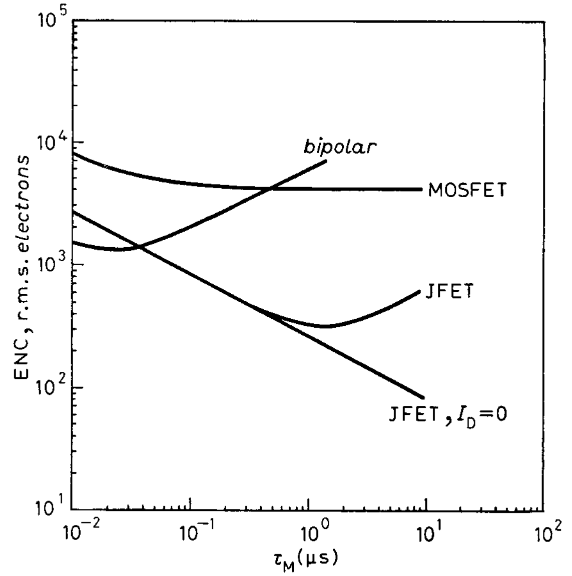

Fig. 5.7. - Equivalent noise charge as a function of τ_M for three types of active devices and a fixed value of C_D; $C_D = 30$ pF, $I_D = 10$ nA.

of the series noise source, followed by a settling to the value determined by the $c/|\omega|$ noise.

The curves of fig. 5.7 are theoretical curves obtained with typical values of the parameters of table 5.I.

In order to analyse the effect of series $c/|\omega|$ noise, the case of a MOS with $c = 10^{-10}\ \text{V}^2$ has been chosen.

The value of c would be considerably smaller in a Schottky-barrier field-effect transistor.

In the usual low-noise design, based upon discrete or thin- and thick-film circuit realizations, the choice of the input active device is restricted to bipolar or silicon junction field-effect transistors. GaAs field-effect transistors cover a domain of applications close to that of microwave bipolar transistors, that is, short processing times. In all these cases the contribution of the $c/|\omega|$ noise is either negligible or masked by the term introduced into the ENC by the series white spectral power density a_w.

REFERENCES

[1] A. VAN DER ZIEL: *Proc. IRE*, **50**, 1808 (1962).
[2] A. VAN DER ZIEL: *Proc. IRE*, **51**, 461 (1963).
[3] K. KANDIAH: *Low noise pulse amplifiers*, in *Instrumentation Techniques in Nuclear Pulse Analysis*, National Academy of Sciences, National Research Council, Publ. 1184 (1964), p. 65.

[4] V. Radeka: *Field-effect transistor in charge-sensitive amplifiers*, in *Instrumentation Techniques in Nuclear Pulse Analysis*, National Academy of Sciences, National Research Council, Publ. 1184 (1964), p. 70.
[5] V. Radeka: *IEEE Trans. Nucl. Sci.*, NS-**20**, 182 (1973).
[6] E. Gatti and P. F. Manfredi: *Nucl. Instrum. Methods Phys. Res.*, **226**, 142 (1984).
[7] A. Van Der Ziel: *Proc. IRE*, **46**, 1019 (1958).
[8] B. B. Fair: *IEEE Trans. Nucl. Sci.*, NS-**23**, 218 (1976).
[9] V. Radeka: *Nucl. Instrum. Methods Phys. Res.*, **226**, 175 (1984).
[10] K. Ogawa, B. Owen and H. J. Boll: *Bell Syst. Tech. J.*, **62**, 1181 (1983).
[11] G. Zimmer: *Nucl. Instrum. Methods Phys. Res.*, **226**, 175 (1984).
[12] B. J. Hosticka: *Nucl. Instrum. Methods Phys. Res.*, **226**, 185 (1984).
[13] G. Baccarani: *Physics of submicron devices*, in *Proceedings of the* NATO *Advanced Study Institute on « Large Scale Integrated Circuit Technology: State of the Art and Prospect »*, edited by L. Esaki and G. Soncini (1982), p. 647.
[14] P. F. Manfredi and F. Ragusa: *Nucl. Instrum. Methods Phys. Res. A*, **235**, 345 (1985).

6. – General considerations about shaping.

Some general considerations about shaping will now be made in order to outline the choice criteria that must be adopted in the design of a low-noise processor for high-energy experiments. The constraints that affect the value of the processing time will be discussed. The noise characteristics of some basic shapers are summarized in table 6.I. Each shaper is described by its « noise weighting function » which in the case of time-invariant circuits as well as in the case of time-variant ones with no preshaping before the gate coincides with the response to a detector current having the shape of a δ-impulse. Synthesis suggestions of the shapers, based upon the time-invariant or the time-variant approach, are also given. When either implementation is clearly not worthwhile compared to the other one, the corresponding space is left void.

The equivalent noise charge is given for all the shapers.

The values of τ_M that minimize the equivalent noise charge for every processor are also presented for all the processings with the exception of the truncated cusp for which, as is obvious, the ENC is a monotonically decreasing function of τ_M.

The last column of table 6.I gives the ratio between the equivalent noise charge evaluated for each processor at the optimum τ_M and the equivalent noise charge achievable with the indefinite cusp.

The analysis of the optimum ENC values, summarized for each processor in the last column of table 6.I, suggests the following useful comment. ENC_{opt} can be expressed as $\alpha\big(4a_w b_w (C_D + C_i)^2\big)^{\frac{1}{2}}$, where α is a coefficient larger than 1 which represents the « worsening factor » of the actual shaper compared with the one characterized by the indefinite-cusp weighting function. For a_w and

TABLE 6.I.

Shaping	Noise weighting function	Possible time-invariant implementation	Possible time-variant implementation
ideal infinite cusp	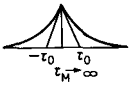	weighting network employing the principle of fig. 3.4	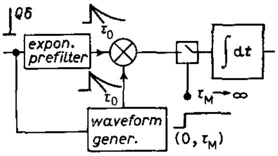
truncated cusp		weighting network employing the principle of fig. 3.4	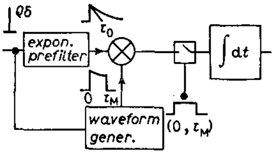
triangular	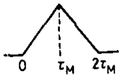	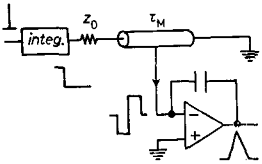	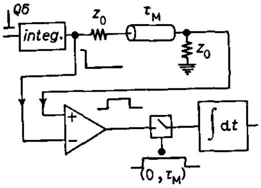
trapezoidal		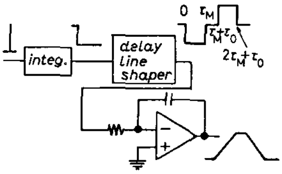	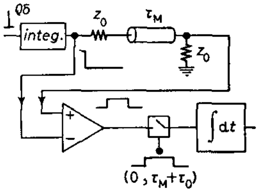
RC-CR $R_1C_1 = R_2C_2 = \tau_M$		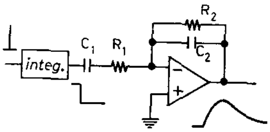	
piecewise parabolic	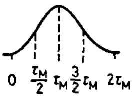		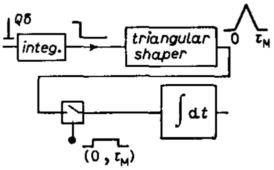
sinusoidal lobe	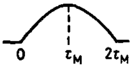		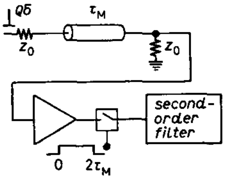

Equivalent noise charge r.m.s. coulomb	$\tau_{\mathrm{M,opt}}$	$\frac{\mathrm{ENC_{opt}}}{(4a_w b_w)^{\frac{1}{2}}(C_D + C_i)^{\frac{1}{2}}}$
$(4a_w b_w)^{\frac{1}{2}}(C_D + C_i)^{\frac{1}{2}}$	∞	1
$\frac{(4a_w b_w)^{\frac{1}{2}}(C_D + C_i)^{\frac{1}{2}}}{(1-\exp[-2(\tau_M/\tau_c)])^{\frac{1}{2}}}$	∞	1
$\left[2a_w(C_D + C_i)^2\frac{1}{\tau_M} + \frac{2}{3}b_w\tau_M\right]^{\frac{1}{2}}$	$\sqrt{3}\left(\frac{a_w}{b_w}\right)^{\frac{1}{2}}(C_D + C_i)$	1.07
$\left[2a_w(C_D + C_i)^2\frac{1}{\tau_M} + b_w\left(\frac{2}{3}\tau_M + \tau_0\right)\right]^{\frac{1}{2}}$	$\sqrt{3}\left(\frac{a_w}{b_w}\right)^{\frac{1}{2}}(C_D + C_i)$	$1.07\left[1 + 0.43\frac{\tau_0}{\tau_c}\right]^{\frac{1}{2}}$
$\frac{e}{2}\left[a_w(C_D + C_i)^2\frac{1}{\tau_M} + b_w\tau_M\right]^{\frac{1}{2}}$	$\left(\frac{a_w}{b_w}\right)^{\frac{1}{2}}(C_D + C_i) = \tau_c$	1.36
$\left[\frac{8}{3}a_w(C_D + C_i)^2\frac{1}{\tau_M} + \frac{14}{15}b_w\tau_M\right]^{\frac{1}{2}}$	$2\sqrt{\frac{5}{7}}\left(\frac{a_w}{b_w}\right)^{\frac{1}{2}}(C_D + C_i)$	1.25
$\left[\frac{\pi^2}{4}a_w(C_D + C_i)^2\frac{1}{\tau_M} + b_w\tau_M\right]^{\frac{1}{2}}$	$\frac{\pi}{2}\left(\frac{a_w}{b_w}\right)^{\frac{1}{2}}(C_D + C_i)$	1.25

b_w the expressions of table 5.I will be introduced. Assuming, for the sake of simplicity, that the input device is a field-effect transistor and writing a_w in the approximate form $a_w = kT/g_m$ and that the dominant contribution to b_w is the one determined by the detector leakage current, which is certainly true in the case of a room temperature Si detector, ENC_{opt} can be written, for a generic processor, as

$$\text{ENC}_{\text{opt}} = \alpha \left[\frac{4qkT}{\omega_T} \left((C_D/C_i)^{\frac{1}{2}} + (C_i/C_D)^{\frac{1}{2}} \right)^2 I_L C_D \right]^{\frac{1}{4}}$$

and

$$\tau_{M,\text{opt}} = \beta \left[\frac{kT}{q} \frac{1}{\omega_T} \left((C_D/C_i)^{\frac{1}{2}} + (C_i/C_D)^{\frac{1}{2}} \right)^2 (C_D/I_L) \right]^{\frac{1}{2}}.$$

The previous relationships show that the optimum ENC and corresponding τ_M can be expressed, apart from a constant, by the product of three factors. One depending on the gain-bandwidth product of the preamplifier input device, which is related to the device technology, the second on a « mismatch term » and the third on the detector characteristics.

The analysis of the various processors has been carried through by neglecting $1/\omega$ spectral power densities in the series generator $a(\omega)$, whose spectrum has been assumed to be white and labelled a_w.

Spectral power densities with linear ω dependence, typical of dielectric losses, have been neglected in the parallel generator, whose spectrum also has been assumed to be white and labelled b_w [1-3].

Both neglected kinds of noise, that is, series $1/\omega$ spectral density and parallel ω spectral density, would introduce into the expression of the ENC a term which is independent of τ_M and, therefore, the value of $\tau_{M,\text{opt}}$ is unaffected by this approximation.

As was already pointed out, the operating conditions of most experiments in high-energy physics are such that the noise due to dielectric losses is overwhelmed by the noise with a_w spectrum.

The same consideration applies very often also to the series $1/\omega$ noise. The exception is represented by the case in which a MOS transistor is employed as input device. The corresponding ENC has the τ_M dependence illustrated in fig. 5.7.

Table 6.I allows the evaluation of the considered processing systems once the weighting function is chosen, the characteristics of the input device are assigned and the detector parameters, capacitance and leakage current as well as the detector and preamplifier bias networks, are known.

A further important aspect is the choice of τ_M.

Strict considerations of signal-to-noise ratio would suggest for τ_M the value which minimizes the ENC according to table 6.I. It is worth emphasizing, however, that several other constraints affect the choice of τ_M.

Considerations related to counting rates and pile-up effects put an upper limitation to the usable τ_M.

The situation is largely different, depending on whether the detectors are employed in a fixed-target or in a collider experiment.

In several fixed-target experiments the detectors are subjected to very high counting rates, up to millions pulses per second during the accelerator spill. If a particle is detected at a given instant, the probability that other particles arrive within a time interval τ_S from the previous one is [4-6]

$$P = 1 - \exp[-\lambda\tau_S] , \tag{6.1}$$

λ being the average counting rate. If a detector current pulse is being processed and another pulse occurs within the processing time, then pile-up occurs. Depending on the characteristics of the shaper employed and on the mutual time separation, the amplitude measurement on the second event or on both of them may lead to a wrong result.

This means that the second event or both events have to be rejected to avoid pile-up inaccuracies. Let τ_D be the processing time, that is, the total time needed to process an event. The value of τ_D depends on the detector pulse duration and on the shaper. Let P_{SA} be the maximum tolerable pile-up probability. The processing time τ_D must be chosen so as to satisfy the following relationship:

$$\tau_D \leqslant \frac{1}{\lambda} \ln \frac{1}{1 - P_{SA}} . \tag{6.2}$$

For instance, a time-invariant triangular shaper with a base width $2\tau_M$ responds to a rectangular detector current of duration τ_{coll} with a signal of total duration $2\tau_M + \tau_{coll}$. This can be assumed to be the processing time of the system.

If a value of P_{SA} lower than 5 % is required at a counting rate of 10^6 pulses per second, then $2\tau_M + \tau_{coll}$ must not exceed 50 ns. In these circumstances, the upper limitation set to $2\tau_M + \tau_{coll}$ by the counting rate requirements becomes a mandatory one and, therefore, the signal-to-noise ratio must be optimized under this constraint on the processing time.

It has to be pointed out that in a segmented detector like a microstrip, where the counting rates on the individual strips are smaller than the counting rate λ on the whole detector, is still λ which determines the processing time. Otherwise it may occur that pulses corresponding to two different events in the detector overlap in time, thereby creating ambiguities in the assignment of the signal to the proper event [7].

In the existing colliders as well as in machines that will go into operation in a near future, the counting rate requirements are by far less severe. The time separation between bunch crossings is such that processing times in the μs region can be employed. In collider experiments the upper limitation to the processing time is determined by other constraints. For instance, by the detector leakage current. In other cases the upper limitation may come from the need of making real-time trigger decisions.

Other effects like ballistic error, signal induction on the noncollecting electrodes of a segmented detector and cross-talk contribute to important considerations in the choice of the shaper and of the processing time.

The nature of the ballistic error is shown in fig. 6.1 [8-10].

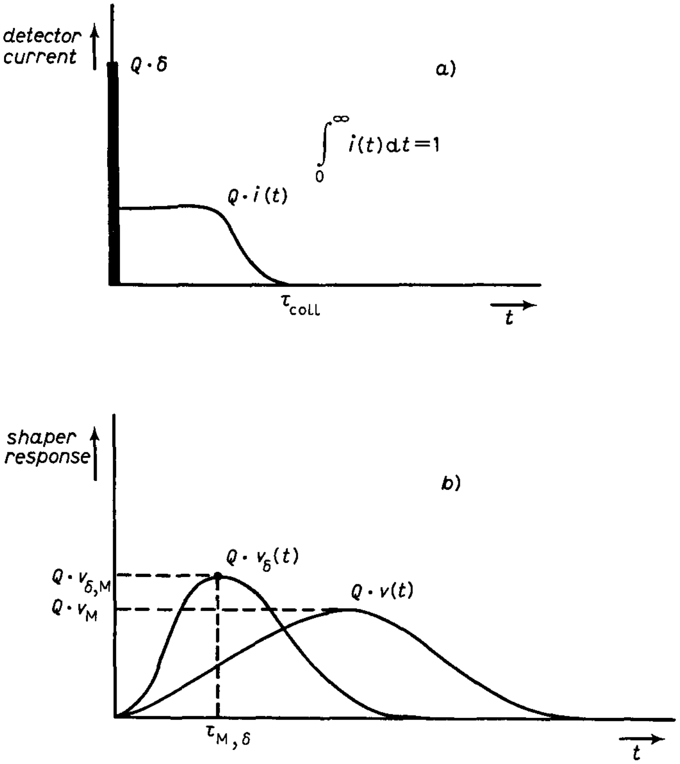

Fig. 6.1. – Response of the shaper to a δ-impulse-like detector current and to a pulse of finite duration: *a*) detector current shapes, *b*) shaped signals.

The processor assumed as a basis of this discussion responds to a δ-like detector current with the signal $Qv_\delta(t)$. A detector current of finite duration τ_{coll}, though carrying the same charge as the δ, excites at the processor output the response $Qv(t)$ which reaches its peak at a later time and has a smaller peak amplitude than $Qv_\delta(t)$.

The ballistic error is defined, according to fig. 6.1*b*), as

$$v_{\delta,M} - v_M\,. \tag{6.3}$$

The effect of ballistic error is limited to a reduction in the equivalent noise charge, related to the decreased output amplitude in the case of detector pulses having the same shape and duration.

If, however, the duration τ_{coll}, as frequently happens, is a random variable, then the ballistic effect contributes to increase the statistic uncertainty in the measurement of Q and, therefore, it has to be kept as small as possible [9, 10].

Analysis of the ballistic error was done by Baldinger and Franzen, who showed that the term (6.3) can be expressed as

$$v_{\delta,\text{M}} - v_\text{M} \simeq -\tfrac{1}{2}\tau_{\text{coll}}^2 v''_\delta(\tau_{\text{M}\delta}) \int_0^1 i(x)(\alpha_1 - x)^2\, \mathrm{d}x\,. \tag{6.4}$$

In the previous relationship $x = t/\tau_{\text{coll}}$ and α_1 is the centroid of the detector current pulse normalized to unit area

$$\alpha_1 = \int_0^1 x\, i(x)\, \mathrm{d}x\,.$$

As pointed out by (6.4), the ballistic error is proportional to the second derivative, that is, to the curvature of the δ-response $v_\delta(t)$ at the peak point. Therefore, a flat-topped $v_\delta(t)$ is required to reduce the ballistic error. A flat-topped $v_\delta(t)$ would eliminate the ballistic error for all the detector current pulses having a τ_{coll} shorter than the duration τ_0 of the flat region [10]. If τ_{coll} is a random variable with values ranging between 0 and τ_0, no amplitude fluctuation would be noticed in $v(t)$. For instance, trapezoidal shaping represents a good compromise between noise performances and insensitivity to collection time variations in the detector. Conversely, $v_\delta(t)$'s having an angular point at the instant

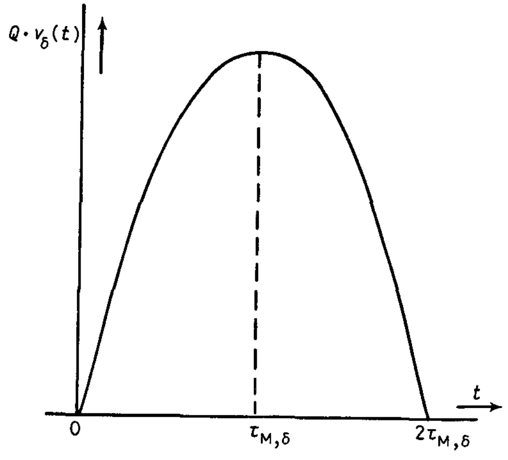

Fig. 6.2. – Parabolic δ-response for the evaluation of the ballistic error.

τ_M give large ballistic errors. This is the case of the cusp and the triangle. An example of evaluation of the ballistic error is made assuming, for reference, the parabolic $v_\delta(t)$ of fig. 6.2. The time dependence of $v_\delta(t)$ is $v_\delta(t) = 2t/\tau_{M,\delta} - t^2/\tau_{M,\delta}^2$ and has a maximum at $t = \tau_{M,\delta}$.

The relative ballistic error in the case of a rectangular current pulse of duration τ_{coll} is

$$\frac{v_{\delta,M} - v_M}{v_{\delta,M}} \simeq -\frac{1}{12}\left[\frac{\tau_{coll}}{\tau_{M,\delta}}\right]^2. \tag{6.5}$$

Equation (6.5) shows that, just using a round-topped $v_\delta(t)$ with a total base width equal to six times the detector pulse duration, the relative ballistic error is below 1%.

Absence of ballistic deficit can be thought of as the property of insensitivity of a measurable output parameter to the shape of the input charge pulse. In particular, insensitivity to zero-charge spurious bipolar input pulses. This kind of disturbances occurs in segmented detectors like microstrips and Ge bulk detectors [11-15].

Two origins of such disturbances are explained with reference to fig. 6.3. Induction of electron and hole pairs on output electrodes not collecting charge carriers like, for instance, $K+1$ in fig. 6.3*a*). Taking into account the weighting field for electrode $K+1$ introduced in sect. **2** and the trajectory of both carriers of a pair, it is apparent that a bipolar, zero-area pulse is induced on $K+1$. This pulse has an overall length equal to the transit time of the slower carrier.

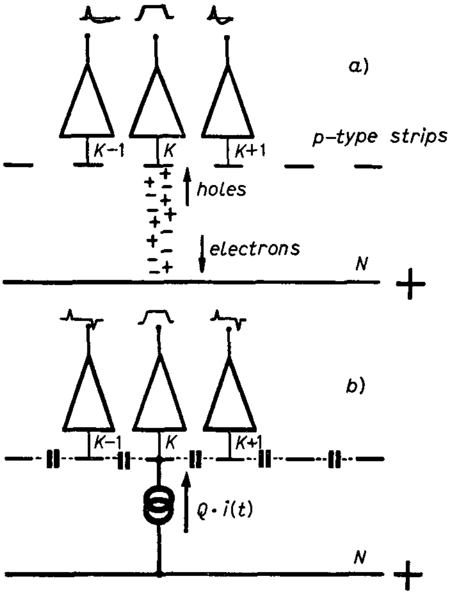

Fig. 6.3. – Induction (*a*)) and cross-talk (*b*)) on the noncollecting electrodes. The preamplifiers are supposed to be current-sensitive.

Cross-talk is illustrated in fig. 6.3*b*). If the input impedance of the preamplifier connected to strip K, though small, is finite, a signal appears across it. The capacitive coupling between strip K and strips $K-1$, $K+1$ is responsible for the injection of two signals, proportional to the derivative of the one appearing on the strip K, into the contiguous preamplifiers. Again, cross-talk signals have zero net area and their time separation is determined by the duration of the pulse at strip K.

Cancellation of induction and cross-talk signals requires round-topped or, better, flat-topped pulses $v_\delta(t)$ of suitable duration.

The phenomena that set a lower limit to the duration of $v_\delta(t)$, namely ballistic error, induction and cross-talk on the noncollecting electrodes, combined with the pile-up effect which conversely sets an upper limitation to the processing time, may lead to incompatible requirements for the duration of $v_\delta(t)$. This incompatibility can be sometimes removed only by reducing, in fixed-target experiments, the counting rate λ.

REFERENCES

[1] A. VAN DER ZIEL: *Adv. Electron. Electron Phys.*, **49**, 225 (1979).

[2] V. RADEKA: *State of the art of low noise amplifiers for semiconductor radiation detectors*, in *Proceedings of the International Symposium on Nuclear Electronics, Versailles 1968*, Vol. **1** (1968), p. 1.

[3] J. LLACER: *Accurate measurements of noise parameters in ultra-low noise opto-feedback spectrometer systems*, in *Proceedings of the II* ISPRA *Nuclear Electronics Symposium*, Publ. EUR 5370e (1975), p. 47.

[4] R. L. CHASE: *Nuclear Pulse Spectrometry* (McGraw-Hill Book Co., New York, N. Y., 1963), Chapt. 9.

[5] P. W. NICHOLSON: *Nuclear Electronics* (J. Wiley and Sons, London, 1973).

[6] I. DE LOTTO, P. F. MANFREDI and P. PRINCIPI: Part I, *Energ. Nucl.* (*Milan*), **11**, 557 (1964); Part II, **11**, 599 (1964).

[7] E. GATTI and P. F. MANFREDI: *Nucl. Instrum. Methods Phys. Res.*, **226**, 142 (1984).

[8] E. BALDINGER and W. FRANZEN: *Adv. Electron. Electron Phys.*, **8**, 225 (1956).

[9] V. RADEKA: *IEEE Trans. Nucl. Sci.*, NS-**19**, 412 (1972).

[10] F. S. GOULDING: *Nucl. Instrum. Methods*, **100**, 493 (1972).

[11] J. P. RICHER and R. L. CHASE: *IEEE Trans. Nucl. Sci.*, NS-**31**, 258 (1984).

[12] V. RADEKA: *Position sensitive semiconductor detectors, signal formation, noise and position readout*; *Silicon detectors for high energy physics*, in *Proceedings of a Workshop Held at Fermilab, October 15-16, 1981*, edited by T. FERBEL (1981), p. 21.

[13] P. F. MANFREDI and V. RAGUSA: *Nucl. Instrum. Methods Phys. Res. A*, **235**, 345 (1985).

[14] E. GATTI and V. RADEKA: *IEEE Trans. Nucl. Sci.*, NS-**25**, 676 (1978).

[15] D. BUCHOLZ, R. KLANNER, G. LUTZ, H. J. SEEBRUNNER, A. WYLIE, U. KÖTZ, K. U. PÖSNECKER and J. KEMMER: *Nucl. Instrum. Methods Phys. Res. A*, **253**, 481 (1985).

7. – Capacitive matching between detector and preamplifier.

The forthcoming considerations apply only to the contribution to the ENC due to either thermal noise in the channel of field-effect devices or to the shot noise in the collector current of a bipolar transistor. According to table 6.I such a contribution is given by

$$\text{ENC}_a^2 = 2kT\,\frac{\chi}{g_\text{m}}\,(C_\text{D}+C_\text{i})^2\,\frac{h_1}{\tau_\text{M}}\,, \tag{7.1}$$

where h_1 is a numerical parameter characteristic of the shaper employed (4.16), and a coefficient χ, $0.5 < \chi < 0.7$, has been introduced to describe with a single expression both bipolar and field-effect devices. As already pointed out, the g_m/C_i ratio represents the gain-bandwidth product ω_T of the device employed. Equation (7.1) can, therefore, be written

$$\text{ENC}_a^2 = 2kT\,\frac{\chi}{\omega_\text{T}}\,\frac{(C_\text{D}+C_\text{i})^2}{C_\text{i}}\,\frac{h_1}{\tau_\text{M}} = 2kT\,\frac{\chi}{\omega_\text{T}}\,\frac{h_1}{\tau_\text{M}}\left[\left(\frac{C_\text{D}}{C_\text{i}}\right)^{\frac{1}{2}} + \left(\frac{C_\text{D}}{C_\text{i}}\right)^{-\frac{1}{2}}\right]^2 C_\text{D}\,. \tag{7.2}$$

The gain-bandwidth product ω_T has an important significance in the application of the device to low-noise amplification of signals from capacitive sources [1].

The device charge sensitivity can be defined as

$$\frac{\text{d}I_\text{u}}{\text{d}Q_\text{i}} = \frac{\text{d}I_\text{u}}{\text{d}V_\text{i}}\,\frac{\text{d}V_\text{i}}{\text{d}Q_\text{i}}\,, \tag{7.3}$$

where $\text{d}I_\text{u}$ is the output current change corresponding to the amount of charge $\text{d}Q_\text{i}$ deposited on the input capacitance C_i and V_i is the voltage across C_i.

As, by definition,

$$g_\text{m} = \frac{\text{d}I_\text{u}}{\text{d}V_\text{i}}\,, \qquad C_\text{i} = \frac{\text{d}Q_\text{i}}{\text{d}V_\text{i}}\,,$$

eq. (7.3) shows that the charge sensitivity of the employed device is expressed by its gain-bandwidth product ω_T. It can be supposed now that both g_m and C_i can be linearly controlled in such a way that their ratio, that is, the gain-bandwitdh product, remains constant [2-4].

For instance, such a control can be achieved by paralleling n subdevices with transconductance g_mo and input capacitance C_io. In this case

$$g_\text{m} = n g_\text{mo}\,, \qquad C_\text{i} = n C_\text{io}$$

and the ratio g_m/C_i is equal to g_mo/C_io, that is, to the gain-bandwidth product of the subdevice.

Another way of controlling g_m and C_i is based upon the control of the cross-section of the device.

In bipolar transistors, within the range of values of the collector current I_C, where the gain-bandwidth product is independent of I_C and the junction capacitance negligible, so that C_i can be assumed to be determined by the diffusion term alone, g_m and C_i are, within a good approximation, linear functions of I_C. The values of g_m and C_i can, therefore, be controlled through I_C.

Whatever is the method utilized to control g_m and C_i, it can be seen from (7.2) that the equivalent noise charge attains a minimum when C_i is made equal to C_D, that is, when the preamplifier is capacitively matched to the source [3-8]. The value of such a minimum is

$$\text{ENC}_{a\text{CM}} = \left[8kT\,\frac{\chi}{\omega_T}\,\frac{h_1}{\tau_M}\,C_D\right]^{\frac{1}{2}}. \tag{7.4}$$

According to (7.4) the equivalent noise charge in the condition of capacitive matching is proportional to the square root of the detector capacitance and inversely proportional to the square root of the $\omega_T\tau_M$ product.

The condition of capacitive matching becomes very important at large detector capacitances [8, 9]. The equivalent noise charge in the mismatched condition, $C_i \neq C_D$, can be written as

$$\text{ENC}_a = \text{ENC}_{a\text{CM}}\,\frac{1+m}{2m^{\frac{1}{2}}}, \tag{7.5}$$

where $m = C_i/C_D$. In the highly mismatched case, $m \ll 1$, eq. (7.5) becomes

$$\text{ENC}_a \sim \text{ENC}_{a\text{CM}}\,\frac{1}{2m^{\frac{1}{2}}}. \tag{7.6}$$

To give an example, the case of a detector capacitance of 1000 pF and of a field-effect transistor with $C_i = 10$ pF will be considered. The condition of capacitive matching, implemented by paralleling devices, would require 100 FET's. This, of course, would be hardly feasible. As pointed out by (7.6), however, the ENC depends on the square root of m. This means that, while a single field-effect transistor would give ENC $\sim$ 5 ENC_{CM}, two paralleled devices would give ENC $\sim$ 3.5 ENC_{CM} and four would lead to ENC $\sim$ 2.5 ENC_{CM}. So a considerable improvement is achieved by reducing the mismatch from $C_i/C_D = 10^{-2}$ to $C_i/C_D = 4\cdot 10^{-2}$ with a reasonable number of devices in parallel. Going up with m, as pointed out by (7.5), the ENC becomes less and less sensitive to further paralleling of devices, until the feasibility of the method is impaired by the large number of devices required.

At short values of τ_M, such that the contribution of the parallel noise to the total ENC is negligible with respect to the contribution due to the collector shot noise, capacitive matching can be realized more easily with bipolar transistors.

To achieve capacitive matching, two parameters are available. They are the input capacitance, which can be controlled through the collector current, and the number of devices which can be connected in parallel. By fixing in each transistor a relatively large current, but not too large in order to avoid possible ω_T drops due to high injection effects, the capacitive matching can be achieved with a smaller number of devices than in the case of field-effect transistors.

A different approach to the capacitive matching between detector and preamplifier is based upon the use of a transformer between them (fig. 7.1).

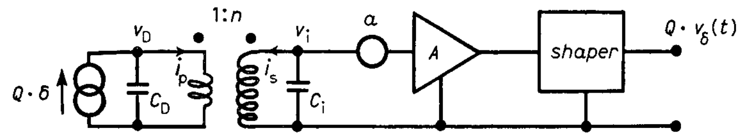

Fig. 7.1. – Capacitive matching based upon transformer coupling between detector and preamplifier; $v_i = nv_D$, $i_p = -ni_s$.

The contribution given by the white component a in the series generator to the total equivalent noise charge referred to the input of the processor 7.1 is

$$\text{ENC}_a^2 = 2kT\,\frac{\chi}{g_{mo}}\,\frac{(C_D + n^2 C_{io})^2}{n^2}\,\frac{h_1}{\tau_M} = 2kT\,\frac{\chi}{\omega_T}\,\frac{h_1}{\tau_M}\left(\frac{1}{n}\sqrt{\frac{C_D}{C_{io}}} + n\sqrt{\frac{C_{io}}{C_D}}\right)^2 C_D\,. \tag{7.7}$$

The contribution ENC_a^2 presents a minimum, as a function of n^2, for $n^2 = C_D/C_{io}$, that is, when the condition of capacitive matching is met. Introducing the gain-bandwidth product $\omega_T = g_{mo}/C_{io}$ into (7.7), it is easily recognized that $\text{ENC}_{a,\text{CM}}$, that is, the equivalent noise charge in the situation of capacitive matching, has again the expression (7.4).

The transformer-based approach to capacitive matching has some limitations. A real transformer would add to the total ENC a noise contribution connected with magnetic losses in the core. The finite magnetizing inductance would seriously spoil the signal-to-noise ratio unless bipolar shaping is employed. Besides, transformer coupling would be unsuitable if the preamplifiers have to be located in a strong magnetic field. Exhaustive analysis of the domains of application of transformers and of their intrinsic limitations is available in the literature [8, 10, 11].

Both ways of realizing the capacitive matching between detector and preamplifier reviewed so far aim at achieving an adequately high charge transfer from the detector to the preamplifier. It has to be pointed out, in passing, that the capacitive-matching condition corresponds to the best transfer of the energy available at the source to the capacitance C_i connected in parallel to C_D.

With reference to fig. 7.2, the energy stored on C_i is

$$\frac{1}{2} C_i V_i^2 = \frac{1}{2} C_i \frac{Q^2}{(C_D + C_i)^2} = \frac{Q^2}{2C_D} \frac{C_i/C_D}{(1 + C_i/C_D)^2}.$$

This expression attains a maximum for $C_i = C_D$.

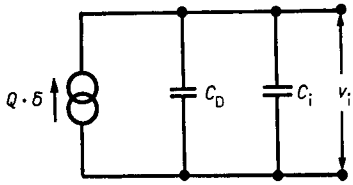

Fig. 7.2. - Energy transfer to C_i.

Capacitive matching can be employed also to reduce the contribution to the ENC arising from the $1/|\omega|$ component of the spectral power density in the series generator. Such a feature is important in the application of MOS transistors to amplification of signals from capacitive sources [5].

The problem of improving the charge transfer between detector and preamplifiers can be tackled also in other ways that can be considered either alternative or complementary to the ones discussed so far.

For instance, charge swinging between detector and preamplifier separated by a decoupling inductor has already been proven to be feasible and to give a nonnegligible reduction in the equivalent noise charge.

All the previous considerations, though important in any situation, will become of utmost importance in the applications of silicon calorimetry, where detector capacitances of some nF are foreseen.

REFERENCES

[1] V. Radeka: *IEEE Trans. Nucl. Sci.*, NS-**20**, 182 (1973).

[2] P. Rehak: *Detection and signal processing in high-energy physics*, in *Proc. S.I.F.*, Course LXXXIV (1981), *Data Acquisition in High-Energy Physics*, edited by G. Bologna and M. L. Vincelli (North-Holland Publ. Co., Amsterdam, 1983), p. 25.

[3] E. Gatti, A. Hrisoho and P. F. Manfredi: *IEEE Trans. Nucl. Sci.*, NS-**30**, 319 (1983).

[4] V. Radeka: *Position-sensitive semiconductor detectors-Signal formation, noise and position readout*, in *Silicon Detectors for High Energy Physics, Proceedings of a Workshop held at Fermilab, October 15-16, 1981*, edited by T. Ferbel (1981), p. 21.

[5] V. Radeka: *Nucl. Instrum. Methods Phys. Res.*, **226**, 209 (1984).

[6] P. F. Manfredi: *Solid state telescopes for lifetime measurements*, in *Proceedings of the Conference on the Search for Charm, Beauty and Truth at High Energies*, edited by G. Bellini and S. C. C. Ting (Plenum Press, New York, N. Y., 1984), p. 257.

[7] C. Bussolati, S. Cova and E. Gatti: *Z. Angew. Math. Phys.*, **22**, 14 (1971).

[8] V. Radeka: *Summary of noise relations for liquid argon ion chamber. Calorimeter notes*, Brookhaven National Laboratory, 9-1973 (1973).

[9] P. F. Manfredi and F. Ragusa: *Nucl. Instrum. Methods Phys. Res. A*, **235**, 345 (1985).

[10] E. Gatti, P. F. Manfredi and D. Marioli: *Nucl. Instrum. Methods Phys. Res.*, **193**, 539 (1982).

[11] R. L. Chase, C. Gruhn, A. Hrisoho, C. Valette and G. Waysand: *Fast electronics for a metastable superconducting detector*, in *Proceedings of the II* ISPRA *Nuclear Electronics Symposium*, Publ. EUR 5370e (1975), p. 29.

8. – Bipolar and junction field-effect transistors in elementary preamplifier configurations.

8'1. *Preamplifiers employing a single active device.* – Some elementary preamplifier configurations employing bipolar transistors and junction field-effect transistors will be discussed here. They are the common-emitter connection of fig. 8.1*a*), the common-base connection of fig. 8.1*b*) and the common-source connection of fig. 8.1*c*) [1-5].

The three elementary preamplifiers of fig. 8.1 are followed by three different shapers, labelled, respectively, I, II, III, designed in such a way that the three circuits respond to a δ-impulse detector current with the same output signal $Qv_\delta(t)$. To evaluate the equivalent noise charge, the active devices will be represented with the circuit models of fig. 5.2, 5.4.

The shapers of fig. 8.1 will be again considered to be noiseless and presenting to the collector of the transistor or to the drain of the JFET an ideal, current-sensitive input. The total input capacitance of the bipolar transistor will be assumed to be equal to C_B and that of the JFET to be $C_\text{i} = C_\text{GS} + C_\text{GD}$. The time domain approach of subsect. 4'2.2 will be employed for noise calculations and the measuring time τ_M of the shaper will be adopted as a reference variable, by putting in (4.16) $u = t/\tau_\text{M}$. The following parameters will be introduced:

$$h_1 = \int_{-\infty}^{\infty} [v'_\delta(u)]^2 \,\mathrm{d}u \,, \tag{8.1}$$

$$h_2 = \int_{-\infty}^{\infty} [v_\delta(u)]^2 \,\mathrm{d}u \,. \tag{8.2}$$

For the sake of simplicity, the index o used in the previous section to label the input capacitance and the transconductance of the individual devices will be omitted.

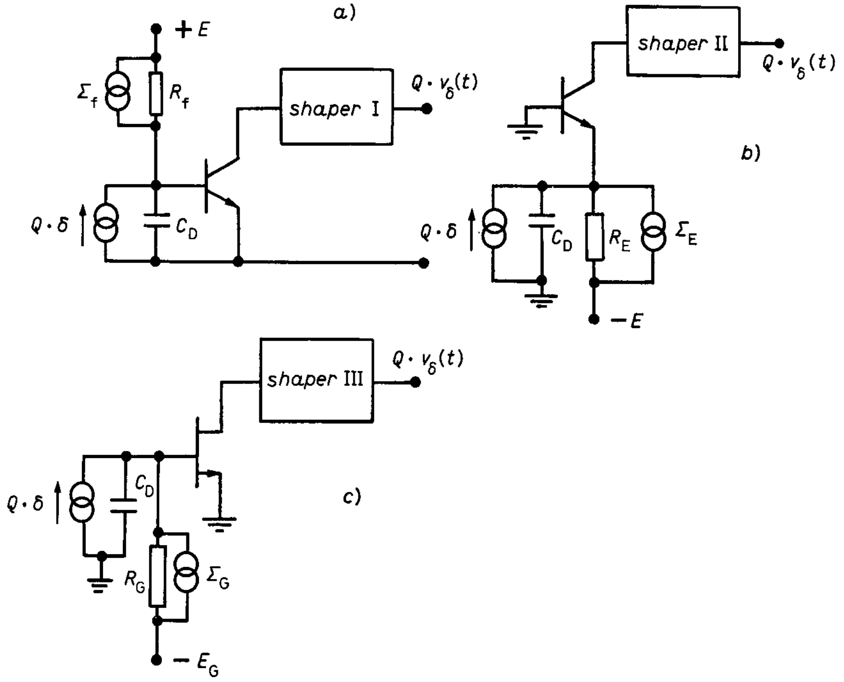

Fig. 8.1. – Elementary preamplifier configuration employing bipolar and junction field-effect transistors: *a*) common emitter, *b*) common base, *c*) common source.

The three bias resistors R_f, R_E, R_G are of negligible importance from the point of view of signal shaping, while their contribution to the noise may be of some significance.

For this reason, they will be considered to be infinitely large in the evaluation of the transfer functions, while their thermal-noise contribution will be accounted for by the relevant current sources with spectral densities

$$\Sigma_{R_f} = \frac{2kT}{R_f}, \qquad \Sigma_{R_E} = \frac{2kT}{R_E}, \qquad \Sigma_{R_G} = \frac{2kT}{R_G}. \tag{8.3}$$

A similar consideration allows to short circuit $R_{BB'}$ in the model of fig. 5.4, yet accounting for its thermal-noise contribution with the ideal series voltage source with spectral power density $\Sigma_{BB'}$ [6, 7].

By carrying through the calculations, the following expressions are obtained for the equivalent noise charge referred to the input of the circuits of fig. 8.1:

a) Common-emitter amplifier

$$\text{ENC} = \left\{kT\left[\left(C_D\frac{(1+\gamma)^2}{\gamma}\frac{1}{\omega_\alpha} + 2R_{BB'}C_D^2\right)\frac{h_1}{\tau_M} + \left(\frac{\omega_\alpha}{\beta}\frac{C_D}{\gamma} + \frac{2}{R_f}\right)h_2\tau_M\right]\right\}^{\frac{1}{2}} \tag{8.4}$$

r.m.s. coulomb.

b) Common-base amplifier

$$(8.5)\qquad \mathrm{ENC}=\left\{kT\left[\left(C_{\mathrm{D}}\frac{(1+\gamma)^2}{\gamma}\,\frac{1}{\omega_\alpha}+2R_{\mathrm{BB'}}\,C_{\mathrm{D}}^2\right)\frac{h_1}{\tau_{\mathrm{M}}}+\left(\frac{\omega_\alpha}{\beta}\,\frac{C_{\mathrm{D}}}{\gamma}+\frac{2}{R_{\mathrm{E}}}\right)h_2\tau_{\mathrm{M}}\right]\right\}^{\frac{1}{2}}$$

r.m.s. coulomb .

In these relationships $\beta = I_{\mathrm{C}}/I_{\mathrm{B}}$ is the transistor current gain, and $\omega_\alpha = g_{\mathrm{m,B}}/C_{\mathrm{B}}$ is the alpha–cut-off angular frequency of the device.

c) Common-source amplifier

$$(8.6)\qquad \mathrm{ENC}=\left[2kT\cdot 0.7\,C_{\mathrm{D}}\,\frac{(1+\gamma)^2}{\gamma}\,\frac{1}{\omega_{\mathrm{T}}}\,\frac{h_1}{\tau_{\mathrm{M}}}+\left(qI_{\mathrm{G}}+\frac{2kT}{R_{\mathrm{G}}}\right)h_2\tau\right]^{\frac{1}{2}}$$

r.m.s. coulomb .

In eqs. (8.4), (8.5), $\gamma = C_{\mathrm{D}}/C_{\mathrm{B}}$ and in eq. (8.6) $\gamma = C_{\mathrm{D}}/C_{\mathrm{i}}$ represent the detector capacitance normalized to the device input capacitance.

Comparison between (8.4) and (8.5) leads to the following comments. The equivalent noise charge for the common-base and the common-emitter connections differs only for the noise due to the bias resistors R_t, R_{E}. Usually R_t is much larger than R_{E} and, therefore, the common-emitter configuration has a slightly smaller ENC.

The equivalent noise charge of a bipolar transistor has two terms in the bracket which multiplies the coefficient $kT(h_1/\tau_{\mathrm{M}})$.

One, determined by the shot noise in the collector current can be expressed as $(C_{\mathrm{D}}+C_{\mathrm{B}})^2/g_{\mathrm{m}}$. The other one, determined by the thermal noise in the base spreading resistance is $2R_{\mathrm{BB'}}C_{\mathrm{D}}^2$. At values of C_{D} much larger than C_{B}, both terms are proportional to C_{D}^2. If the collector current is raised beyond 1 mA, the dominant term becomes the one related with the base spreading resistance.

Instead, at values of C_{D} smaller than C_{B}, the noise contribution due to the base spreading resistance can be neglected [5].

In the absence of noise due to the external bias network (8.4) and (8.5) become equal. The ENC as a function of γ presents a minimum for

$$(8.7)\qquad \gamma=\left[1+\frac{h_2}{h_1}\,\frac{\omega_\alpha^2\tau_{\mathrm{M}}^2}{\beta}\right]^{\frac{1}{2}}.$$

If τ_{M} is so short that $\omega_\alpha^2\tau_{\mathrm{M}}^2 \ll \beta(h_1/h_2)$, the minimum ENC occurs for $\gamma = 1$, that is, in the condition of capacitive matching between detector and transistor input capacitance [4, 8].

The behaviour of the ENC as a function of γ^{-1} is illustrated in fig. 8.2. Each set of curves is drawn for a fixed value of $\omega_\alpha\tau_{\mathrm{M}}$ and with the normalized base speading resistance $\varrho_{\mathrm{BB'}} = R_{\mathrm{BB'}}\,\omega_\alpha\,C_{\mathrm{D}}$ as a parameter.

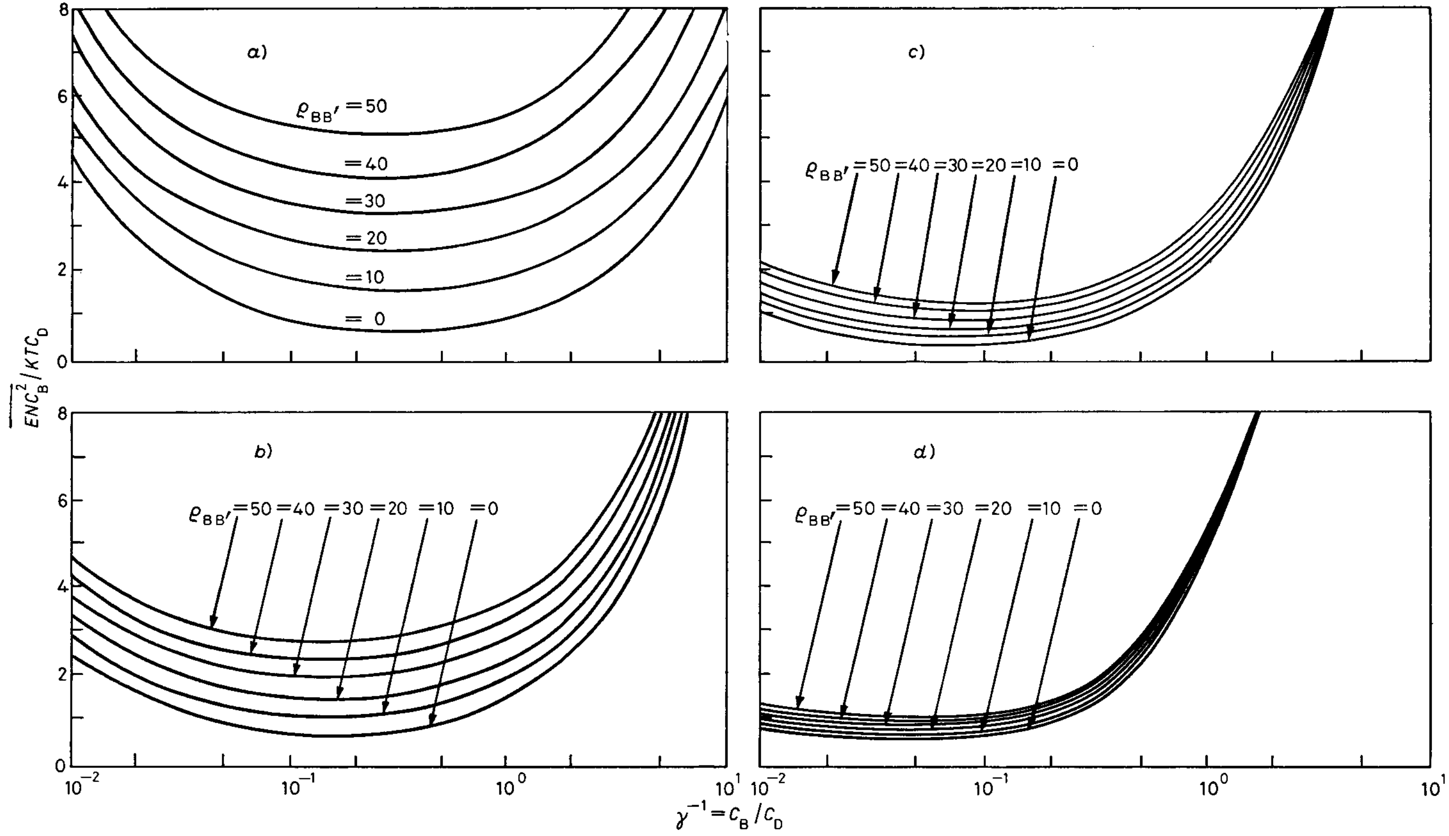

Fig. 8.2. – Normalized square of the equivalent noise charge as a function of γ^{-1} for a bipolar transistor, $\beta = 100$: *a*) $\tau_M = 60/\omega_\alpha$, *b*) $\tau_M = 120/\omega_\alpha$, *c*) $\tau_M = 240/\omega_\alpha$, *d*) $\tau_M = 480/\omega_\alpha$.

The curves of fig. 8.2 clearly show that the value of γ at which the minimum ENC occurs moves away considerably from $\gamma = 1$ as $\omega_\alpha \tau_M$ is increased due to the effect of parallel noise.

For a given C_D and for assigned values of β, ω_α, τ_M, the value of C_B which gives the best ENC can be easily fixed by adjusting the collector standing current.

Comparison between the expected behaviour and some values of the ENC measured at different γ's is shown in fig. 8.3.

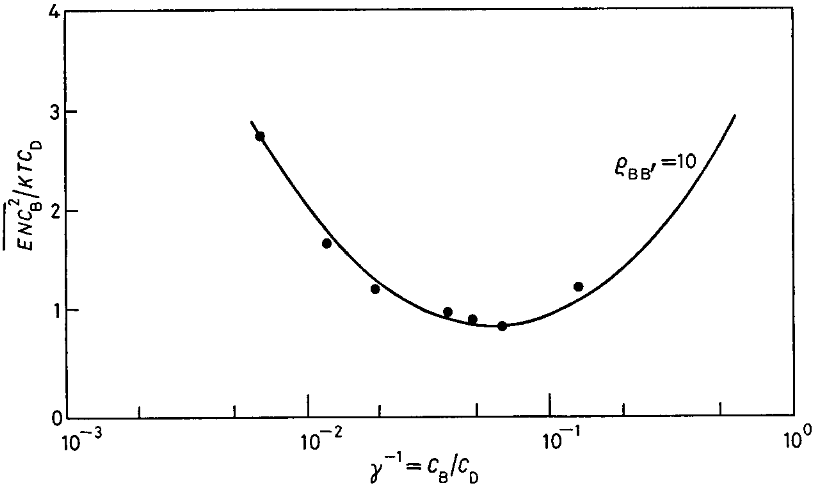

Fig. 8.3. – Comparison between the theoretical behaviour (——) of the ENC as a function of γ^{-1} and some experimental points (•); $\beta = 50$, $C_D = 100$ pF, $\tau_M = 180/\omega_\alpha$.

In the case of a field-effect transistor, as pointed out by eq. (8.3), the value of γ which makes the ENC minimum is $\gamma = 1$. This condition of capacitive matching, however, cannot be met as C_D is varied, by using a single field-effect transistor. A way of controlling C_i in a broad range of values through an electrical parameter does not exist in a field-effect transistor.

8'2. *Preamplifiers employing parallel connections of bipolar and junction field-effect devices.* – As pointed out in the previous subsection, the minimum of ENC as a function of γ can, in principle, be achieved in a bipolar transistor by adjusting the collector current as C_D is varied. The minimum ENC in the case of field-effect transistors occurs when the capacitive matching is satisfied and this requires, as discussed in sect. **7**, the parallel connection of the devices. Also in the case of bipolar transistors, however, the parallel connection has a beneficial effect, that of reducing the noise contribution due to $R_{BB'}$. This effect is demonstrated in fig. 8.4. The curve *a*) of fig. 8.4 shows the dependence of the ENC on the detector capacitance for a single bipolar transistor working at 1 mA collector current.

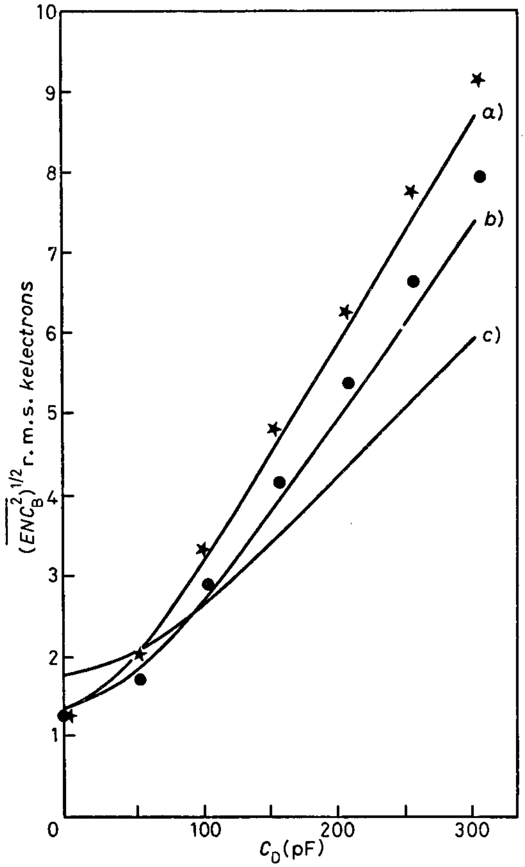

Fig. 8.4. – Reduction of the noise contribution due to $R_{BB'}$ achieved by paralleling two bipolar transistors: ——— experimental curves; theoretical values: * case *a*), • case *b*), $R_{BB'} = 15\ \Omega$, $\beta = 10^2$, $\omega_\alpha = 2\pi \cdot 10^9$ rad/s.

The curve *b*) shows the same dependence for the parallel connection of two transistors, working at 0.5 mA each.

Comparison between curves *a*) and *b*) confirms that the value of the ENC at $C_D = 0$ is unchanged, on account of the fact that the total base current and, therefore, the parallel noise are unaltered, while the sensitivity of the ENC to the detector capacitance is reduced.

Such a reduction results from the decreased noise contribution from $R_{BB'}$, achieved by paralleling two transistors. Curve *c*) refers to two transistors in parallel, each working at a 1 mA collector current.

This situation brings about an increase in the parallel noise and, therefore, a larger ENC at $C_D = 0$ and a further reduction in the sensitivity of the ENC to C_D, which accounts for the reduced contribution of the collector shot noise.

Next, the question arises of finding, for given values of C_D and τ_M and fixed h_1 and h_2, the parallel combination of bipolar transistors which gives the minimum ENC. Two possibilities exist. One consists in fixing the number n_{F} of transistors to be paralleled and determining accordingly the value of C_{BO} in the individual transistors which gives the minimum ENC.

The other one consists in fixing the standing current in the individual transistors and in finding out the number n of devices that have to be paralleled to achieve the minimum ENC. The former approach, fixed number, gives for $\gamma_{\min}$ and $\mathrm{ENC}_{\min}$ the following values:

$$\gamma_{\min} = n_{\mathrm{f}}\left[1 + \frac{\omega_\alpha^2\,\tau_{\mathrm{M}}^2}{\beta}\,\frac{h_2}{h_1}\right]^{\frac{1}{2}}, \tag{8.8}$$

$$\mathrm{ENC}_{\mathrm{B,min}} = 2kTC_{\mathrm{D}}\,\frac{h_1}{\omega_\alpha\,\tau_{\mathrm{M}}}\left\{\sqrt{1 + \frac{\omega_\alpha^2\,\tau_{\mathrm{M}}^2}{\beta}\,\frac{h_2}{h_1}} + 1 + \frac{R_{\mathrm{BB'}}}{n_{\mathrm{f}}}\,\omega_\alpha\,C_{\mathrm{D}}\right\}. \tag{8.9}$$

The approach based upon a fixed working point in the individual transistors, that is, C_{BO} assigned, gives for the number of devices $n_{\min}$ which minimizes the ENC and for $\mathrm{ENC}_{\min}$, respectively,

$$n_{\min} = \frac{C_{\mathrm{D}}}{C_{\mathrm{BO}}}\left[\frac{1 + 2\omega_\alpha R_{\mathrm{BB'}}\,C_{\mathrm{B}}}{1 + (h_2/h_1)(\omega_\alpha^2\,\tau_{\mathrm{M}}^2/\beta)}\right]^{\frac{1}{2}} \tag{8.10}$$

and

$$\mathrm{ENC}_{\mathrm{B,min}} = 2kTC_{\mathrm{D}}\,\frac{h_1}{\omega_\alpha\,\tau_{\mathrm{M}}}\left\{1 + \sqrt{\left(1 + \frac{\omega_\alpha^2\,\tau_{\mathrm{M}}^2}{\beta}\,\frac{h_2}{h_1}\right)\left(1 + 2R_{\mathrm{BB'}}\,C_{\mathrm{D}}\,\omega_\alpha\,\frac{C_{\mathrm{B}}}{C_{\mathrm{D}}}\right)}\right\}. \tag{8.11}$$

For the field-effect transistor the minimum ENC is achieved for $\gamma = 1$. As in most of high-energy applications τ_{M} is short enough to make the parallel noise contribution negligible, the equivalent noise charge $\mathrm{ENC}_{\mathrm{F,min}}$ can be expressed as

$$\mathrm{ENC}_{\mathrm{F,min}} = \left\{8kT\cdot 0.7\,C_{\mathrm{D}}\,\frac{h_1}{\omega_{\mathrm{T}}\,\tau_{\mathrm{M}}}\right\}^{\frac{1}{2}}. \tag{8.12}$$

8'3. *Comparison between input stages employing bipolar and junction field-effect transistors.* – The analysis of subsect. **8'1** and **8'2** opens up the possibility of comparing different configurations of bipolar and field-effect input stages, determining in the $(C_{\mathrm{D}}, \tau_{\mathrm{M}})$-plane the regions where either component gives better noise performances [4]. The present discussion will be carried on in connection to the piecewise parabolic shaper whose parameters h_1 and h_2 have the following values:

$$h_1 = \frac{8}{3}, \quad h_2 = \frac{14}{15}.$$

It will be assumed that the devices employed in the input stages are a bipolar transistor with a 1 GHz f_α and a junction field-effect transistor with $g_m = 10$ mA/V and $C_i = 10$ pF, featuring accordingly a 10^9 rad/s ω_T.

As a first case, comparison will be made between a bipolar transistor whose working point is adjusted at each value of C_D so as to satisfy (8.7) and the parallel combination of JFETs which at every C_D ensures the capacitive matching. The boundary curves that in the (C_D, τ_M)-plane limit the regions where the former input stage has smaller or larger ENC than the latter one are shown in fig. 8.5. The current gain β is assumed as a parameter. It is shown in fig. 8.5

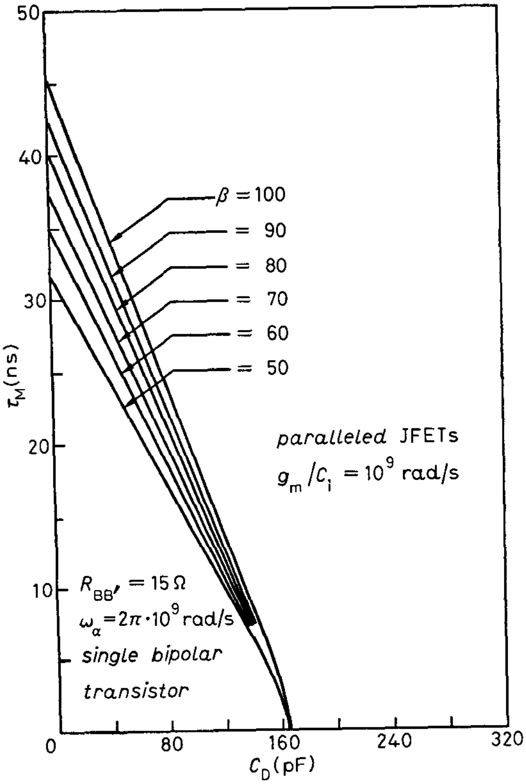

Fig. 8.5. – Boundary curves in the (C_D, τ_M)-plane separating the regions where a single bipolar transistor gives a smaller or a larger ENC than the parallel combination of JFETs required for capacitive matching.

that, at any τ_M, a value of C_D can be found beyond which the bipolar stage becomes more noisy than the JFET one. This can be explained by the remark that, according to the equivalent circuit of fig. 5.4, as C_D increases, the fraction of the noise generator $\Sigma_{BB'}$ which appears at the B'E port increases.

As a second step, the parallel combination of n_{min} transistors, where n_{min}

is the number which, according to (8.10), minimizes ENC_B in the operation at fixed C_{BO}, can be compared to the parallel combination of JFETs required for capacitive matching. The new boundary curves in the (C_D, τ_M)-plane are horizontal straight lines. That is, for a given β of the bipolar transistor, the bipolar stage is superior, regardless of the value of C_D up to a certain τ_M beyond which the FET stage takes over (fig. 8.6). The parallel combination of JFETs required

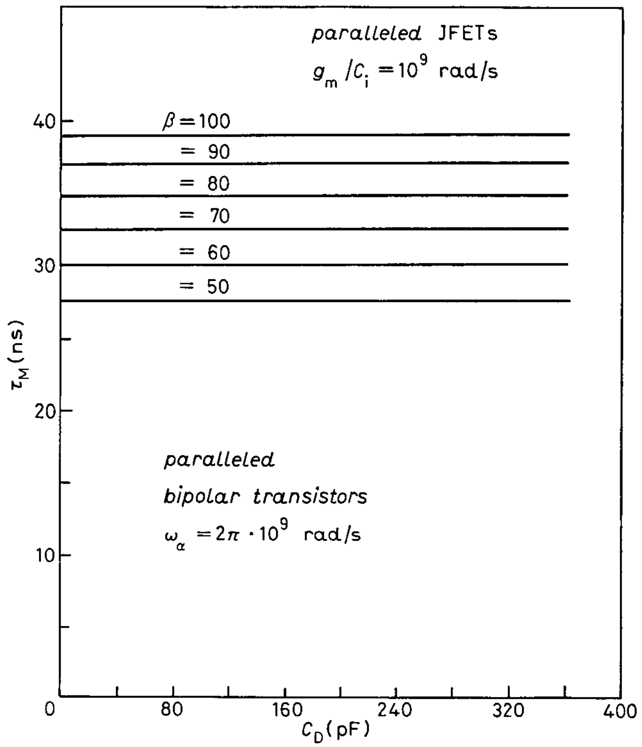

Fig. 8.6. – Boundary curves separating in the (C_D, τ_M)-plane the regions where the parallel combination of the optimum number of bipolar transistors, each working at a fixed C_B, features a smaller or a larger ENC than the parallel combination of JFETs required for capacitive matching.

for capacitive matching may be unpractical, especially if the number of preamplifiers is large. It makes, therefore, sense to compare input stages consisting of a single device of either type. In this case the advantage of the bipolar transistor, which allows an optimization of the ENC based upon the simple control of its working point, emerges. This is confirmed by the boundary curves of fig. 8.7. As shown in fig. 8.7, the region where the bipolar stage features a smaller ENC than the JFET one is considerably broader than in the previous cases. In particular, the larger is C_D, the wider is the range of values of τ_M where the

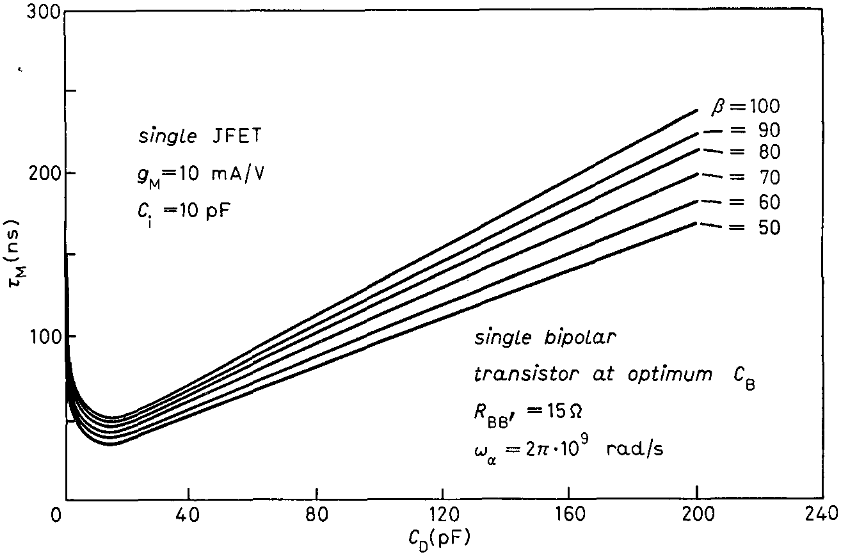

Fig. 8.7. – Boundary curves separating the regions where a single bipolar transistor put to work in the optimum condition (8.7) features a smaller or a larger ENC than a single JFET.

bipolar transistor has a better noise behaviour. This property of the bipolar transistor was successfully exploited in the early days of application of the silicon telescopes in high-energy experiments [1].

REFERENCES

[1] P. F. Manfredi, D. Misler and V. Varoli: *Limitations in the performances of silicon detectors used as live targets in high energy experiments*, in *Proceedings of the Topical Seminar on Interactions of Elementary Particles with Nuclei*, edited by G. P. Bellini and G. Bertocchi (Trieste, 1970), p. 275.

[2] A. Hrisoho and K. Truong: *IEEE Trans. Nucl. Sci.*, NS-**27**, 329 (1980).

[3] A. Hrisoho: *Silicon detector electronics for high energy experiments*, in *Proceedings of the Conference on the Search for Charm, Beauty and Truth at High Energies, Erice, November 1981*, edited by G. Bellini and S. C. C. Ting (Plenum Press, New York, N. Y., 1984), p. 457.

[4] E. Gatti, A. Hrisoho and P. F. Manfredi: *IEEE Trans. Nucl. Sci.*, NS-**30**, 319 (1983).

[5] E. Gatti and P. F. Manfredi: *Nucl. Instrum. Methods Phys. Res.*, **226**, 142 (1984).

[6] H. F. Knott, H. Sutcliffe and C. Eng: *Proc. IEE*, **120**, 623 (1973).

[7] A. Willemsen and N. Bell: *IEE J. Solid-State Circuits*, SC-**15**, 245 (1980).

[8] H. Spieler and E. E. Haller: *IEEE Trans. Nucl. Sci.*, NS-**32**, 419 (1985).

9. – Feedback preamplifier structures.

9'1. *Block diagram analysis.* – With the only exception of the grounded-base connection, which is sometimes employed alone and has as attractive features a short risetime and a good transmission stability, all the other configurations are rather intended as input stages of feedback loops.

Under hypotheses of broad validity, the expressions of the ENC as well as the results of the comparative discussions made on stages consisting of one or more paralleled devices can be extended to the case in which the reviewed configurations are employed as input stages of feedback preamplifiers. It is sufficient for this to assume that i) the second-stage noise is negligible and ii) the feedback loop around the preamplifier does not change the signal transfer function from the detector to the shaper output as well as the noise weighting function, except for a constant factor. This statement has been implicitly already checked in subsect. **8'1**, when it has been observed that the common-emitter and the common-base configurations, assuming the noise from the external bias resistors negligible, have the same ENC.

The present section is devoted to feedback preamplifier structures employing more active elements in the loop [1].

The basic configurations that will be discussed are shown in fig. 9.1 along with the input-to-output transfer functions evaluated in the simplified hypothesis of infinite gain in the amplifying modules. They are, respectively, a charge-sensitive configuration (a)), a current-sensitive configuration (b)) and a voltage-sensitive one (c)) [2-6].

To a better approximation, the three amplifying blocks of fig. 9.1 will be represented with a single-pole transfer function

$$T(s) = \frac{g_{\mathrm{m,T}} R}{1 + sRC}, \tag{9.1}$$

where $g_{\mathrm{m,T}}$ is the total transconductance of the block and the parallel of R and C is the internal load across which the current $g_{\mathrm{m,T}} v_{\mathrm{i}}$ flows, thereby producing the voltage gain. In general $g_{\mathrm{m,T}}$ may be greater than the transconductance of the input stage, for a current gain may exist between input stage and R, C load. Only when such a current gain is unity, $g_{\mathrm{m,T}} = g_{\mathrm{m}}$. The gain-bandwidth product of the amplifying block is $g_{\mathrm{m,T}}/C$ and this is usually smaller than the ω_{T} of the devices employed in the input stage.

The input capacitance of the amplifying blocks with the main feedback open is labelled C_{i} in fig. 9.1.

9'1.1. Charge-sensitive configuration. The charge-sensitive configuration of fig. 9.1 has an advantage over the other ones, that is, the noise

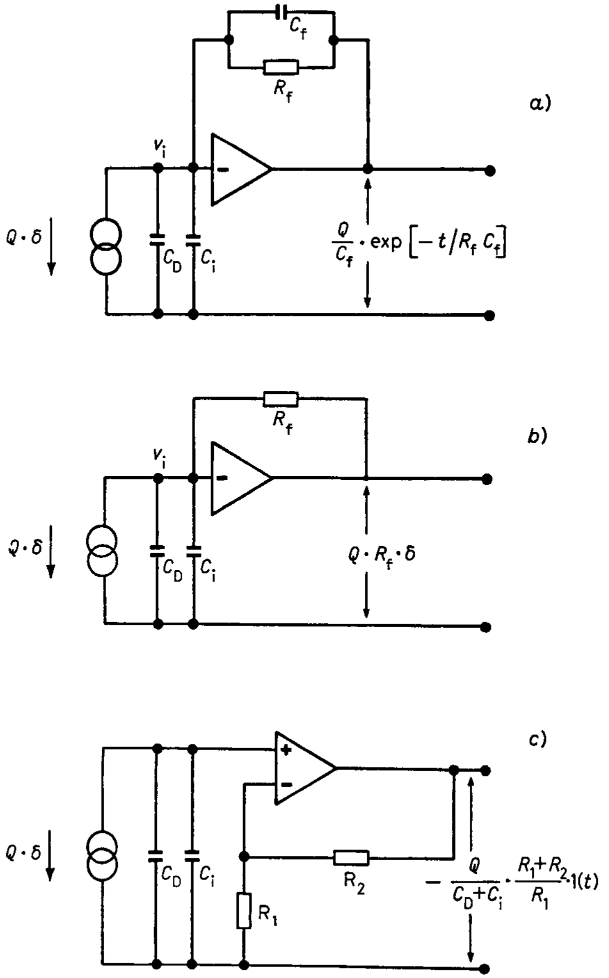

Fig. 9.1. – Feedback preamplifier configurations: *a*) charge sensitive, *b*) current sensitive, *c*) voltage sensitive.

contribution from the external network can be made negligible. The feedback resistor R_f serves the only purpose of providing a d.c. return for the bias currents of the input device. It can be made as large as $10^9\ \Omega$ in the case of a field-effect transistor input and of the order of $10^5\ \Omega$ or more with a bipolar input stage. Throughout the range of values of τ_M either device is intended to cope with, the contribution to the ENC arising from the thermal noise in R_f is usually of minor importance.

Evaluation of the impedance Z_i presented by the charge-sensitive loop in parallel to the $C_D + C_i$ capacitance shows the following interesting property. If the internal time constant RC is made equal to $R_f C_f$, the magnitude $|Z_i|$ has the frequency dependence shown in fig. 9.2. The d.c. gain $g_{m,T} R$ is assumed $\gg 1$. From fig. 9.2, it can be concluded that $Z_i = C/g_{m,T} C_f$ from d.c. up to a

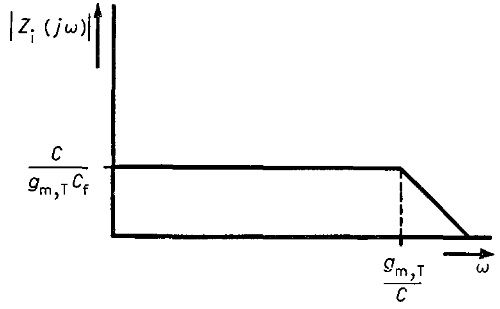

Fig. 9.2. – Frequency dependence of the magnitude of Z_i for a charge-sensitive loop.

frequency determined by the gain-bandwith product of the amplifying block [1, 2].

Such a resistive term, which depends only on the total transconductance $g_{m,T}$ and on the ratio of two capacitors, under certain conditions can be less noisy than a physical resistor of the same value. For this reason it deserves the denomination of « cold resistor » [2-4].

The values of the cold resistor can be varied within a broad range by a suitable choice of $g_{m,T}$, C_f, C.

Small values of the cold resistor are required in segmented detectors in order to reduce the time constants with which the spurious cross-talk signals appearing on the electrodes next to the collecting one die off.

The evaluation of the transfer functions in the charge-sensitive loop can be done on the basis of the equivalent circuit of fig. 9.3 which puts the cold resistor into evidence.

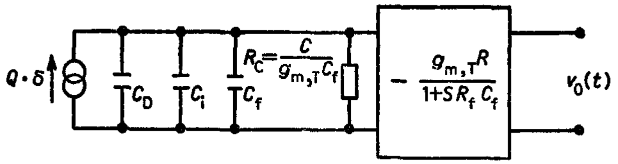

Fig. 9.3. – Equivalent circuit of the charge-sensitive loop with the cold resistance into evidence.

The amplifying block of fig. 9.3 is represented by the transfer function $-g_{m,T}R/(1+sR_fC_f)$, in which the cancellation condition $RC=R_fC_f$ has been employed.

Usually $R_fC_f \gg (C_D+C_i+C_f)(C/g_{m,T}C_f)$ and, therefore, the risetime of the output signal $v_0(t)$ in response to the δ-impulse detector current is determined by the input time constant,

$$\tau_i=(C_D+C_i+C_f)\frac{C}{g_{m,T}C_f}\,. \tag{9.2}$$

As pointed out by (9.2), the preamplifier risetime depends on the total capacitance shunting the preamplifier input port and on the cold resistance. Equation (9.2) can be, alternatively, written as

$$\tau_i = \frac{1}{g_{m,T}/C} \frac{1}{C_f/(C_D + C_i + C_f)}, \tag{9.3}$$

which expresses τ_i as the reciprocal of the gain-bandwidth product of the amplifying block divided by the feedback return ratio. As pointed out by (9.2), in order to keep the preamplifier risetime small at large detector capacitance, the cold resistance has to be adequately reduced, which can be done by increasing C_f if the gain-bandwidth product of the amplifying block is assumed to be constant.

The signal at the output of a charge-sensitive preamplifier has usually a very large decay time constant, according to the need of keeping R_f large to reduce its thermal-noise contribution. In order to clip this signal, without introducing undesired negative tails, pole-zero cancellation is performed, as shown in fig. 9.4.

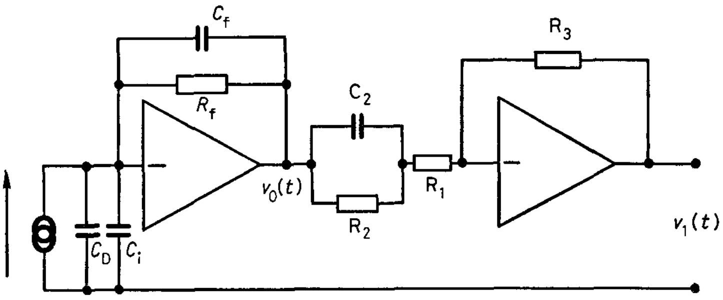

Fig. 9.4. – Signal clipping by pole-zero cancellation at the output of the charge-sensitive loop.

The foregoing analysis deals with the slow exponential decay at the output of the charge-sensitive loop and, therefore, the risetime portion of $v_0(t)$ can be neglected, by writing

$$V_0(s) = \frac{Q}{sC_f} \frac{s}{s + 1/R_f C_i}. \tag{9.5}$$

The voltage $v_1(t)$ can be expressed in the Laplace domain as

$$\begin{aligned} V_1(s) &= -V_0(s) \frac{R_3}{R_1} \frac{s + 1/R_2 C_2}{s + (R_1 + R_2)/(R_1 R_2)(1/C_2)} = \\ &= -\frac{R_3}{R_1} \frac{s + 1/R_2 C_2}{s + \big((R_1 + R_2)/R_1 R_2\big)(1/C_2)} \frac{Q}{sC_f} \frac{s}{s + 1/R_f C_f}. \end{aligned} \tag{9.6}$$

If the zero $s = -1/R_2C_2$ in eq. (9.6) is chosen so as to cancel the pole $s = -1/R_f C_f$, the previous relationship becomes

$$V_1(s) = -\frac{Q}{sC_f}\frac{R_3}{R_1}\frac{1}{s+\big((R_1+R_2)/R_1R_2\big)(1/C_2)}, \tag{9.7}$$

which shows that the original signal $v_0(t)$ has undergone clipping to the reduced time constant $(R_1R_2/(R_1+R_2))C_2$ and amplification determined by the R_3/R_1 ratio.

If R_1 is made equal to zero, eq. (9.6) yields

$$V_1(s) = -V_0(s)R_3C_2\left(s+\frac{1}{R_2C_2}\right) = -Q\frac{C_2}{C_f}R_3\frac{s+1/R_2C_2}{s+1/R_fC_f}. \tag{9.8}$$

If the condition of pole-zero cancellation $R_2C_2 = R_fC_f$ is met again, (9.8) becomes

$$V_1(s) = -Q\frac{C_2}{C_f}R_3 . \tag{9.9}$$

In this case the input-to-output relationship is a real transresistance $-(C_2/C_f)R_3$. Within the intrinsic band width limitations of the amplifying blocks, the configuration 9.4 preserves the detector current shape.

It can be concluded that a charge-sensitive loop followed by a pole-zero cancellation with $R_1 = 0$ implements a current-sensitive configuration. Such a configuration has better noise performances than the one employing resistive feedback, shown in fig. 9.1*b*).

9'1.2. Current-sensitive configuration. The current-sensitive configuration of fig. 9.1*b*) presents, besides the noise sources in the preamplifier module, the thermal-noise contribution from the feedback resistor R_f. This resistor cannot be made too large, otherwise the pole determined by R_f and the stray capacitance across it would spoil the closed-loop risetime.

The frequency dependence of the magnitude of the input impedance Z_i presented by the current-sensitive preamplifier in parallel to $C_D + C_i$ is shown in fig. 9.5. In the frequency range of interest the input impedance has an inductive character. This may result into an oscillating response at certain values of the detector capacitance. At very small detector capacitance the circuit is not critical, but its input impedance can be not as small as desired. The advantage of the resistive feedback preamplifier over the other ones is that, in all the applications requiring that the detector current shape be preserved, no pole-zero cancellation is needed. Such an advantage becomes important in connection with detectors involving large numbers of acquisition channels, like microstrip planes [7, 8]. Individual pole-zero cancellation on thousands of preamplifiers would hardly be feasible.

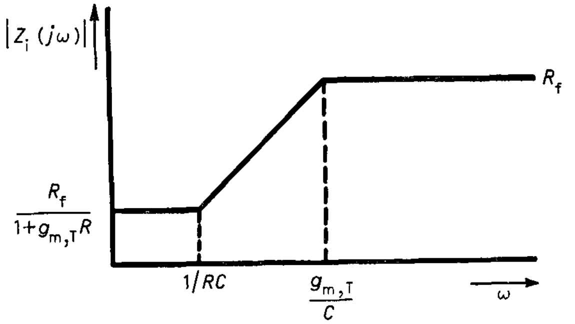

Fig. 9.5. – Frequency dependence of the magnitude of the input impedance in the current-sensitive configuration.

9·1.3. Voltage-sensitive configuration. In the voltage-sensitive configuration of fig. 9.1c) the external feedback network adds a contribution to the white spectral density in the series noise generator. Such a contribution, in the practical case in which $R_2 \gg R_1$, is equal to $2kTR_1$. By choosing R_1 and R_2 suitably small, that is, $R_1 \sim 1\ \Omega$, the effect of the external bias network on the preamplifier noise becomes negligible.

The voltage-sensitive configuration presents to the detector an impedance of purely capacitive nature. Such a capacitance has been labelled C'_i in fig. 9.1c) to emphasize the fact that C'_i, by virtue of the series voltage feedback, is smaller than the «cold capacitance» of the active devices.

In the configuration 9.1c) the relationship between the charge delivered by the detector and the output voltage depends on the detector capacitance. If, however, the detector is totally depleted and the radiation damage effects during the experiment are negligible, C_D can be considered stable and reliable enough to guarantee an adequate accuracy in the measurement of Q.

The voltage-sensitive preamplifier has two interesting features. First, its risetime is independent of the detector capacitance and, therefore, the preamplifier can be fast enough even at very large C_D's.

Second, contrary to what happens with the charge-sensitive and current-sensitive configurations, the voltage-sensitive preamplifier does not load the detector appreciably. It becomes, therefore, very suitable to sense the total voltage across stacks of series-connected detectors. This feature has been exploited to perform multiplicity measurements with telescopes of silicon detectors.

9·2. *Basic low-noise inverting amplifier.* – Some examples of low-noise preamplifier design, able to cope with different experimental situations in elementary-particle physics, will be described in this subsection. Before going into the analysis of the specific circuits, a rather general circuit diagram of low-noise inverting amplifier will be illustrated. This circuit, shown in fig. 9.6, provides a basic building block around which charge-sensitive loops of the type shown in fig. 9.1*a*) or current-sensitive configurations of fig. 9.1*b*) can be realized.

For reference purposes, the input device of the low-noise inverting amplifier has been represented as a field-effect transistor, but the structure of fig. 9.6 applies equally well to the case of a bipolar-transistor input stage, as well as to any parallel combinations of bipolar or field-effect devices.

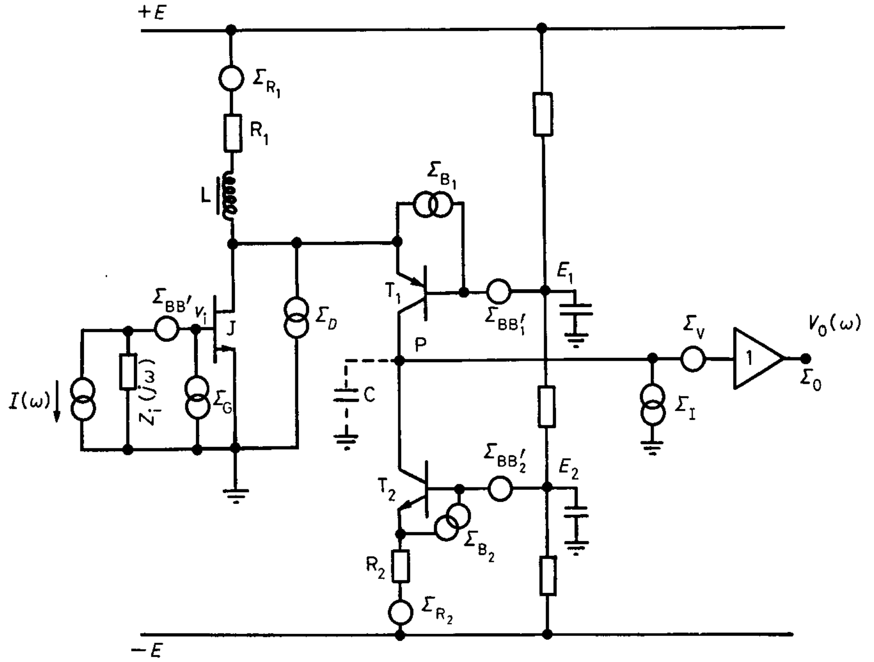

Fig. 9.6. – Basic configuration of low-noise inverting amplifier.

According to the circuit diagram of fig. 9.6 J behaves as a transconductance amplifier which injects a signal current $g_m v_i$ into the emitter of the common-base transistor T_1. The collector of T_1 is connected to that of T_2, which acts as a current source. It is reasonable to assume that the load appearing between P and ground is purely capacitive, so that the open-loop transfer function of the low-noise preamplifier is $-g_m/sC$, where C is the total capacitance shunting P.

The noise sources in the circuit are represented by their spectral power densities. They have the following meaning:

1) $\Sigma_{BB'}$ is the spectral power density of the generator which accounts for the thermal noise in the base spreading resistor of a bipolar transistor if employed as input device in 9.6.

2) Σ_G is the spectral power density of the parallel noise related to the input bias current, $\Sigma_G = qI_G$ or $\Sigma_G = qI_B$ according to whether the input device is a field-effect or a bipolar transistor.

3) Σ_{D} is the spectral power density of the thermal noise in the channel of a JFET or the power density of the shot noise in the collector current of a bipolar transistor, $\Sigma_{\mathrm{D}} = 2kT\cdot 0.7\, g_{\mathrm{m}}$ or $\Sigma_{\mathrm{D}} = qI_{\mathrm{C}}$, respectively.

4) Σ_{R_1}, Σ_{R_2} are the spectral power densities of the thermal noise in the resistors R_1, R_2, $\Sigma_{\mathrm{R}_1} = 2kTR_1$, $\Sigma_{\mathrm{R}_2} = 2kTR_2$.

5) Σ_{B_1}, Σ_{B_2} are the spectral power densities of the shot noise in the base currents of T_1 and T_2,

$$\Sigma_{\mathrm{B}_1} = qI_{\mathrm{B}_1}\,, \qquad \Sigma_{\mathrm{B}_2} = qI_{\mathrm{B}_2}\,.$$

6) $\Sigma_{\mathrm{BB}_1'}$, $\Sigma_{\mathrm{BB}_2'}$ are the spectral power densities of the thermal noise in the base spreading resistors of T_1 and T_2.

7) Σ_{I} and Σ_{V} are the parallel and series spectral power densities of the output stage.

For the sake of comparing the relative importance of the various noise sources and their relation to the signal, open-loop analysis of the circuit 9.6 is adequate.

In the circuit of fig. 9.6 the contribution of the shot noise in the collector currents of the common-base transistors T_1, T_2 to the output spectral power density Σ_0 is small compared to the contribution due to the base current noise of the same transistors. For this reason, the generators that would represent the shot noise in the collector currents of T_1 and T_2 have been omitted.

The inductor L has the purpose of reducing, in the frequency range of interest, the contribution to Σ_0 due to Σ_{R_1} and $\Sigma_{\mathrm{BB}_1'}$. A high quality is required for this component, which must feature very low stray capacitance, must be able to work at relatively large currents without core saturation and must have an inductance between 10 and 100 mH.

The inductor L is present in most low-noise preamplifiers for nuclear spectroscopy. In high-density preamplifiers for applications in high-energy experiments it may be too bulky, expensive and even not usable if the preamplifiers are located in a strong magnetic field.

For these reasons the total output spectral density of the noise, Σ_0, will be evaluated in the absence of L, with the understanding that, if L is present, its effect can be accounted for by putting $\Sigma_{\mathrm{R}_1} = 0$, $\Sigma_{\mathrm{BB}_1'} = 0$.

The output spectral power density is given by

$$\Sigma_0(\omega) \simeq \left\{\Sigma_{\mathrm{G}}|Z_{\mathrm{i}}(\omega)|^2 g_{\mathrm{m}}^2 + \Sigma_{\mathrm{BB}'} g_{\mathrm{m}}^2 + \Sigma_{\mathrm{D}} + \frac{\Sigma_{\mathrm{R}_1}}{R_1^2} + \frac{\Sigma_{\mathrm{BB}_1'}}{R_1^2} + \right. \\ \left. + \Sigma_{\mathrm{B}_1} + \frac{\Sigma_{\mathrm{R}_2}}{R_2^2} + \frac{\Sigma_{\mathrm{BB}_2'}}{R_2^2} + \Sigma_{\mathrm{B}_2} + \Sigma_{\mathrm{I}}\right\} \frac{1}{\omega^2 C^2} + \Sigma_{\mathrm{V}}\,. \tag{9.10}$$

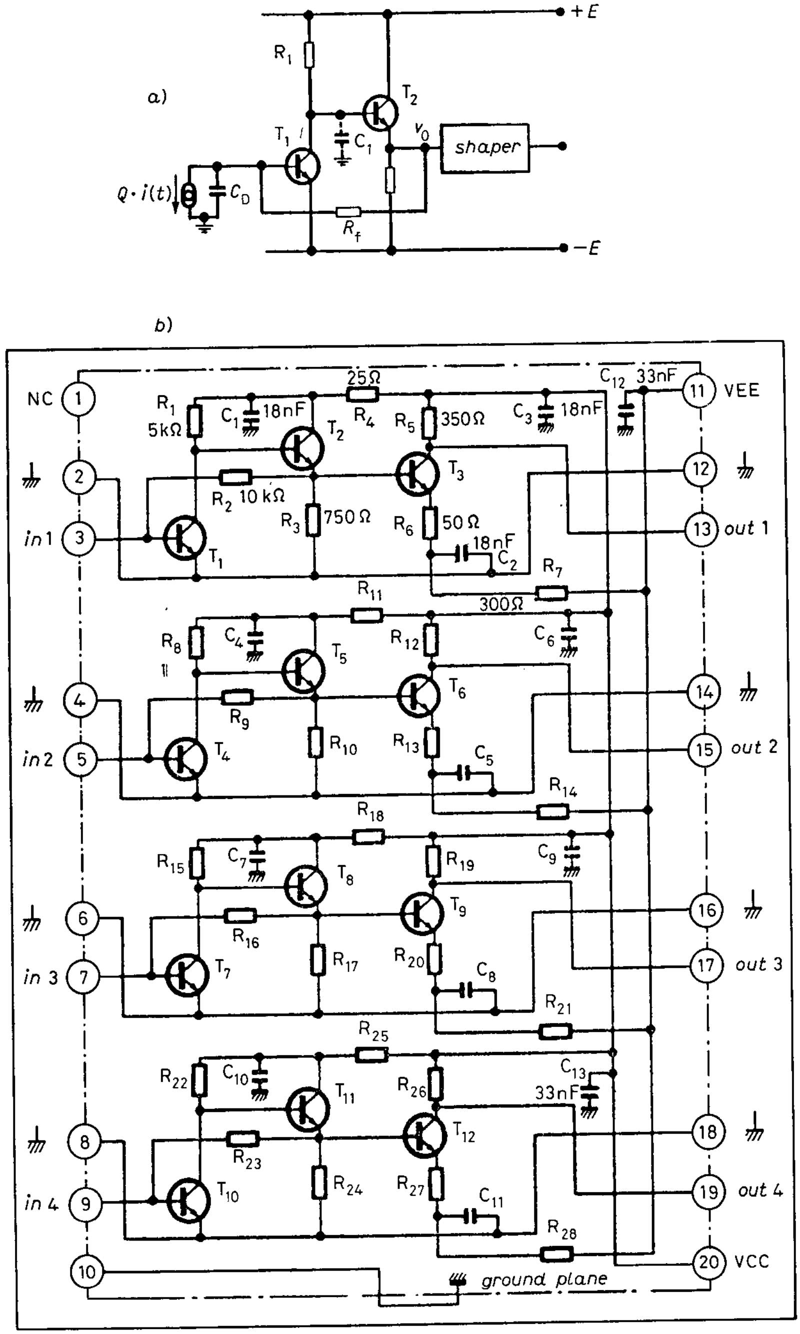

Fig. 9.7. – Current-sensitive preamplifier: *a*) basic preamplifier configuration followed by a shaper, *b*) actual hybrid preamplifier with 4 channels on the substrate.

The Fourier transform of the output signal is

$$V_0(\omega) = -I(\omega) Z_i(\omega) g_m \frac{1}{j\omega C}. \tag{9.11}$$

From eq. (9.10) the relative importance of the various terms can be investigated. In a well-designed preamplifier, Σ_D or $\Sigma_{BB'} g_m^2 + \Sigma_D$ are the dominant terms. However, when L is omitted and low supply voltages are used to reduce consumption, the value of R_1 may turn out to be not sufficiently large and its noise contribution may be not negligible.

To reduce the contributions due to the shot noise in the base currents I_{B_1} and I_{B_2}, it is advisable to fix low collector currents in T_1 and T_2, that is, less than 1 mA.

The low-noise amplifying block of fig. 9.6 can be transformed into a charge-sensitive loop by connecting between input and output the parallel combination of a capacitor and a resistor. A resistor of comparatively low value, $R_f \sim 10$ kΩ, connected between input and output implements a current-sensitive preamplifier.

9'3. *Practical preamplifier configurations.* – This subsection reviews some preamplifier configurations that have been developed during the last few years for specific applications in elementary-particle physics.

The circuit of fig. 9.7 is a current-sensitive configuration designed for microstrip signal processing [7, 8].

As shown in fig. 9.7*b*), the transistors T_1, T_2 implement the inverting preamplifier around which the current-sensitive loop is designed. The transistor T_3 provides additional voltage gain. The circuit 9.7 is being extensively used at CERN in association with microstrip detectors.

The preamplifier shown in fig. 9.8 is a common-base configuration, while that of fig. 9.9 is a charge-sensitive one [9].

Comparison was made between the noise performances of the three preamplifiers of fig. 9.7-9.9 with the special aim of investigating their behaviour at short processing times [9].

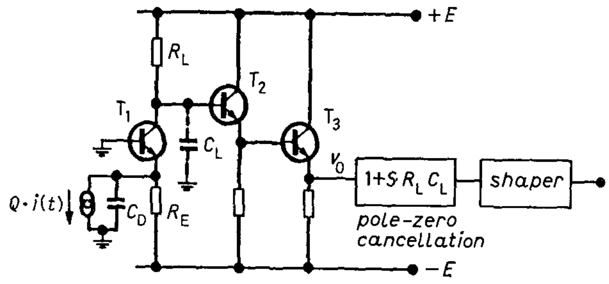

Fig. 9.8. – Common-base preamplifier.

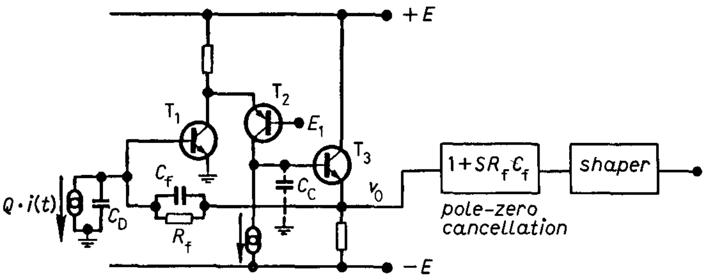

Fig. 9.9. – Charge-sensitive loop.

For this purpose, the same fast bipolar transistor, a NEC specimen featuring a 5 GeV f_α at $I_C = 5$ mA and $R_{BB'}$ between 10 and 15 Ω, was employed as input stage of the three preamplifiers. Its collector current was fixed around 0.7 mA.

TABLE 9.I.

ENC$_P$ [r.m.s.e.]

$W(t)$	Preamplifier		
	charge sensitive $R_f = 150$ kΩ	current sensitive $R_f = 10$ kΩ	common base $R_L = 22$ kΩ $R_E = 27$ kΩ
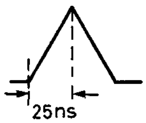	1265	1434	1434
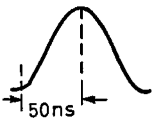	1786	2020	2020

ENC$_S$/C_D [r.m.s.e./pF]

$W(t)$	Preamplifier		
	charge sensitive	current sensitive	common base
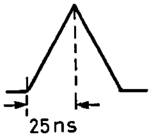	18	18	18
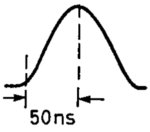	14.7	14.7	14.7

The results obtained are shown in table 9.I, which presents the values of the ENC at $C_D = 0$ and the asymptotic slope of ENC *vs.* C_D for the three configurations of fig. 9.7-9.9 and for two different noise weighting functions.

The slightly better behaviour of the charge-sensitive preamplifier at $C_D = 0$ has to be attributed to the fact that, compared to the other two circuits, it has a lower thermal-noise contribution from the bias resistors.

Preamplifiers of the types 9.7-9.9 have been realized in thick-film technology and are commercially available.

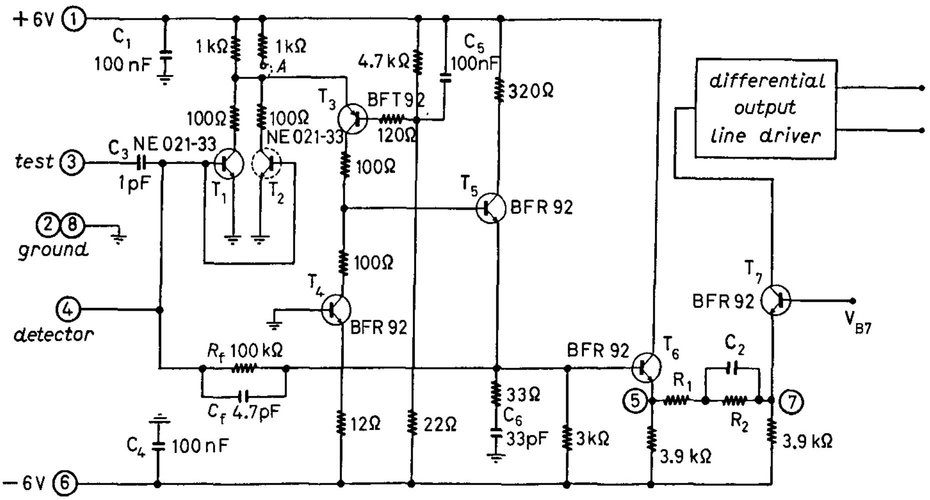

Fig. 9.10. – Preamplifier consisting a of charge-sensitive loop followed by pole-zero cancellation.

Figure 9.10 shows a complete preamplifier based upon an input charge-sensitive loop, transistors T_1, T_2, T_3, T_4, T_5, a pole-zero cancellation and amplification section consisting of transistors T_6, T_7 and passive network between their emitters and of a differential output line driver [10].

The noise behaviour of this preamplifier is close to that described in table 9.I. The circuit is commercially available in thick-film hybrid version, with either a single transistor or two paralleled transistors in the input stage. In the latter version, aiming at reducing the noise contribution from $R_{BB'}$, it was employed with the detectors of the silicon active target developed by the Milan group for the second part of the FRAMM experiment.

In that application, with a detector capacitance of about 80 pF and a shaping implemented by a semi-Gaussian prefiltering with 25 ns FWHM followed by a gated integrator with 70 ns gate width, it featured an ENC of 2200 electrons r.m.s.

Based upon a configuration similar to that of fig. 9.10 is the preamplifier with field-effect transistor input stage developed by the group of Milan for the low-noise data acquisition from the germanium bulk detector employed in the second part of the FRAMM experiment. Also this unit is now commercially available in thick-film, hybrid version. The FRAMM preamplifier at $C_D = 0$ and with a Gaussian shaping of 0.5 µs peaking time features less than 300 electrons r.m.s. An improved version, with reduced thermal-noise contribution from the feedback resistor, presents 150 electrons r.m.s. at $C_D = 0$ and with a Gaussian shaping of about 0.7 µs peaking time.

A preamplifier for very large detector capacitances and short shaping times, which employs five paralleled bipolar transistors in the input stage, is shown in fig. 9.11. The preamplifier of fig. 9.11 consists of a charge-sensitive loop, transistors T_1 to T_8, of a pole-zero cancellation and amplifying stage, transistors T_9, T_{10}, and of a balanced output stage, transistors T_{11}, T_{12} [11].

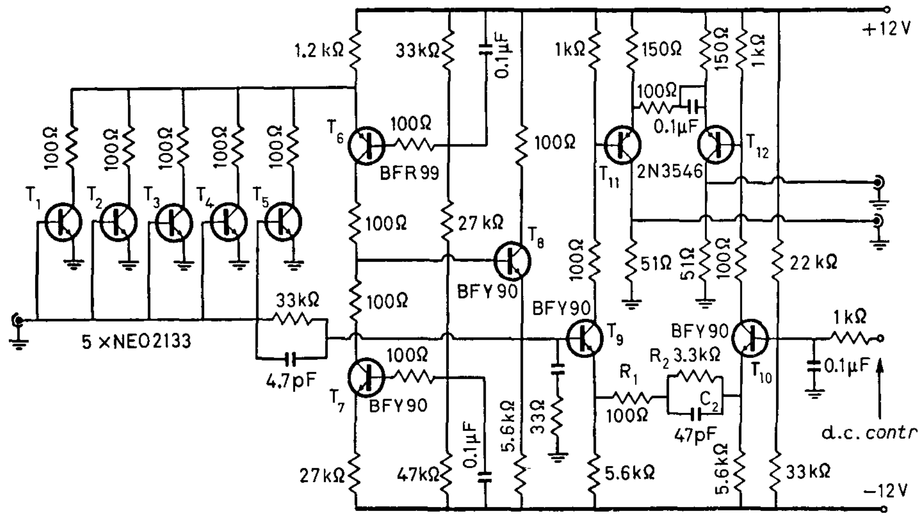

Fig. 9.11. – Preamplifer for very large detector capacitance.

The equivalent noise charge referred to the input is plotted as a function of detector capacitance in fig. 9.12.

The measurements were performed using an erfc-type weighting function with a FWHM of 30 ns. The slope of the noise linewidth *vs.* detector capacitance plot is about 5.8 r.m.s. electrons/pF. In applications with detectors of very large capacitance and when the constraint of very high rates is present, operation at values of τ shorter than the preamplifier risetime may be necessary. In this case, the need arises of stabilizing the preamplifier risetime, otherwise inaccuracies of the type seen discussing the ballistic error may occur. If the preamplifier is based on a charge-sensitive loop, this is equivalent to state, according to the model of fig. 9.3, that its cold resistance must be stabilized [12]. This requires a stabilized $g_{m,T}$. If the input stage employs bipolar transistors

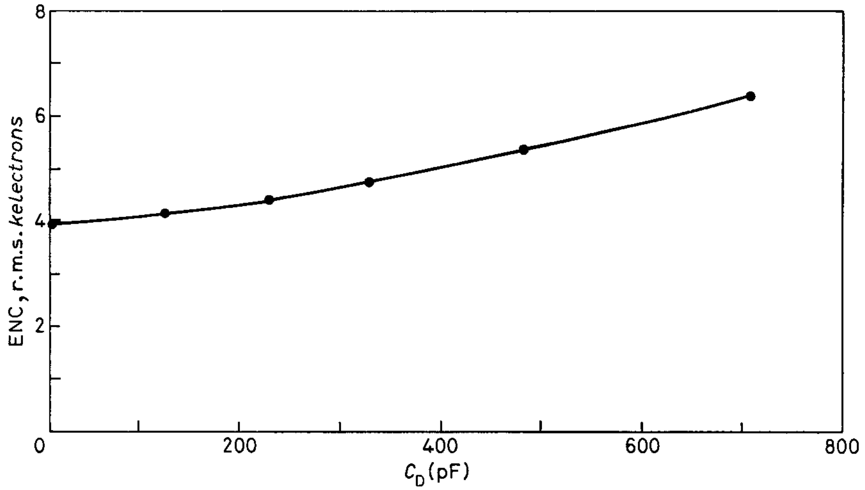

Fig. 9.12. – Equivalent noise charge as a function of detector capacitance C_D; $I_c = 0.87$ mA in each of T_1 to T_5 transistors.

and, as in the case of fig. 9.6, no current gain exists between the input stage and the output, then $g_{m,T} = g_m = qI_C/kT$. At fixed collector current I_C, g_m has a thermal coefficient of $\approx 0.3/°C$. This means that the extent to which the risetime is affected by thermal variations in g_m is negligible. If a field-effect transistor is employed as input device, risetime stabilization requires more elaborated circuitry, for the transconductance of a field-effect transistor is more dependent on temperature.

The stabilization of the input cold resistance in a charge-sensitive loop is based upon the principle shown in fig. 9.13 [4, 12].

In the circuit of fig. 9.13 the amplifier A, the transistor T and the resistive divider R_1, R_2 implement a feedback stabilized transconductance amplifier.

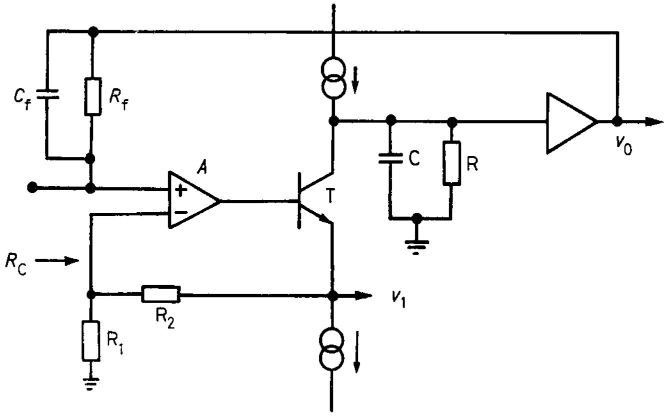

Fig. 9.13. – Charge-sensitive preamplifier with stabilized cold resistance.

The value of the transconductance is $1/R_1$. If the condition $R_f C_f = RC$ is met, the cold resistance appearing at the preamplifier input is, accordingly, $R_1 C/C_f$. Two outputs are available in the circuit 9.13, the usual integrated one is taken at v_0, while a fast output, closely reproducing the detector current pulse, can be taken at v_1. The latter signal can be of some usefulness if fast trigger operations have to be performed. In the design of this preamplifier a low value of R_1 must be used, as already pointed out, to avoid a noticeable increase in the series white noise.

Preamplifiers with stabilized cold resistance have been employed in data acquisition from silicon telescopes during the first part of the FRAMM experiment. They were associated with detectors of 700 pF capacitance and the counting rate during the accelerator spill was about 10^6 pulses per second.

An example of preamplifier of the type 9.1c) developed to sense the voltage signal across a stack of series-connected detectors is shown in fig. 9.14 [13].

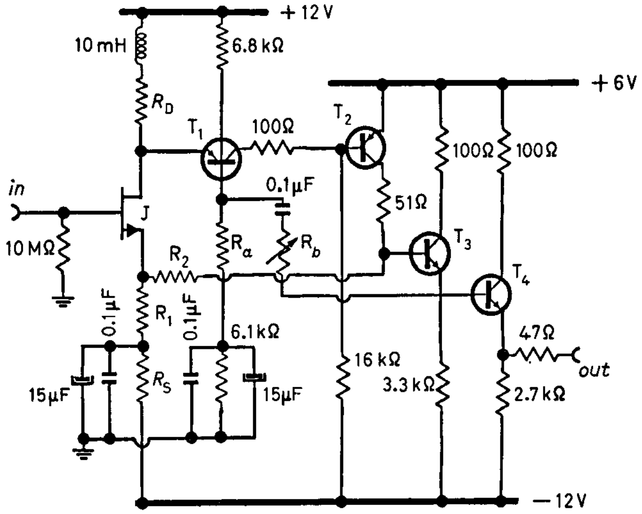

Fig. 9.14. – Voltage-sensitive preamplifier.

The feedback loop in the circuit of fig. 9.14 includes the input field-effect transistor J, the common-base transistor T_1 and the common-emitter transistor T_2, whose collector current is injected into the source of J. The output is taken from the collector of T_2 through the emitter followers T_3, T_4.

The voltage gain of the preamplifier is approximately $(R_1 + R_2)/R_1$.

An interesting feature of the preamplifier of fig. 9.14 is that its input capacitance can be zeroed. The gate-to-source capacitance of J appears at the input strongly attenuated by virtue of the series voltage feedback applied to the source of J. Positive feedback from the output to the base of T_1 via the voltage divider R_a, R_b has the effect of cancelling in the preamplifier input capacitance the contribution due to the gate-to-source capacitance of J.

The effectiveness in the control of the input capacitance achieved with the R_a, R_b voltage divider is shown in fig. 9.15. As pointed out in subsect. 9.1, one of the attractive features of the voltage-sensitive preamplifier is the very small dependence of risetime on detector capacitance C_D. As shown in fig. 9.16, the risetime of the preamplifier given in fig. 9.14 after an initial decrease remains constant around 6 ns up to 600 pF detector capacitance.

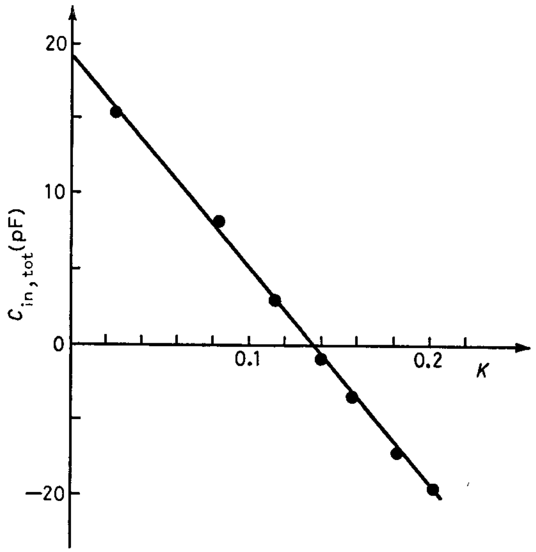

Fig. 9.15. – Input capacitance of the voltage-sensitive preamplifier as a function of the attenuation ratio K of the R_a, R_b voltage divider.

The noise behaviour of the voltage-sensitive preamplifier analysed with a triangular, time-invariant shaper with 100 ns base width is shown in fig. 9.17, curve *a*).

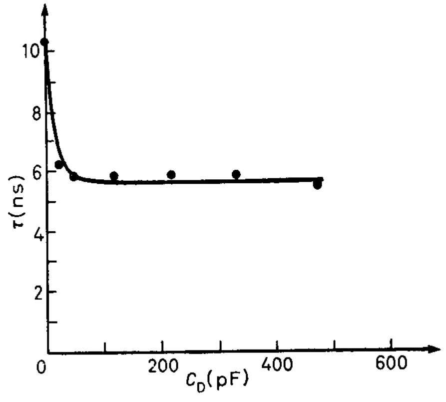

Fig. 9.16. – Risetime of the voltage-sensitive preamplifier as a function of C_D.

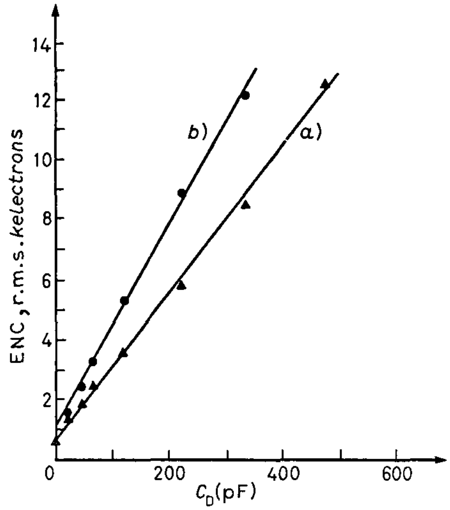

Fig. 9.17. – Equivalent noise charge as a function of the detector capacitance for the voltage-sensitive preamplifier of fig. 9.14: curve *a*) single-ended configuration of fig. 9.14, curve *b*) differential configuration.

A voltage-sensitive difference configuration has been developed by coupling two circuits of the type shown in fig. 9.14. Its purpose is that of sensing the voltage across a floating detector in a stack of series-connected elements [13].

The equivalent noise charge for the differential voltage-sensitive configuration is described, as a function of C_D, by curve *b*) of figure 9.17.

REFERENCES

[1] P. F. Manfredi: *Electronics for silicon detectors in high energy experiments*, in *Proceedings of the Meeting on Miniaturization of High Energy Physics Detectors, Pisa, September 1980*, edited by A. Stefanini (Plenum Press, New York, N. Y., 1983), p. 77.

[2] J. K. Millard, T. V. Blalok and N. W. Hill: *IEEE Trans. Nucl. Sci.*, NS-**19**, 388 (1972).

[3] V. Radeka: *IEEE Trans. Nucl. Sci.*, NS-**21**, 51 (1974).

[4] E. Gatti and P. F. Manfredi: *Low noise current preamplifiers for large capacitance semiconductor detectors and high counting rates*, in *Proceedings II* ISPRA *Nuclear Electronics Symposium*, Publ. EUR 5370 e (1975), p. 33.

[5] M. Goyot: *A hybrid, broadband, low noise charge preamplifier for simultaneous high resolution energy and time information with large capacitance semiconductor detectors*, in *Proceedings II* ISPRA *Nuclear Electronics Symposium*, Publ. EUR 5370 e (1975), p. 99.

[6] E. Gatti, P. F. Manfredi and V. Speziali: *Nucl. Instrum. Methods Phys. Res.*, **226**, 163 (1984).

[7] E. Heijne and P. Jarron: *Silicon detectors, a new tool for high energy physics*, in *Silicon Detectors for High Energy Physics, Proceedings of a Workshop held at Fermilab, October 15-16, 1981*, edited by T. Ferbel (1981), p. 1.
[8] P. Jarron and M. Goyot: *Nucl. Instrum. Methods Phys. Res.*, **226**, 156 (1984).
[9] P. D'Angelo, A. Hrisoho, P. Jarron, P. F. Manfredi and J. Poinsignon: *Nucl. Instrum. Methods*, **193**, 533 (1982).
[10] G. Bellini, M. Conte, P. D'Angelo, P. F. Manfredi, D. Menasce, E. Meroni, L. Moroni, S. Sala and M. Szawlowski: *IEEE Trans. Nucl. Sci.*, NS-**30**, 415 (1983).
[11] E. Gatti, P. Inzani, P. F. Manfredi and D. Marioli: *Design of low noise preamplifiers for some special application in high energy experiments*, in *Proceedings of the Symposium on Nuclear Electronics, Bratislava, 6-12 September 1983* (1983), p. 67.
[12] E. Gatti and P. F. Manfredi: *IEEE Trans. Nucl. Sci.*, NS-**24**, 66 (1978).
[13] E. Gatti, P. F. Manfredi and D. Marioli: *Nucl. Instrum. Methods Phys. Res.*, **221**, 536 (1984).

10. – Linear amplifier and shaper.

The signal delivered by the preamplifier has to go through further processing before being presented to the amplitude-measuring system. Such a processing consists of amplification and shaping.

Shaping has been exhaustively discussed in sect. **4**, **5**. It has been pointed out that some kinds of shaping operations—it would be better to say some kinds of noise weighting functions—can be implemented, in both time-invariant or time-variant ways.

Other weighting functions are preferably implemented in one or in the other way. The present trend in elementary-particle physics relies upon the synthesis of the weighting function based upon gated integrators. This trend finds its explanation in the fact that, as pointed out already, in most of analog signal acquisition channels a gated integrator is present as a part of the charge-sensing analog-to-digital converters.

Between preamplifier and gated integrator, a linear-amplifier system is required, whose purpose is that of matching the signal level to the amplitude range required by the gated integrator and to perform on it the time-invariant preshaping. The amplifier system may be a potential source of both inaccuracy in the amplitude measurement and of spectral-line broadening caused by baseline shifts at high counting rates. Baseline shifts occur in a.c. coupled amplifier systems because of the random superposition of the tails that follow the pulse [1-3].

The effect is explained in fig. 10.1 which shows the behaviour of a d.c. level blocking network, RC differentiator, on a rectangular signal applied at the input. The input signal is strictly unipolar and has an amplitude V and a width τ, which is supposed to be much shorter than the differentiator time

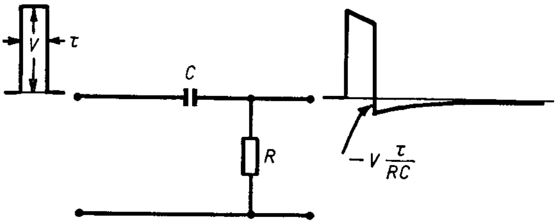

Fig. 10.1. - Negative tail following the positive pulse and due to the *RC* differentiator.

constant *RC*. As the input signal is of finite area and the transfer function of the differentiator has a zero in the origin of the complex *s*-plane, the output signal has zero area. Consequently, the positive output signal is followed by a negative tail which starting from the value $-V(\tau/RC)$ tends to zero exponentially with time constant *RC*. The time dependence of the tail is

$$-V\frac{\tau}{RC}\exp[-t/RC]\,. \tag{10.1}$$

Assume, for the sake of simplicity, that the input pulses have a very narrow, δ-like amplitude distribution. The random arrival of the pulses with average rate λ creates a stochastic baseline. According to Campbell's theorem applied to (10.1), the mean value of the baseline is

$$-\lambda\tau V \tag{10.2}$$

independent of the time constant *RC* and its variance is

$$\frac{\lambda\tau^2}{2RC}V^2\,. \tag{10.3}$$

The original indefinitely narrow pulse amplitude distribution would undergo a relative broadening described by the standard deviation

$$\left[\frac{\lambda\tau^2}{2RC}\right]^{\frac{1}{2}}. \tag{10.4}$$

It has to be pointed out that baseline shift may be present also in d.c. coupled systems employing pole-zero cancellations, if these are not correctly adjusted.

It is worth discussing now in which situations baseline shift and related statistical fluctuations are important.

The most critical condition is that of a telescope of silicon detectors in a fixed-target experiment. With reference to (10.4) it can be said that in a pulsed accelerator the time constant *RC* cannot be made very large, otherwise a long settling transient would be present on the baseline at the beginning of every machine burst. For instance, in an a.c. coupled amplifier working at 10^6 pulses per second, each pulse lasting 100 ns and with a RC time constant of 10 μs, the baseline shift would be 10 % of the signal amplitude and the standard deviation of the output amplitude distribution would be about 2 %. At low particle multiplicities, such a contribution to the line broadening is not negligible.

Three classical solutions borrowed from nuclear spectroscopy to remove baseline effects are baseline restoration, double sampling, that is, sampling the baseline before the pulse arrival and the peak of the pulse and then taking their difference, and bipolar shaping [4-9]. They are schematically illustrated in fig. 10.2. The circuit of fig. 10.2*a*) is the well-known time-variant baseline restorer. The incoming positive pulse through the switch control circuit opens S, thereby making the differentiation time constant associated with C infinitely larger. At the end of the positive pulse, the switch gets closed. Tails of negative sign which might exist owing to the presence of earlier differentiating stages are clipped because the time constant rC is chosen suitably short. In this way the zero value of the baseline is quickly recovered and the effects of baseline shift strongly reduced.

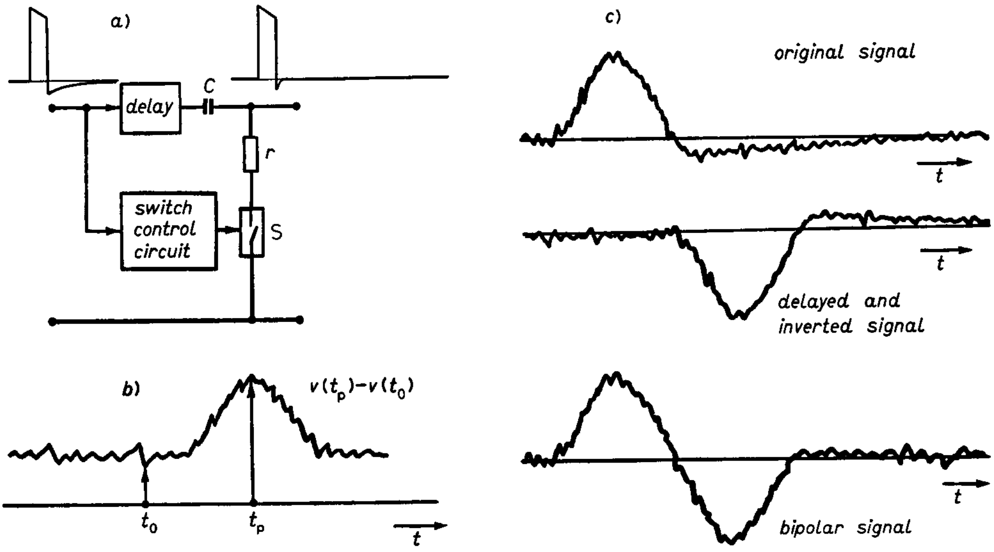

Fig. 10.2. – Three ways of avoiding baseline shift at high counting rates: *a*) baseline restorer, *b*) sampling the baseline and the peak of the pulse, *c*) bipolar shaping.

The baseline restorers, to be effective in the conditions of high-energy experiments, at counting rates of millions pulses per second, must execute a quick level clamping after the pulse and this clamping action must last until the next pulse. As a result, the faster noise components for which no correlation exists between the values immediately preceding and immediately following the positive-going edge of the pulse undergo a $\sqrt{2}$ increase.

The method of fig. 10.2*b*) cancels the baseline component by measuring the peak amplitude of the signal with a double sampling of the total wave form.

As to the effect on the high-frequency noise, the double sampling behaves exactly like the baseline restorer, that is, it introduces a $\sqrt{2}$ noise worsening. In fact, the resulting weighting function is the original one inverted in polarity and delayed of a time interval equal to its width.

Figure 10.2*c*) shows how a first-order tail cancellation can be achieved by using bipolar shaping, that is, by adding to the original signal the same signal inverted and delayed. As already pointed out, bipolar shaping, compared to the unipolar one based upon the same kind of signal, introduces a $\sqrt{2}$ deterioration in the noise. For a general approach to the area-balanced wave forms and, among them, the one giving the least noise for a defined overall width, the reader can refer to paper [4].

It can, therefore, be concluded that the three methods of reducing baseline shift described in fig. 10.2 all degrade the equivalent noise charge of a comparable amount, at least if the dominant noise term is the series white one. Such a degradation is hardly tolerable in several experimental conditions of elementary-particle physics, where the signal-to-noise ratio is intrinsically poor.

Effort was accordingly concentrated on a possible way of achieving the desired counting rate performances with the slightest sacrifice in signal-to-noise ratio. A method was introduced, called periodical stabilization of the amplifier system, which was proven to meet the stated requirement. The idea it is based upon is shown in fig. 10.3 [10].

The fast signal path in the diagram of fig. 10.3 is d.c. coupled from the

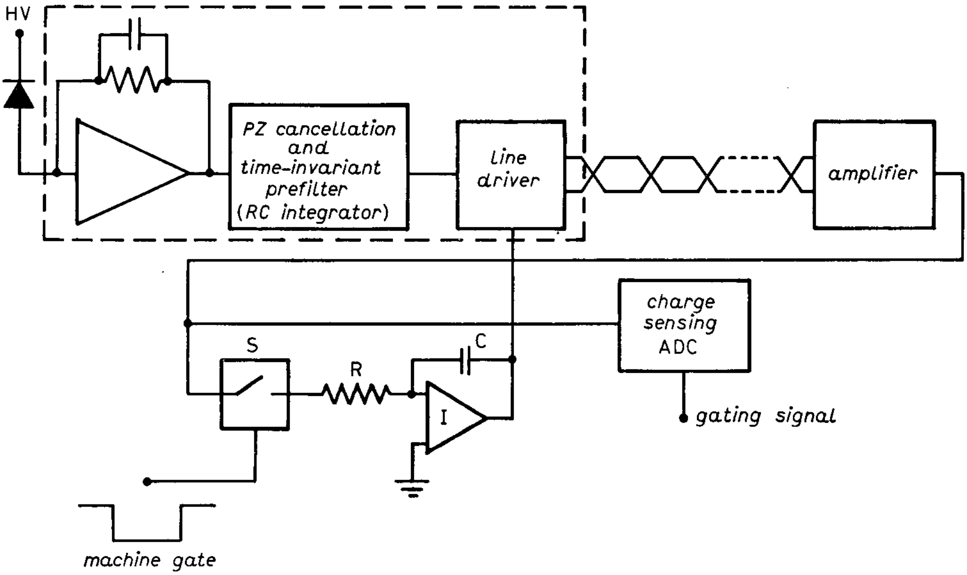

Fig. 10.3. – Periodically stabilized amplifier system.

detector to the ADC input, provided that the switch S is open. In this situation, if the pole-zero cancellation networks on the signal path are properly adjusted, the pulses along this path are strictly unipolar and no baseline shift occurs.

The linear processor as a whole can be considered as a time-variant shaper preceded by a time-invariant preshaping. The time-variant shaping is implemented by the gated integrator provided in the ADC. The time-invariant preshaping results from the intrinsic band width limitations in the amplifier system for the faster realizations, and from some lumped integrations in the slower versions. The time-variant preshaper can be assumed to be Gaussian in both cases and the complete noise weighting function is almost trapezoidal with erfc-type leading and trailing edges.

The d.c. coupled fast channel cannot work alone, for the thermal and long-term drift would introduce slow instabilities in the output baseline. In order to avoid this, a correction path has been introduced, which implements the periodical stabilization. The correction path includes the switch S and a long-term integrator whose output voltage is fed back to the preamplifier. The correcting phase takes place during the interburst periods of the accelerator, when the beam is off and no radiation falls on the detector.

The switch S remains closed throughout the interburst period. The feedback loop, which encircles the preamplifier output stage, the amplifier, the switch S and the long-term integrator, forces the output of the amplifier to zero.

A correcting voltage builds up across C, which accounts for any long-term and thermal drift in the signal processor. At the beginning of the next accelerator burst, S opens again. The correcting voltage stored on C, however, keeps the working points in the amplifier stable during the accelerator burst. A new correcting phase, which has the purpose of updating the correcting voltage on C, starts at the beginning of the next interburst period. The sequence of acquisition and correction phases is shown in fig. 10.4*a*). Figure 10.4*b*) shows that no baseline shift occurs during the accelerator burst, despite the high pulse rate at which the picture was taken, more than 10^6 p.p.s. The effect of wrong operation of the switch S is shown in fig. 10.4*c*). If S is left permanently closed, then the system of fig. 10.3, with the feedback not interrupted when pulses are delivered by the detector, behaves as an a.c. coupled amplifier. Baseline shift takes place at the beginning of the accelerator burst and then the baseline settles to the negative value predicted by (10.2). The dependence of the centroid of a spectral line on the counting rate is shown in fig. 10.5 for both correctly operated and permanently closed switch S.

With the switch S correctly operated, less than 0.3% centroid shift occurs raising the counting rate up to $\sim 3\cdot 10^6$ pulses per second. If, instead, S is left permanently closed, a large variation is noticed in the centroid position by varying the counting rate in the same range as before.

The behaviour of the periodically stabilized amplifier system at high counting rates is also described by the spectra of fig. 10.6.

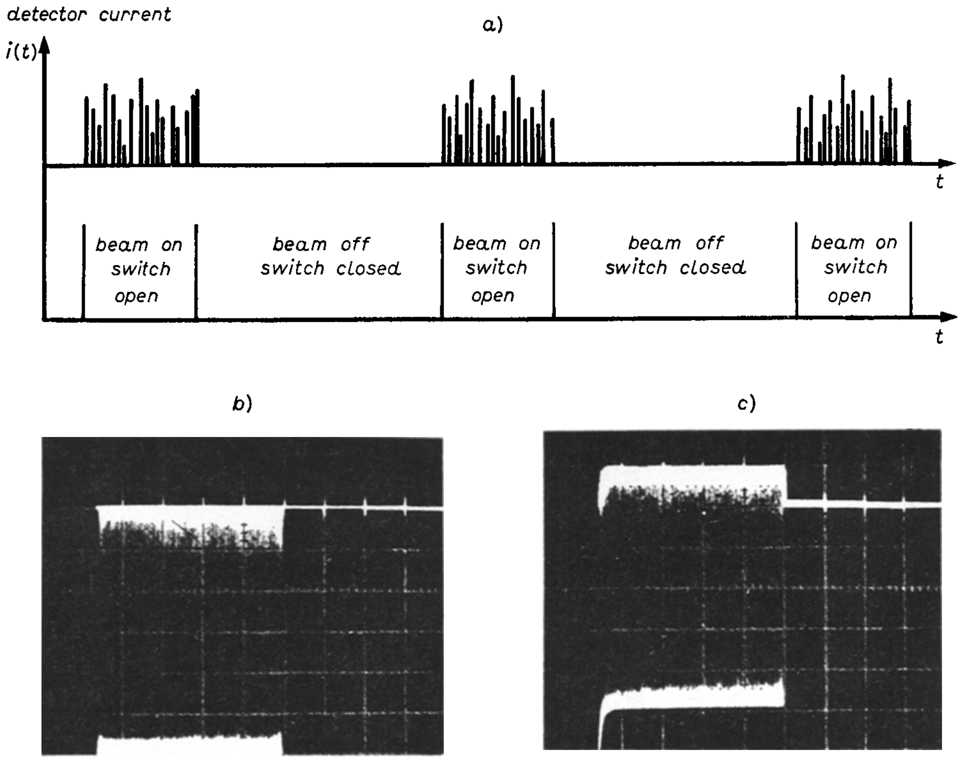

Fig. 10.4. – *a*) Sequence of acquisition and correction phases. *b*) Baseline at the amplifier output with the switch S correctly operated. *c*) Baseline at the amplifier output with the switch S permanently closed.

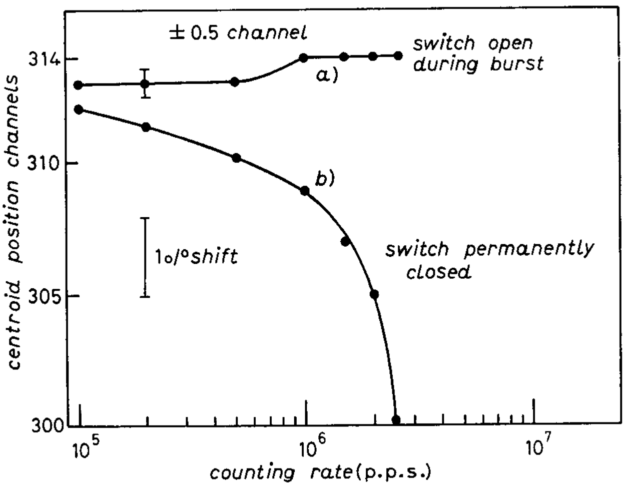

Fig. 10.5. – Dependence of the centroid of a spectral line on the counting rate: *a*) switch S correctly operated, *b*) switch S permanently closed.

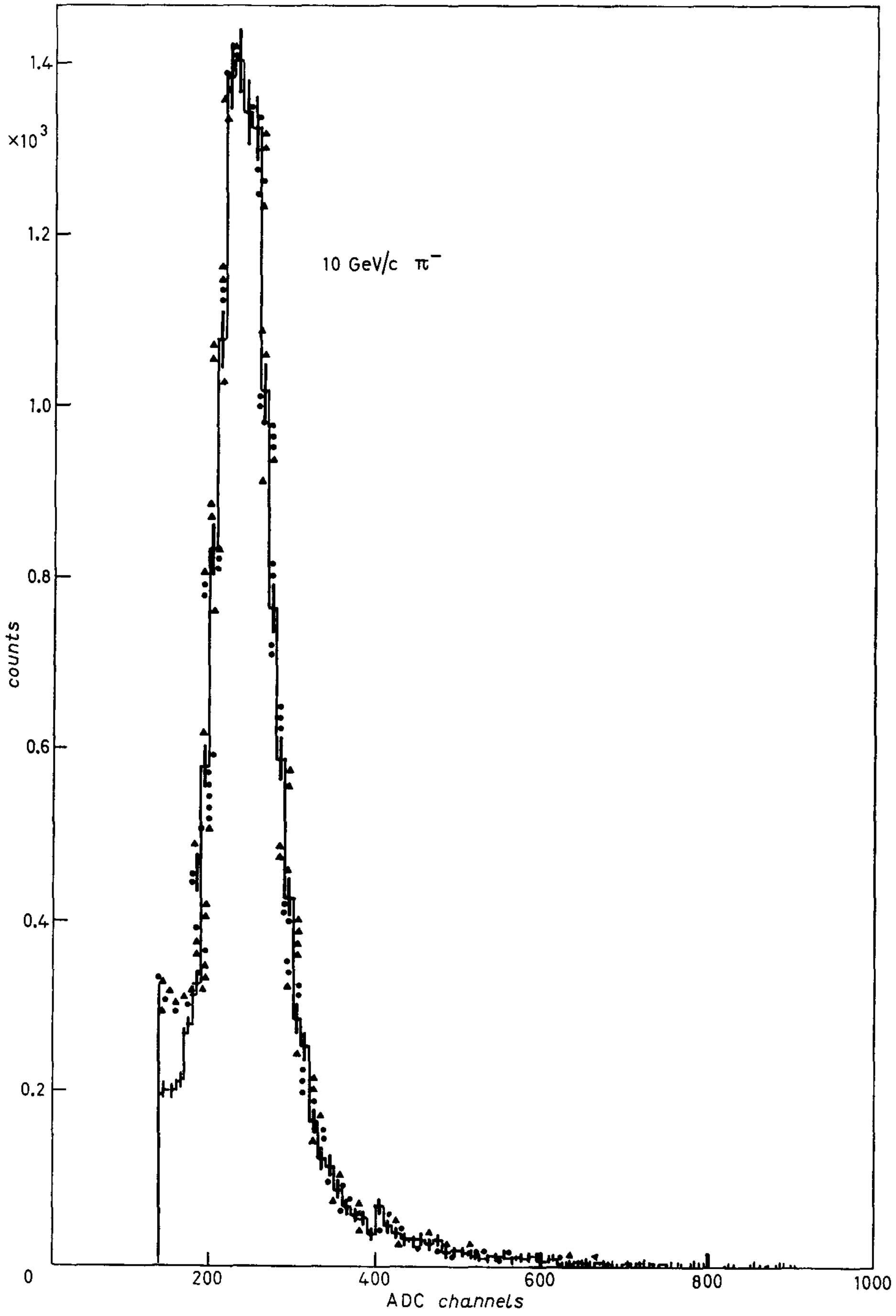

Fig. 10.6. – Landau distributions of negative π-mesons recorded at three different counting rates: ——— $2.7 \cdot 10^5$ p.p.s., ▲▲▲ $5.1 \cdot 10^5$ p.p.s., ●●● 10^6 p.p.s.

Figure 10.6 shows that no significant shape variation occurs in the Landau distribution of minimum-ionizing particles by increasing the counting rate up to 10^6 p.p.s.

The principle of periodical baseline stabilization is presently being employed in some fixed-target experiments, where it proved to be successful in high-duty-cycle data acquisition from both silicon and germanium active targets. It thoroughly confirmed its capability of ensuring outstanding counting rate performances without degrading the intrinsic equivalent noise charge of the detector-preamplifier assembly.

Highly segmented detectors, like microstrip planes, even if employed in fixed-target experiments, do not present usually critical problems of baseline shift and baseline fluctuations because the average duty cycle in each acquisition channel is small, less than 1%. For these situations, a.c. coupled amplifier systems are suitable. The only requirement which has to be met is that the differentiating time constants in the amplifiers be adequately short to enable a quick baseline settling to the standing value at the beginning of the accelerator bursts.

In the collider applications, as long as the spacings between bunch crossings are of several microseconds, the baseline problems are negligible. This statement is reinforced by the remark that in collider experiments all the detectors are segmented and the tracks are spread over a large solid angle. Therefore, the counting rates on the individual detector segments will be definitely small. The situation might change in future large hadron colliders, where the time between bunch crossing will be a few tens of nanoseconds and the number of charged tracks per event will be large. The machine parameters for these colliders, however, are still under investigation and no conclusion can be drawn as yet.

Before concluding this section, some alternative ways of realizing the shaping function will be described. A first example is shown in fig. 10.7 [11, 12]. Accord-

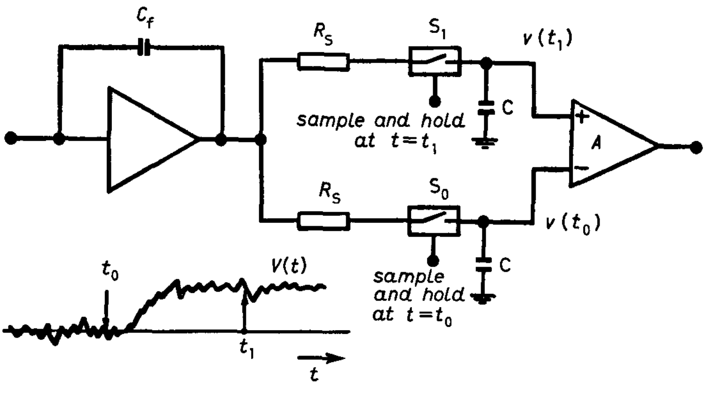

Fig. 10.7. – Shaping realized by sampling and holding the preamplifier output at different instants.

ing to the circuit diagram presented there, the output of the charge-sensitive preamplifier is split along two ways, each containing a resistor, a switch and a capacitor. A two-input amplifier takes the difference of the voltages stored on the capacitors. At $t = t_0$, shortly before the arrival of the pulse, the baseline is sampled by closing and reopening S_0 and the corresponding voltage is held on the relevant capacitor. At $t = t_1$, some time after the arrival of the pulse, S_1 is closed and reopened and the value $v(t_1)$ is held. At $t > t_1$ the voltage at the difference amplifier output provides the step amplitude to be measured.

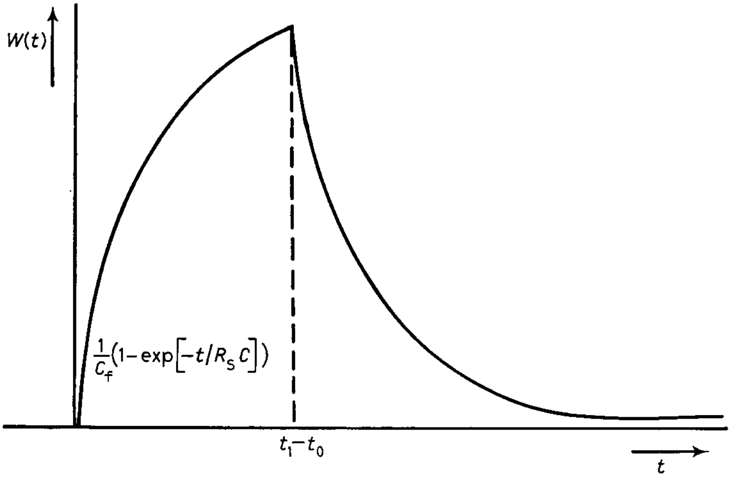

Fig. 10.8. – Weighting function realized.

The circuit of fig. 10.7 implements the weighting function shown in fig. 10.8. Such a function is identical to the one which would be obtained by applying a delay line clipping to the step response of an approximate integrator.

The sample and hold operation and the difference of the two samples, therefore, replace the delay line with two advantages. First, the delay between the two samples, $t_1 - t_0$, can be easily changed by acting upon the relative position of two logic pulses. Secondly, the circuit of fig. 10.7 lends itself to a possible monolithic integration, while obviously the delay line implementation of the same weighting function does not.

The present trend of realizing in monolithic form the high-density front-end circuits required by highly segmented detectors will benefit from the possibilities opened up by the principle of fig. 10.7. More generally, shaping can be based upon sampling the voltage at the preamplifier output at the instants $t_0, t_1, \ldots, t_k$, holding the samples in $k + 1$ capacitors and then combining the samples with suitable coefficients. For instance, a third path in the circuit of fig. 10.7 and the following linear combination of the samples $v(t_0)$, $v(t_1)$, $v(2t_1 - t_0)$

$$2v(t_1) - v(t_0) - v(2t_1 - t_0)$$

would implement a bipolar weighting function [13].

It might be argued that sampling the preamplifier output at $t = t_0$ requires a trigger signal which precedes the step at the preamplifier output with a fixed time relationship, otherwise a delay between the preamplifier and the sample and hold circuits is needed.

In collider experiments, where these techniques are supposed to be more perspective, the trigger signal defining t_0 can be made indeed available, as the events occur during the bunch crossings, that is, at a constant time distance from each other.

Always thinking of collider experiments, the switched-capacitor approach of fig. 10.9 can be employed to realize the best estimate of a random staircase in the presence of white noise discussed in sect. 4.

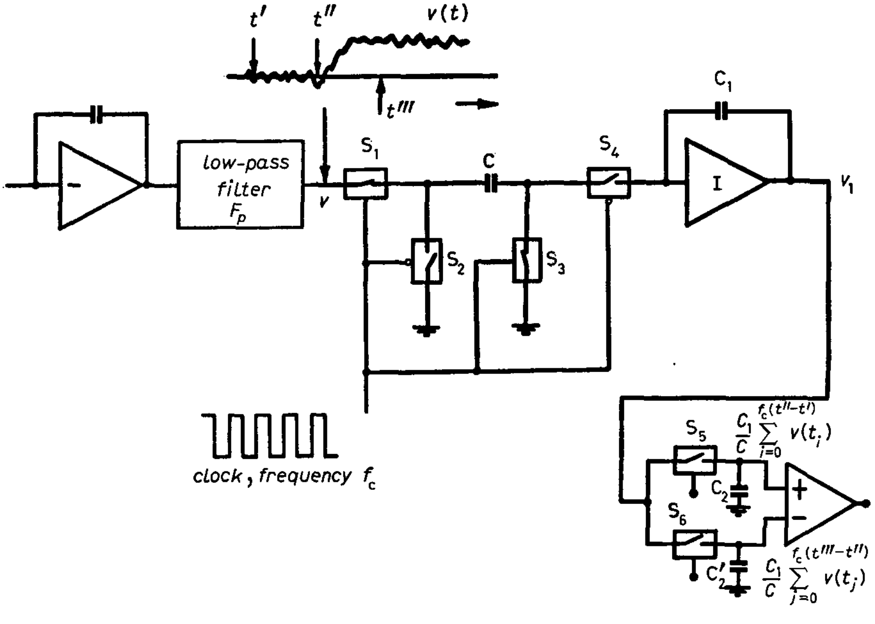

Fig. 10.9. – Switched-capacitor approach to optimum processing in the presence of white noise, F_p is a prefilter with a cut-off frequency lower than f_{clock}.

In the diagram of fig. 10.9 the capacitor C, the switches S_1, S_2, S_3, S_4 and the capacitive feedback around I realize an integrator based upon the switched-capacitor technique. As initial condition at $t = t'$ the capacitor C_1 is set at zero voltage by a switch not shown in the diagram and the clock is enabled. When the free-running clock is at one of the two logic levels, S_1 and S_3 are closed, S_2 and S_4 are open.

The capacitor C is connected between the output of the low-pass, band-limiting filter and ground, thereby charging to the output voltage v. During the other logic state of the clock, S_4 and S_2 are closed, S_1 and S_3 are open. The capacitor

C is now connected between the inverting node of I and ground. Its charge Cv is transferred to C_1. The voltage at the output of I as the result of N sample and hold operations at the clock rate f_c is

$$V_I(t) = \frac{C}{C_1} \sum_{i=0}^{N} v(t_i) ,$$

where $v(t_i)$ is the voltage stored on C at the i-th sampling-holding operation.

Between t' and t'', when S_5 is closed and S_6 is open, V_I is stored on C_2, while it is stored on C_2' between t'' and t''', when S_5 is open and S_6 is closed. At $t > t'''$, the voltage at the output of A provides the best estimate of the step in $v(t)$.

The process ends by resetting the voltage across C_1 to zero. The low-pass filter performs the function of band-limiting the signal with a cut-off frequency lower than $f_c/2$.

The principle depicted in fig. 10.9 is based upon the classical switched-capacitor technique and, therefore, is of easy implementation in MOS monolithic technology.

REFERENCES

[1] E. Fairstein and J. Hahn: *Nucleonics*, **23**(9), 81 (1965).

[2] A. H. Snell, Editor: *Nuclear Instruments and Their Uses* (John Wiley and Sons, New York, N. Y., 1962), Chapt. 4.

[3] P. W. Nicholson: *Nuclear Electronics* (John Wiley and Sons, London, 1974), Chapt. 3.

[4] M. O. Deighton: *Minimum-noise filters with good low-frequency rejection*, in *Proceedings of* ISPRA *Nuclear Electronics Symposium, May 6-9, 1969*, Publ. EUR 4289-e (1969), p. 47.

[5] M. Bertolaccini, C. Bussolati, S. Cova, I. De Lotto and E. Gatti: *Nucl. Instrum. Methods*, **62**, 221 (1968).

[6] M. Bertolaccini, C. Bussolati, S. Cova, I. De Lotto and E. Gatti: *Optimization of signal-to-noise ratio in the presence of noise and pile-up fluctuations*, in *Proceedings of the Conference on Semiconductor Nuclear Particle Detectors and Circuits, Gatlinburg, 1967*, National Academy of Science, Publ. 1593 (1969), p. 523.

[7] R. L. Chase and L. R. Poulo: *IEEE Trans. Nucl. Sci.*, NS-**14**, 83 (1967).

[8] V. Radeka: *The effect of baseline restoration on signal-to-noise ratio in pulse amplitude measurements*, in *Proceedings of the Conference on Semiconductor Nuclear Particle Detectors and Circuits, Gatlinburg, 1967*, National Academy of Science, Publ. 1593 (1969), p. 620.

[9] M. Bertolaccini and C. Bussolati: *Nucl. Instrum. Methods*, **100**, 349 (1972),

[10] R. L. Chase, P. D'Angelo, A. Hrisoho, P. F. Manfredi and J. Poinsignon: *IEEE Trans. Nucl. Sci.*, NS-**29**, 602 (1982).

[11] T. F. Droege, F. Lobkowics and Y. Fukushima: *IEEE Trans. Nucl. Sci.*, NS-**25**, 687 (1978).

[12] T. F. Droege, H. C. Hibbard, C. A. Nelson jr., P. A. Thomson, Y. Makdisi and R. Lipton: *IEEE Trans. Nucl. Sci.*, NS-**27**, 64 (1980).

[13] J. P. Richer and R. L. Chase: *IEEE Trans. Nucl. Sci.*, NS-**31**, 258 (1984).

11. – Conclusive remarks on some problems of analog processing.

Some of the experimental situations described in the introduction will be reviewed now and the related problems of noise and counting rates will be considered again, in order to outline practical solutions. The more demanding condition, that is, the one arising in fixed-target experiments, will be assumed as a reference.

11'1. *Silicon telescopes.* – By virtue of the short collection time in the detector counting rates of several million pulses per second are theoretically possible. To achieve these rates in a real system, two problems have to be solved. First, optimizing the equivalent noise charge at processing times that are constrained to be in the range of a few tens of nanoseconds. Second, designing an amplifier system capable of working at these rates with negligible spectral-line degradation [1].

The most appropriate preamplifier solution looks to be based upon microwave bipolar transistors with low $R_{\text{BB}'}$. As the detector capacitance can be not small, frequently exceeding 100 pF, capacitive matching between detector and preamplifier is advisable.

To cope with the counting rates, the use of the periodical stabilization in the amplifier system is mandatory.

Analog processors based upon bipolar-transistor preamplifiers and periodical stabilization are presently employed in association with the silicon active targets of NAI, WA71, NA14 experiments [2-5].

They all employ time-variant shaping realized with the gated integrators of charge-sensing ADCs. The analog processors of NAI experiment, for instance, has the following characteristics. The noise weighting function results from the convolution of a Gaussian pulse with 25 ns FWHM and of a rectangle 70 ns wide. The equivalent noise charge with a detector capacitance of about 80 pF is 2200 electrons r.m.s. The Landau spectra at several multiplicities of minimumionizing particles, taken at a counting rate of 10^6 p.p.s., are shown in fig. 11.1 [2].

11'2. *Germanium bulk detector.* – The germanium bulk detectors employed in NAI experiment were of two different pitches, 50 μm and 100 μm. Owing to the long path that the charge carriers have to travel along in their collection motion, the collection times and their fluctuations are considerably larger than in silicon telescopes. For this reason longer time constants in the time-invariant preshapers and a wider gating window had to be employed. Preshaping was achieved with lumped *R-C* integrations.

The noise weighting function results from the convolution of an almost

Gaussian pulse with 200 ns FWHM and a 500 ns wide rectangle. The capacitance presented by each electrode to the preamplifier, basically due to the connections, is of the order of 30 pF. The small detector capacitance and the long duration of the noise weighting function suggest the field-effect transistor as the most suitable input device in the preamplifier. The amplifier system employs periodical stabilization and, like in the processor associated with the silicon target, time-variant shaping is implemented by the gated integrator of the charge-sensing ADCs. The equivalent noise charge for the germanium analog processors is 700 electrons r.m.s.

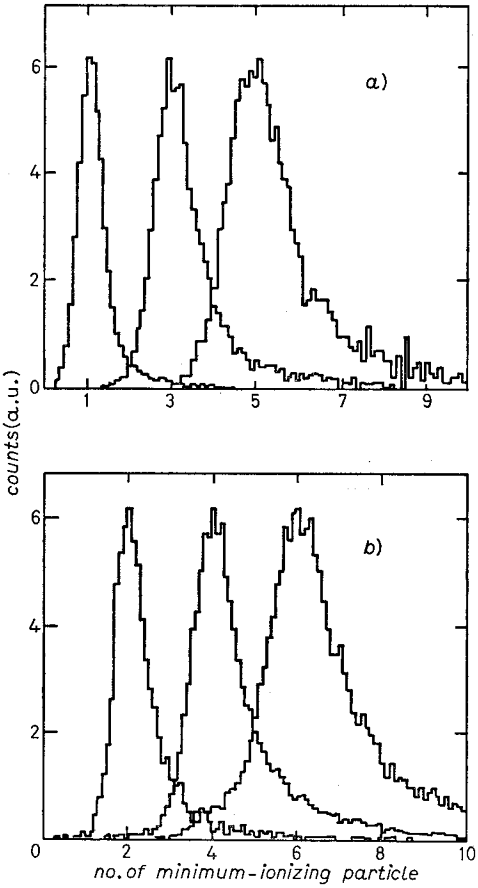

Fig. 11.1. – Landau distributions obtained with the NAI silicon active target: *a*) odd multiplicities, *b*) even multiplicities.

The noise line and the Landau distributions of two and four minimum-ionizing particles are shown in fig. 11.2 [6].

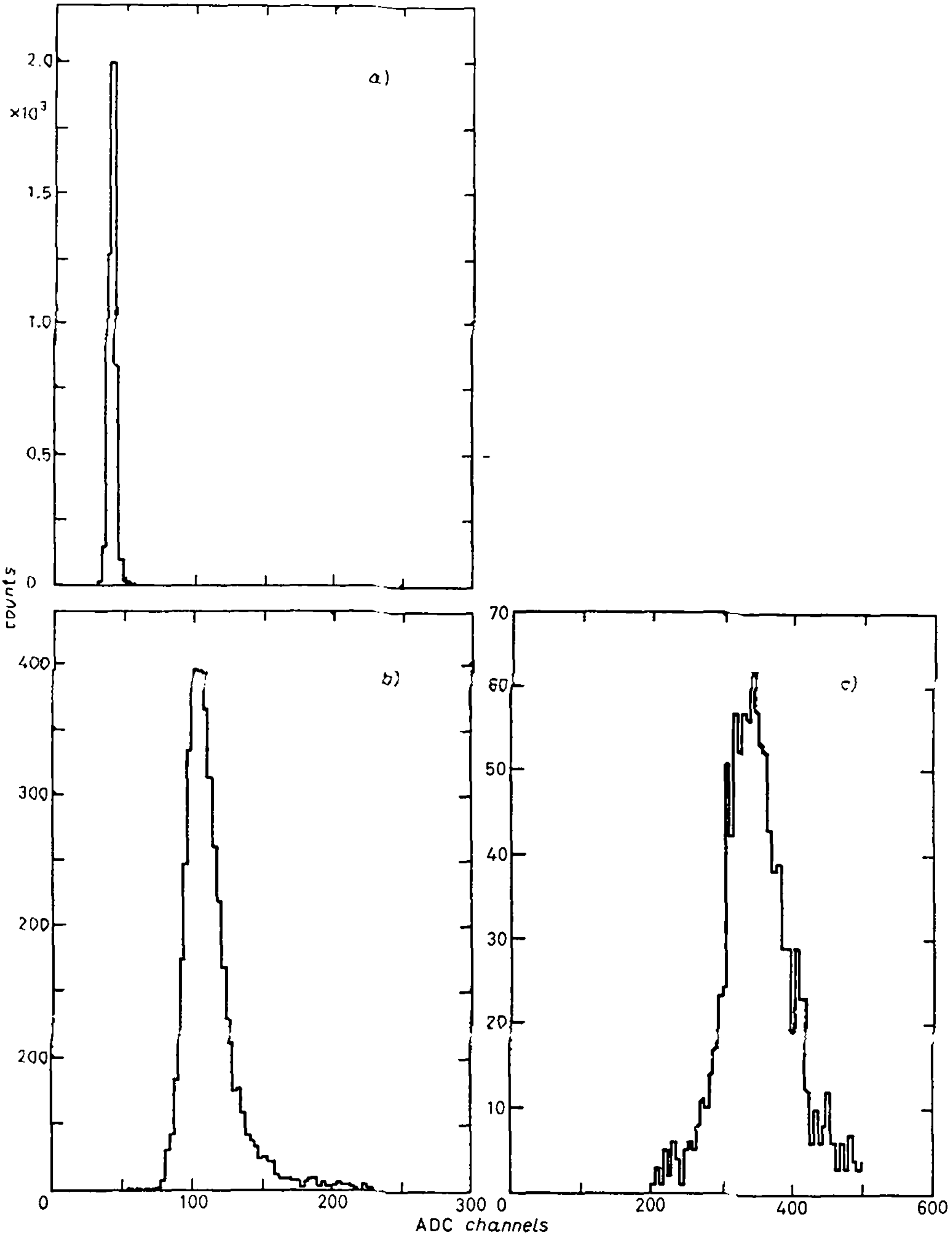

Fig. 11.2. – Noise line (*a*)) and Landau distributions of two (*b*)) and four (*c*)) minimum ionizing particles.

11'3. *Microstrip detectors.* – The position information in a microstrip detector can be read out according to two different approaches [7]. One, called strip-by-strip readout, requires one analog signal processor every strip. The other is based upon an interpolation method employing charge division and allows accordingly a reduction in the number of readout channels required.

The strip-by-strip readout is shown in fig. 11.3 [8-10].

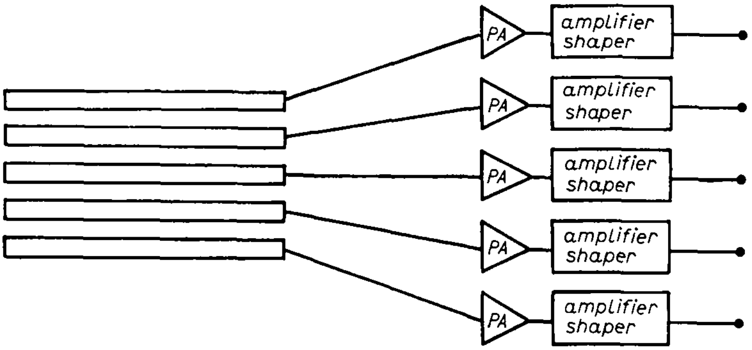

Fig. 11.3. – Strip-by-strip readout from a microstrip plane.

As the figure points out, in microstrip planes of small pitch, a serious problem is the one connected with the need of fanning out the signals from the strips to the preamplifiers. If the preamplifiers are of relatively large size, like in the case of thick-film circuits, for instance, the connections between the strips and the preamplifiers are long. The contribution of the fan-out to the total capacitance at the preamplifier input becomes dominant [7]. For instance, a printed-circuit fan-out designed to connect a microstrip detector with 50 μm pitch to a set of hybrid, thick-film preamplifiers would present at each output more than 30 pF. The capacitance presented by every strip would be of $(5\div10)$ pF. The signal-to-noise ratio, therefore, is badly affected by the fan-out circuit.

Besides that, a configuration of the type shown in fig. 11.3 introduces serious problems connected with the size of the front-end electronics and with the number of cables needed to convey the signals to the remote-end electronics. These two difficulties can be overcome in a fixed-target experiment, where the number of strips hardly exceeds 10^4, but would make the method unusable in the barrel-type microstrip assemblies foreseen for some collider experiments. Consequently, while present fixed-target experiments are still based upon discrete or thick-film circuits in configurations of the type of fig. 11.3, a monolithic approach to the design of the front-end electronics with a built-in demultiplexing circuit to reduce the cabling problems is pursued for collider applications. Several systems have been developed during the last few years for low-noise data acquisition from microstrip detectors employing the strip-by-strip readout. In high-counting-rate applications, the solution based upon bipolar-transistor thick-film preamplifier of the transresistance type and described in subsect. **9**.3 has been extensively used at CERN [8].

Such a preamplifier is particularly suited for processing times shorter than 50 ns and input capacitances of the order of 10 pF, that is, for applications with fan-out printed-circuit boards not excessively large. Within these limitations, the preamplifier benefits from the good noise performances of the bipolar transistors at collector currents that are more than an order of magnitude lower than the usual drain currents in a field-effect transistor. This results in a small power dissipation, which is an advantage in such a large front-end system as microstrip detectors require. The preamplifier can be used in association with a fast amplifier and a threshold discriminator which senses the strip hit, in which case the shaping is of time-invariant nature, implemented by the natural band width limitations in the preamplifier and in the amplifier. Alternatively, if the pulse height analysis is advisable, as it happens when microstrip detectors are employed in tracking systems, the gated integrator at the ADC input performs in the already discussed fashion time-variant shaping. In microstrip applications, the use of a gated integrator rather than of a simple discriminator, even if the purpose is just that of sensing the hit on the strip, has the advantage of a much better rejection of spurious charge induction on the noncollecting strips as well as of cross-talk signals. Cross-talk is not a trivial problem in microstrip detectors of small-pitch readout with large fan-out printed-circuit boards featuring a high density of conductive paths. An alternative solution of microstrip readout is presently being employed in WA75 experiment at CERN [10]. The analog channels, intended for a strip-by-strip readout, consist of a charge-sensitive preamplifier with a JFET input stage, of an *RC* integration and of a track-and-hold amplifier. The outputs of the track-and-hold amplifier are digitized by analog-to-digital converters operating in a multiplexed way.

Every ADC serves 32 analog channels. The shaped analog signals are fed into the track-and-hold amplifiers, where their peak amplitude is stored upon receipt of a timing command. If the experiment trigger requirements are met, then the analog storage is confirmed to enable the multiplexed analog-to-digital conversion to be performed. Otherwise a fast clear is executed on the analog memories. The system is intended for application with a vertex detector consisting of 16 microstrip planes with 300 μm thickness and 50 μm pitch. The equivalent noise charge referred to the preamplifiers' input is about 1500 electrons r.m.s.

In order to meet the application requirements of microstrip detectors in collider experiments, research and development effort is presently being channelled into the monolithic solution of the front-end analog electronics. To be effective, such a solution must allocate on the same chip the preamplifier, the shaper and an analog multiplexer which has the purpose of reducing the number of cables leaving the front-end circuitry. The technological approach followed so far is based on VLSI MOS circuits [11, 12].

This solution, though suitable to implement a shaping employing the analog switching functions of fig. 10.7 and 10.9 as well as the analog multiplexing operations, leads to rather poor noise performances in the preamplifiers. A JFET-MOSFET compatible process, with the JFET as low-noise input stage and the MOS transistors implementing the other functions, would be certainly more suitable. Its feasibility is still to be investigated.

Analog front-end electronics employing MOS transistors only is presently undergoing the laboratory tests. The basic circuit diagram is very similar to the one shown in fig. 10.7. The outputs from several channels are multiplexed on a single analog line by a system of analog switches. This process of information serializing is controlled by a clock generated on the chip and takes place during the period between two consecutive bunch crossings.

The use of a monolithic technology does not allow the realization of resistors of large value. Therefore, an alternative solution must be found to the problem of the charge reset on the preamplifier feedback capacitance C_f, reset which in discrete or hybrid circuits is implemented by a resistor in parallel to C_f. The alternative solution adopted employs a switch in parallel to C_f, as shown in fig. 11.4. The switch S is closed during most of the time between bunch crossing. A few hundreds of nanoseconds before a bunch crossing S is opened. Once the baseline at the preamplifier output has settled, the sample at $t = t_0$ is taken (fig. 10.7). Passed the bunch crossing and after the second sampling instant, $t = t_1$, S is closed again. The described solution is feasible, of course, because of the predictable time of occurrence of the events which is a characteristic of collider experiments.

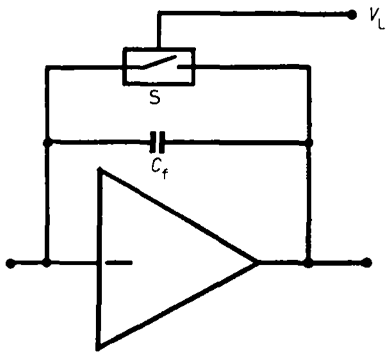

Fig. 11.4. – Switch-actuated charge reset.

Irrespectively of the type of solution adopted for the preamplifiers, in a detector in which every strip is read out, the output noise of each preamplifier is increased by the presence of the adjacent circuits. This statement is explained in fig. 11.5, where the three preamplifiers considered are supposed to have infinite gain-bandwidth product. The r.m.s. output noise for the K-th preamplifier can be expressed as

$$\overline{v_0^2} = \frac{\overline{e_N^2}}{C_f^2}\left[(2C_{is}+C_s+C_f)^2+2C_{i,s}^2\right],$$

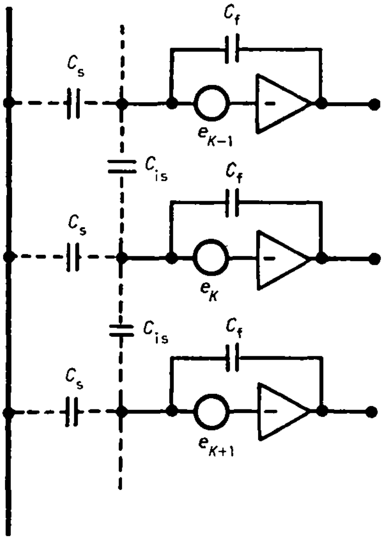

Fig. 11.5. – Effect of the adjacent preamplifiers on output noise of the K-th one.

where $\overline{e_N^2}$ is the input root-mean-square noise assumed equal for the three preamplifiers. As usually the values of C_{is} capacitances are larger than C_f and C_s, the presence of the adjacent preamplifiers increases the output noise of the K-th one of about 25%.

Microstrips' readout of the type analysed so far requires a large number of channels. The effect of noise increase due to the two adjacent preamplifiers must not be overlooked. As an advantage, the strip-by-strip readout has a double-track resolution which is close in value to the employed pitch.

A method which allows a reduction in the number of readout channels, more accuracy in the evaluation of the single-track position by virtue of its interpolating nature, but a lower double-track resolution, is based upon charge division and is shown in fig. 11.6 [13, 14]. As shown in fig. 11.6, there is one strip readout every N.

The hypothesis of ideal charge division between the two readout preamplifiers will be assumed at first; the parallel capacitances will be accordingly neglected for the strips that are not read out. For the strips 0 and N, to which

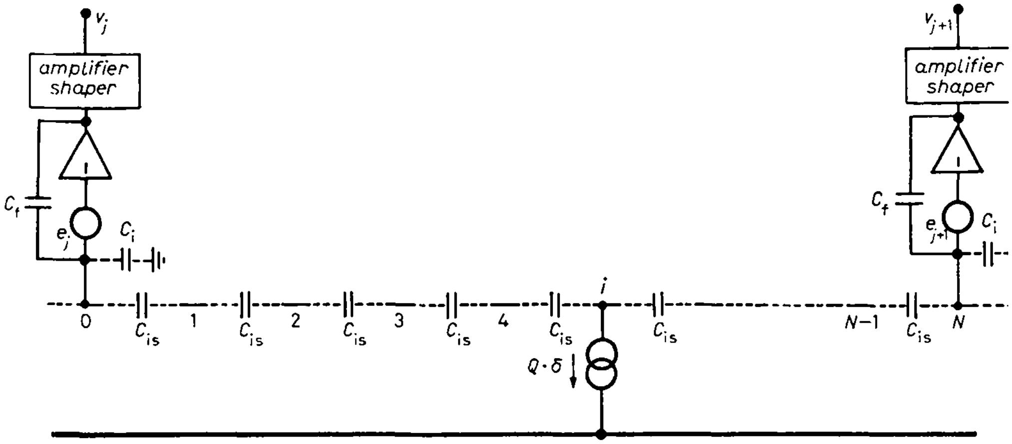

Fig. 11.6. – Position interpolation by charge division.

the preamplifiers are connected, the two capacitances C_i account for the sum of the preamplifier input capacitances and for the strays. Let e_j, e_{j+1} be the root-mean-square noise integrated on the band-pass of the shapers and referred to the input of the preamplifiers. The gain of the two analog channels will be assumed to be normalized in such a way that the peak amplitudes of the signals v_j, v_{j+1} are

$$v_{j,s} = \frac{Q}{C_f}\,\frac{N-i}{N}\,, \qquad v_{j+1,s} = \frac{Q}{C}\,\frac{i}{N}\,.$$

The noise at the v_j, v_{j+1} outputs is given by

$$(11.1)\qquad \left\{\begin{aligned} v_{j,N} &= e_j\left[\frac{C_i}{C_f} + \frac{C_{is}}{NC_f} + 1\right] + e_{j-1}\frac{C_{is}}{NC_f} + e_{j+1}\frac{C_{is}}{NC_f}\,,\\ v_{j+1,N} &= e_{j+1}\left[\frac{C_i}{C_f} + \frac{C_{is}}{NC_f} + 1\right] + e_j\frac{C_{is}}{NC_f} + e_{j+2}\frac{C_{is}}{NC_f}\,. \end{aligned}\right.$$

To explain the basic methods that can be employed to deduce the position information, the presence of the noise will be at first disregarded.

Under this hypothesis, the sum $v_{j,s} + v_{j+1,s} = Q/C_f$ is position independent and can be considered as a normalizing factor to obtain a position information without any dependence on the charge Q, that is, on the energy released in the detector. In the ideal case of noiseless readout amplifiers, the position is reconstructed by taking either quotient

$$(11.2)\qquad \frac{v_{j+1,s}}{v_{j,s} + v_{j+1,s}} = \frac{i}{N}\,,$$

or

$$(11.3)\qquad \frac{v_{j+1,s}-v_{j,s}}{v_{j+1,s}+v_{j,s}}=2\left(\frac{i}{N}-\frac{1}{2}\right),\qquad N \text{ even}.$$

In the former case the result is a linear function of the co-ordinate i measured from the readout preamplifier v_j; in the latter the position is evaluated with positive and negative signals and the zero is coincident with the central strip between the two preamplifiers.

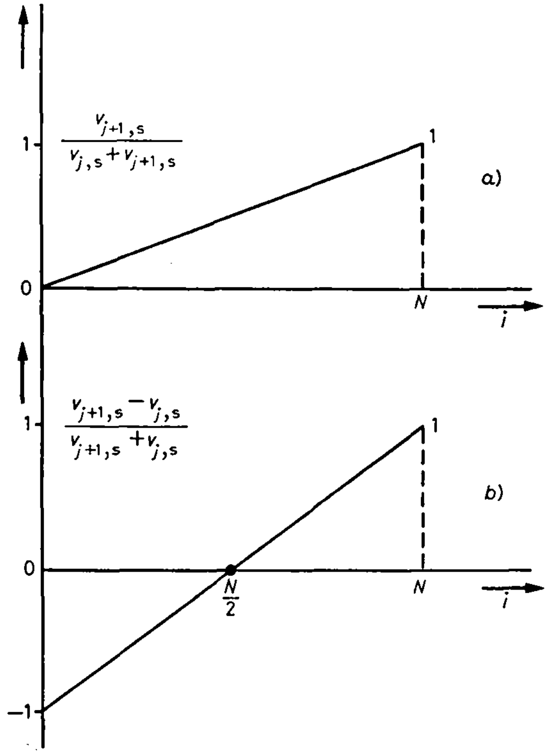

Fig. 11.7. – Signal as a function of the co-ordinate i with the two interpolation methods.

The dependence of the signal amplitude on i is shown in fig. 11.7 for the two cases.

The effect of noise in the two cases can be analysed by writing, in place of (11.2), (11.3), the actual quotients

$$(11.2')\qquad \frac{v_{j+1,s}+v_{j+1,N}}{v_{j+1,s}+v_{j+1,N}+v_{j,s}+v_{j,N}}$$

and

$$v_{j+1,s} - v_{j,s} + v_{j+1,N} - v_{j,N} \over v_{j+1,s} + v_{j+1,N} + v_{j,s} + v_{j,N} \tag{11.3'}$$

where the suffix s stands for signal and the suffix N stands for noise.

For $v_{j+1,N}$ and $v_{j,N}$ expressions (11.1) have to be introduced. In the actual situation, when discrete or hybrid preamplifiers are employed, the term C_i/C_t largely dominates and $v_{j,N}$, $v_{j+1,N}$ can be accordingly written simply as

$$v_{j,N} \simeq e_j \frac{C_i}{C_t}, \qquad v_{j+1,N} \simeq e_{j+1} \frac{C_i}{C_t}.$$

The variance of i/N is given in both cases, (11.2') and (11.3'), by

$$\frac{C_i^2}{Q^2}\left[\frac{(N-i)^2}{N^2} + \frac{i^2}{N^2}\right]\overline{e_N^2}, \tag{11.4}$$

where $\overline{e_N^2}$ is the square of the r.m.s. noise referred to the input and assumed to be the same for all the channels.

The function in brackets is plotted in fig. 11.8.

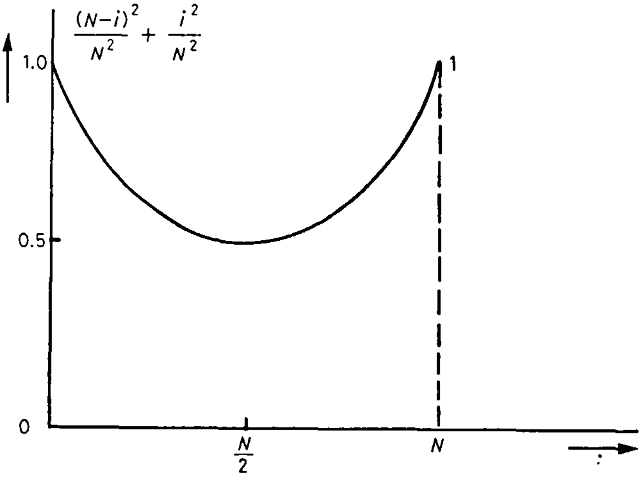

Fig. 11.8. – Dependence of the i/N variance on the i co-ordinate.

All the analysis developed so far disregards the effects of the parallel capacitances in the detector and applies, therefore, to the case in which $C_{is} \gg C_D$, where C_D is the capacitance of the diodes determined by the strips that are not read out and the depleted N region beneath them.

If the condition $C_{is} \gg C_D$ is not met, the ladder-type capacitive network resulting from the C_{is}, C_D cells in series introduces an attenuation in the charge appearing at the preamplifiers' input and would affect the position measurement with a nonlinearity even in the ideal hypothesis of absence of noise.

To satisfy the condition $C_{is} \gg C_{p}$, the detector should be manufactured by making, for a given pitch, the strips as wide as possible and the gap between strips as narrow as possible. Additional interstrip capacitance might be required if the previous method does not give a suitably high C_{is}/C_{p} ratio.

REFERENCES

[1] G. Bellini, P. D'Angelo, P. F. Manfredi, E. Meroni, L. Moroni, C. Palazzi-Cerrina, F. Ragusa and S. Sala: *Nucl. Instrum. Methods,* **196**, 351 (1982).

[2] G. Bellini, M. Conte, P. D'Angelo, P. F. Manfredi, D. Menasce, E. Meroni, L. Moroni, S. Sala and M. Szawlowski: *IEEE Trans. Nucl. Sci.*, NS-**30**, 415 (1983).

[3] S. R. Amendolia, G. Batignani, F. Bedeschi, G. Bellini, E. Bertolucci, D. Bettoni, G. Bologna, L. Bosisio, C. Bradaschia, M. Budinich, P. D'Angelo, M. Dell'Orso, B. D'Ettorre Piazzoli, F. L. Fabbri, F. Fidecaro, L. Foà, E. Focardi, P. Giannetti, M. Enorini, M. A. Giorgi, P. Laurelli, F. Liello, P. F. Manfredi, G. Mannocchi, P. S. Marrocchesi, D. Menasce, A. Menzione, E. Meroni, E. Millotti, L. Moroni, D. Pedrini, L. Perasso, P. Picchi, F. Ragusa, L. Ristori, L. Rolandi, S. Sala, A. Scribano, P. Spillantini, A. Stefanini, R. Tenchini, G. Triggiani, G. Tonelli and A. Zallo: *Nucl. Instrum. Methods Phys. Res.*, **226**, 78 (1984).

[4] R. Barate, P. Bonamy, P. Borgeaud, M. Burchell, M. David, Y. Lemoigne, C. Magneville, J. Movchet, P. Noon, J. Poinsignon, N. Primont, P. G. Rancoita and G. Villet: *Nucl. Instrum. Methods Phys. Res. A*, **235**, 235 (1985).

[5] A. Igiuni, P. Inzani, P. F. Manfredi, D. Marioli, C. Meroni, N. Radaelli, D. Torretta and G. Vegni: *Nucl. Instrum. Methods Phys. Res.*, **226**, 85 (1984).

[6] P. F. Manfredi and F. Ragusa: *Nucl. Instrum. Methods Phys. Res. A*, **235**, 345 (1985).

[7] V. Radeka: *Nucl. Instrum. Methods Phys. Res.*, **226**, 209 (1984).

[8] P. Jarron and M. Goyot: *Nucl. Instrum. Methods Phys. Res.*, **226**, 156 (1984).

[9] E. H. M. Heijne, E. Higon, P. Jarron, L. Rossi, P. Burger, W. Geerlings and M. Rynsent: *Nucl. Instrum. Methods Phys. Res.*, **226**, 63 (1984).

[10] R. Alberganti, E. Chesi, Ch. Gerke, F. Piuz, L. Ramello, T. D. Williams and R. Roosen: *A system of* 4400 *silicon microstrips readout with analog multiplexed electronics*, CERN-Rep EF/0089 P (3 Novembre 1983).

[11] R. Hofmann, G. Lutz, B. J. Bosticka, M. Wrede, G. Zimmer and J. Kemmer: *Nucl. Instrum. Methods Phys. Res.*, **226**, 196 (1984).

[12] J. T. Walker, S. Parker, B. Hyams and S. L. Shapiro: *Nucl. Instrum. Methods Phys. Res.*, **226**, 200 (1984).

[13] V. Radeka: *Position sensitive semiconductor detectors signal formation, noise and position readout*, in *Proceedings of the Workshop on Silicon Detectors for High Energy Physics, Fermilab, 15-16 October 1981,* edited by T. Ferbel (1981), p. 21.

[14] J. Kemmer, E. Belau, R. Klanner, G. Lutz and B. Hyams: *Development of* 10 μm *resolution silicon counters for charm signature observation with the* ACCMOR *spectrometer*, in *Proceedings of the Workshop on Silicon Detectors for High Energy Physics, Fermilab, 15-16 October 1981,* edited by T. Ferbel (1981), p. 195.

12. – Conclusions.

During the past few years, several semiconductor detecting devices have been introduced in elementary-particle experiments performed around the large accelerators.

Examples of these devices, according to their historical order of appearance, are the arrays of silicon detectors employed as active targets or as charged-multiplicity recognizers, the germanium active targets, the silicon microstrip detectors and the CCDs used for position-sensing and for vertex reconstruction purposes. More recently, large silicon detectors have been successfully tested as sampling elements in calorimetry, while new devices, like the silicon drift chamber, are progressing along their way to the experimental set-up.

When one of these devices is introduced into a complex experimental configuration, like the one that most of the experiments require, and is exposed to a high-intensity beam, several peculiar constraints affect the strategies adopted to process the signal delivered by the detectors. These strategies are entirely different according to whether solid-state detectors are employed in a fixed-target or in a colliding-beam experiment. Besides, they depend on several other parameters of the experiment and must be versatile enough to enable the experimenters to change some of these parameters.

A review of the criteria governing the detector signal processing under the particular constraints arising in experiments around large accelerators was one of the purposes of this paper.

Its second purpose is that of disseminating among the community of high-energy physicists a number of instrumentation solutions that have been developed with the aim of making the high-energy applications of solid-state detectors as effective as possible.

APPENDIX

The values of the integrals that more frequently appear in the frequency domain noise evaluations are given in this appendix for the readers' usefulness. A very good sourcebook of integrals is *Table of Integrals, Series and Products* by I. S. GRADSTEYN and I. M. RYZIK (Academic Press, New York, N. Y., 1965), whence some of the results quoted in this appendix were taken.

$$1)\ \int_0^\infty \frac{dx}{(1+x^2)^2} = \pi/4\,,$$

$$2)\quad \int\limits_0^\infty \frac{x^2\,\mathrm{d}x}{(1+x^2)^2} = \pi/4\,,$$

$$3)\quad \int\limits_0^\infty \frac{\sin^2 ax}{x^2}\,\mathrm{d}x = a\pi/2 \qquad (a>0)\,,$$

$$4)\quad \int\limits_0^\infty \frac{\sin^3 ax}{x^2}\,\mathrm{d}x = \frac{3}{4}\,a\ln 3\,,$$

$$5)\quad \int\limits_0^\infty \frac{\sin^4 ax}{x^2}\,\mathrm{d}x = \frac{a\pi}{4} \qquad (a>0)\,,$$

$$6)\quad \int\limits_0^\infty \frac{\sin^4 ax}{x^3}\,\mathrm{d}x = a^2\ln 2\,,$$

$$7)\quad \int\limits_0^\infty \frac{\sin^4 ax}{x^4}\,\mathrm{d}x = \frac{a^3\pi}{3} \qquad (a>0)\,,$$

$$8)\quad \int\limits_0^\infty \frac{\sin x}{x}\,\mathrm{d}x = \pi/2\,.$$

Direttore responsabile: RENATO ANGELO RICCI

Stampato in Bologna dalla Tipografia Compositori
coi tipi della Tipografia Monograf

Questo fascicolo è stato licenziato dai torchi il 26-III-1986

Questo periodico
è iscritto
all'Unione Stampa
Periodica Italiana